SCANNING TUNNELING MICROSCOPY AND SPECTROSCOPY MEASUREMENTS OF SUPERCONDUCTOR/FERROMAGNET HYBRIDS

A Dissertation
in Partial Fulfillment
of the Requirements for the Degree
DOCTOR OF PHILOSOPHY

by

Steven A. Moore

Department of Physics
Temple University

December 2015

Thesis Examination Committee:
Dr. Maria Iavarone, Temple University Physics Department, Chair
Dr. Alex Gray, Temple University Physics Department
Dr. Dieter Forster, Temple University Physics Department
Dr. Valentine Novosad, Argonne National Laboratory, External Examiner

ABSTRACT

The focus of this thesis work is the study of the nanoscale electronic properties of magnetically coupled superconductor/ferromagnet hybrid structures using low-temperature scanning tunneling microscopy and strectroscopy (LT-STM/STS) under ultra-high vacuum conditions. There are a number of novel effects that can occur due to the non-homogenous magnetic field from the ferromagnet, which directly influence the global and local superconducting properties. These effects include the generation of vortices/anti-vortices by the non-uniform magnetic stray field, local modulations in the critical temperature, filamentary superconductivity close to the transition temperature, and superconducting channels that can be controlled by external magnetic fields.

Prior to this dissertation the subject of superconductor/ferromagnet hybrid structures has been mainly studied using global measurements (such as transport and magnetization) or scanning probe techniques that are sensitive to the magnetic field. Scanning tunneling microscopy probes the local electronic density of states with atomic resolution, and therefore is the only technique that can study the emergence of superconductivity on the length scale of the coherence length. The novel results presented in this dissertation show that magnetically coupled superconductor/ferromagnet heterostructures offer the possibility to control and tune the strength and location of superconductivity and superconducting vortices, which has potential for promising technological breakthroughs in computing and power applications.

This thesis was supported by the U.S. Department of Energy, Office of Basic Energy Sciences, Division of Materials Sciences and Engineering under Award DE-SC0004556.

ACKNOWLEDGEMENTS

It goes without saying that the work done during this dissertation would not have been possible if it were not for the help and support of the people around me. As her first student, I would like to thank my advisor, Prof. Maria Iavarone, for her knowledge and patience in taking on the challenge to teach me such an extremely complicated technique starting from the ground up. I know it has been, and continues to be a seemingly impossible task, but her continued persistence and guidance cannot be underrated. Though not technically my co-advisor, I would like to thank Dr. Jan Fedor as such, and for visiting so many times over the years to work in the lab. Whether it be rebuilding the floor of the shielding room or developing a new sample holder, his knowledge and attention to detail played a huge role in making my research successful. I would also like to thank our collaborators, Prof. Goran Karapetrov and Dr. Valentine Novosad, for their continued advice during my dissertation. I could always count on them for a candid and honest evaluation of the results.

Probably they don't expect it, but I would like to thank the other members in the research group: Eric Lechner, James Curtis, Cinzia Di Giorgio, Daniel Trainer, Aleksei Putilov, Gabriel Plummer, and Jeffrey Timlin. Although they all joined the group much later than me, it has been helpful to have other students around. Although none of us will admit it openly, I think we would agree that it has been nice to make so many friendships along the way.

There have also been a number of other professors and staff in the department

who, at some time or another, have provided practical advice either about physics or life. I would like to thank Prof. Theodore Burkhardt, Prof. Dieter Forster, Prof. Tan Yuen, Prof. Peter Riseborough, Andrew Cuthbert, Karen E. Woods-Wilson, Jacqueline Farley, and Constance O'Donnell. I would also like to thank the members of my dissertation committee Prof. Maria Iavarone, Prof. Dieter Forster, Prof. Alex Gray, and Dr. Valentine Novosad for taking time out of their busy schedules to give advice during the final stages of my dissertation.

I also cannot thank enough the unsung heros of the basement machine shop, Edward Kaczanowicz and Matthew McCormick. Ed's experimental expertise in materials properties, low-temperature apparatus, and vacuum systems saved me a lot of time over the years, and for that I am eternally indebted. I also cannot count the number of times while making new designs that I went to ask Matt for advice on machinability, but what I do know is that it is almost as many times that he saved me from designing *scrap*. I would also like to thank Mr. Richard Harris in the electronics shop, who was always there with the components (and quarky stories) I needed in a pinch.

Undoubtedly, it is my family has made me who I am today, and without them I am not sure which path in life I would have taken. My sisters, Rachel McGhee, Sara Moore, and Michelle DePriest, who taught me how to stand up to any kind of beratement and criticism that could be thrown at me. My grandmother, Hideko Moore, who pushed me from a young age to finish everything I started and to do it well. My father, Dr. Steven R. Moore, who taught me by example that hard work does eventually pay off. Finally, my mother, Alice Moore, who has unconditionally had faith in me and supported me my entire life. I love you guys.

Finally, I never would have made it through this process without the love and support of Cassandra Sims. We started our life together at the same time that I started my research, and this dissertation is the culmination of a lot of work and

patience on both our parts. I cannot promise never to bring work home, but I can promise to not make you listen to any more presentations about vortices or domain walls.

CONTENTS

LIST OF FIGURES

CHAPTER 1

INTRODUCTION

For more than fifty years the coexistence of superconductivity and magnetism has been a widely studied topic within the condensed matter community. At first glance, the antagonistic nature of these materials makes superconductor/ferromagnet (S/F) hybrid structures unlikely candidates for useful technological breakthroughs. In particular, the effects of the electromagnetic and exchange interactions from the ferromagnet tend to suppress and modulate the superconducting order parameter. As will be described later, in conventional superconducting systems electrons having opposite spin and momentum are paired up into Cooper pairs via phonon interactions. Interactions with electromagnetic fields can modify the electronic orbital motion, and for large enough fields this can cause the Cooper pairs to break apart. On the other hand, for strong enough exchange interaction the spin of one of the paired electrons can be flipped, which also results in the break up of the Cooper pair. Investigations into the coupling of these two competing ground states first evolved from the study of ferromagnetic superconductors [1, 2]. Usually, in the case of ferromagnetic metals, the exchange field will dominate the system properties because it is much larger than the internal magnetic field. However, it was shown early on that in special circumstances superconductivity can be recovered by the application

of sufficiently high magnetic fields [3]. A thorough review of the early theoretical and experimental work involving both the orbital and exchange interactions in ferromagnetic superconductors has been provided by Bulaevskii *et al.* [4]. Although focused primarily on ferromagnetic superconductors, these early considerations opened the door towards the controllable manipulation of superconducting properties in systems involving both superconductivity and ferromagnetism, such as artificial structures.

Recent advancements in materials fabrication techniques have allowed investigations into the interplay between superconductivity and ferromagnetism in artificially constructed hybrid structures with unprecedented control. Differently from ferromagnetic superconductors, in superconductor/ferromagnet (S/F) hybrids the constituent materials can be physically separated. This separation, realized via a thin insulating layer, prohibits effects due to the short range exchange interactions while still allowing effects driven by the long range orbital interaction. By creating a purely magnetically coupled S/F system fundamental properties such as the nucleation length scales for superconductivity, the nucealtion conditions for vortices, the dynamics of vortices, and the H-T phase diagram can all be altered depending sensitively on the materials and geometries chosen for the system. The focus of this dissertation is concerned with measurements of the nanoscale electronic properties of these magnetically coupled superconductor/ferromagnet hybrid structures using low-temperature scanning tunneling microscopy and spectroscopy (STM/STS) under ultra-high vacuum conditions in order to unravel the underlying physical principles emerging on these mesoscopic length scales.

In this dissertation, the first three chapters provide a brief overview of the theoretical basis and experimental techniques underlying the results. The concept of superconductivity is introduced, followed by an explanation of the novel physical phenomena that emerge in magnetically coupled superconductor/ferromagnet hybrid structures. Finally, an understanding of the experimental techniques and equip-

ment necessary for scanning tunneling microscopy (STM) and spectroscopy (STS) is provided. The remaining chapters are comprised of a collection of published and unpublished work performed during this thesis, in the field of superconducting films and superconductor/ferromagnet hybrids, which for convenience and clarity are summarized below.

- Chapter 4: Ultrathin Pb films

  Ultrathin films of Pb have been used extensively during this dissertation as the superconducting material in the investigated S/F hybrid structures. Before investigating the resulting properties in the S/F hybrid, we have studied the superconducting properties of the Pb films in absence of the ferromagnet layer. When the size of the metal is reduced to the size comparable to the Fermi wavelength of the electrons, the physics of the system is dominated by quantum mechanics instead of classical physics. Indeed, electrons confined in a thin metal film on a surface form standing-wave eigenstates in the direction perpendicular to the surface. These discrete electronic eigenstates are known as quantum well states (QWS) [5]. Their eigenenergies crucially depend on the film thickness, because the Fermi wavelength is typically ∼1nm. Consequently, as a function of film thickness, the electronic density of states (DOS) is modulated in an oscillatory manner when a QWS passes through the Fermi level. The oscillatory behavior of the electronic properties at E_F affects many of the physical and chemical properties of a thin film, e.g., the local work function, the chemical reactivity, the thin film thickness [6], or even the superconducting properties a tlow temperature [7]. Characterizations performed on continuous ultrathin Pb films in various stages of growth have resulted in one published paper [8].

- Chapter 5: Threshold of vortex nucleation

The presence of the underlying magnetic template in S/F hyrbrids can cause superconducting vortices to be generated spontaneously in the absence of externally applied magnetic fields. Theoretically defined nucleation thresholds for the generation of these vortices depend strongly on specific material and geometry dependent properties, and spontaneously generated vortices are not guaranteed [9]. STM and STS are the ideal tools for the visualization of these effects on the atomic scale. Measurements were carried out on an S/F hybrid with a ferromagnet film having asymmetric magnetic domain widths, thereby teetering on both sides of the nucleation threshold and allowing for the direct experimental assessment of these theoretically defined conditions. This work shows that it is possible to control the formation of spontaneous vortices/antivortices, that are detrimental for some applications. Moreover, it also constitutes a proof of principle that vortex imaging can be used to identify the structure of the underlying magnetic template with a measurement technique that is not inherently sensitive to magnetic features. The results discussed in this chapter are a restatement of another work published during this dissertation [10].

- Chapter 6: Domain wall and reverse domain superconductivity

  One of the most fundamental phenomena predicted in magnetically coupled superconductor/ferromagnet hybrid structures is the emergence of the superconducting condensate into thin filamentary regions that are localized at regions above the domain walls on a lengthscale of roughly twice the superconducting coherence length. Predicted theoretically [11], and previously inferred by macroscopic techniques [12, 13], measurements made during this dissertation have provided the first nanoscale visualization of the so-called domain wall superconductivity state. Furthermore, these measurements show the controllable

switching of the localized nucleus of superconductivity with application of external magnetic fields, which has a high potential for use in applications. This chapter is an overview of these results, which have also been published [14].

- Chapter 7: S/F hybrids with off-axis superconducting films

  Low-temperature scanning tunneling microscopy and spectroscopy measurements on magnetically coupled superconductor/ferromagnet hybrid structures are presented, where the c-axis of the superconducting film is tilted with respect to the surface of the ferromagnet. Temperature and spatially dependent spectroscopy measurements and conductance maps in applied magnetic field reveal superconducting properties that vary locally at the nanoscale. These results indicate that in a system where the superconducting film is oriented off-axis the parallel component of the magnetic stray field plays a substatial role in determining the superconducting properties over a large portion of the phase diagram. Moreover, it is suggested that the visualization of these effects is due to the ability to measure energy shifts in the quasiparticle excitation spectrum due to the doppler effect of the supercurrents.

CHAPTER 2

SUPERCONDUCTOR/FERROMAGNET HETEROSTRUCTURES

2.1 Brief overview of superconductivity

After being the first to successfully liquify helium in 1911, and consequently revolutionize the field of low temperature physics, Kamerlingh Onnes discovered superconductivity in elemental mercury [15]. This discovery came in the form of a precipitous drop in the resistivity at single digit Kelvin temperatures, which for historical reasons is shown in figure 2.1. Soon after, this behavior was confirmed in a number of other elements, although the temperature at which the resistivity drop occured (T_c) differed with material. While this kind of behavior can be characteristic of a perfect conductor, the discovery in 1933 that magnetic fields are also expelled below T_c unambiguously put superconductors into a class on their own [16]. A perfect conductor cooled down in the presence of a magnetic field cannot expel that field, and instead when the field is turned off it will remain trapped in the interior [17]. What was instead shown by the Meissner effect, as it came to be known, is that a superconductor cooled down in the presence of a magnetic field will actually expel

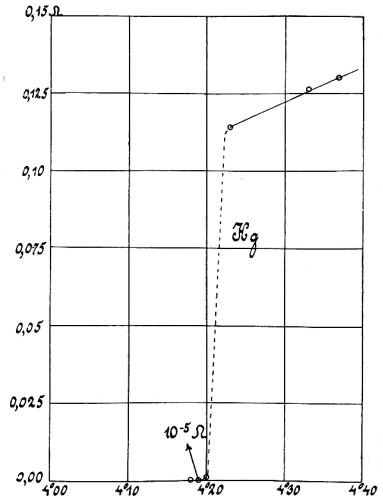

FIGURE 2.1: First measurement of superconductivity made by Kamerlingh Onnes on elemental Mercury which shows the drop in resistivity at the transition temperature (T_c) of 4.2K that is characterisitic of superconductivity.

the field from its interior. Figure 2.2 shows how the magnetic field lines behave for a superconductor above and below T_c.

A number of brilliant theories were later put forward to explain these two basic properties of superconductors (zero resistivity and the Meissner effect). The two London equations, introduced in 1935, explained quite well the Meissner effect from simple electrodynamic principles by introducing the idea of a current flowing around the perimeter of the superconductor which expelled the magnetic field. In this way, the magnetic field penetrated the superconductor on a length scale λ_0, which is the first appearance of the superconducting penetration depth. Over the next few decades the theoretical nuiances of superconductivity were ironed out amongst a rapidly growing body of experimental data. Following Landau's theory of second-order phase transitions [18], Ginzburg and Landau developed a phenomenological theory to describe superconductivity without knowing the underlying microscopic

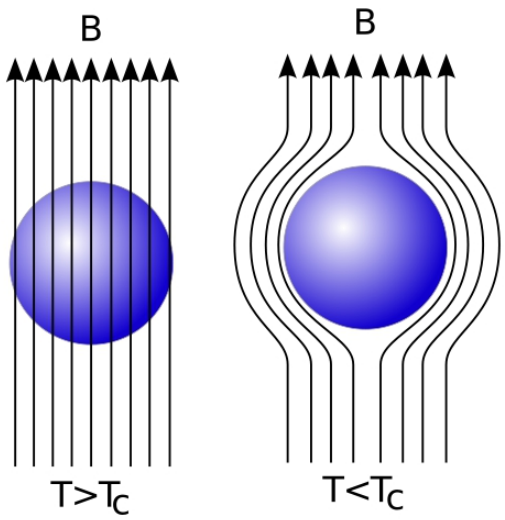

FIGURE 2.2: Magnetic field lines of a superconducting sphere above (left) and below (right) the transition temperature (T_c) showing the expulsion of the magnetic field from the interior of the superconductor (*i.e.* Meissner effect).

mechanism [19]. Gizburg-Landau (GL) theory assumes that near the superconducting transition the free energy of the system can be expressed using an order parameter ψ, which is small just below and zero just above the T_c. One of the main features to come out of this theory is that superconductors can be characterized by two distinct length scales, the first of which is the temperature dependent coherence length $\xi(T)$, that describes the spatial variation over which perturbed superconducting electrons return to their equilibrium value ψ. The other characteristic value to emerge naturally from GL theory is the penetration depth λ, which is one in the same as that found in the London formalism.

Overall the scientific community was fairly satisfied with the progress towards the understanding of superconductivity, but there still remained the mystery regarding the microscopic origins of this intriguing phenomenon. Finally, in 1957,

Bardeen, Cooper, and Schrieffer reinvigorated the field by introducing the first microscopic model of superconductivity. According to the Bardeen-Cooper-Schrieffer (BCS) model electrons near the Fermi energy pair up into Cooper pairs due to a weak attractive electron-phonon mediated interaction [20, 21]. The result of this pairing is an energy gap in the density of states $\Delta \approx 2\hbar\omega_d e^{-1/N(0)V}$ around the Fermi energy, where ω_d is the Debye cutoff energy and $N(0)$ is the density of states at the Fermi energy [17]. With respect to the BCS superconducting density of states

$$N_s(E) = \frac{|E|}{\sqrt{E^2 - \Delta^2}} \tag{2.1}$$

the energy gap that opens up around Δ creates a divergent pile up of quasiparticles in the DOS, as shown in figure 2.3. In tunneling experiements the DOS is probed directly, making tunneling the ideal tool to investigate superconductivity. As a consequence, because of the atomic scale resolution of the scanning tunneling microscope, it is the only choice for direct measurements of superconducting properties on the local scale. The topic of tunneling, and more specifically scanning tunneling microscopy, will be covered in more detail in chapter 3.

While the GL theory was originally phenomenological and based on the theory of phase transitions, a later derivation by Gor'kov [22] showed that it was completely reconcilable within BCS theory as a limiting case, thereby giving a microscopic meaning to the ideas of the coherence length and penetration depth. Moreover, as a result of this work, it was shown that the order parameter from GL theory ψ is proportional to the gap parameter Δ. This was lucky with respect to the interpretation of data because unlike in BCS theory where the energy gap Δ is considered to be constant in space, the complex order parameter from GL theory naturally accomodates gradual spatial inhomogeneities.

In the presence of the boundary conditions imposed by fields, currents, or gradients ψ should be considered in terms of its amplitude and phase, $\psi(\mathbf{r}) = |\psi(\mathbf{r})| e^{-i\psi(\mathbf{r})}$,

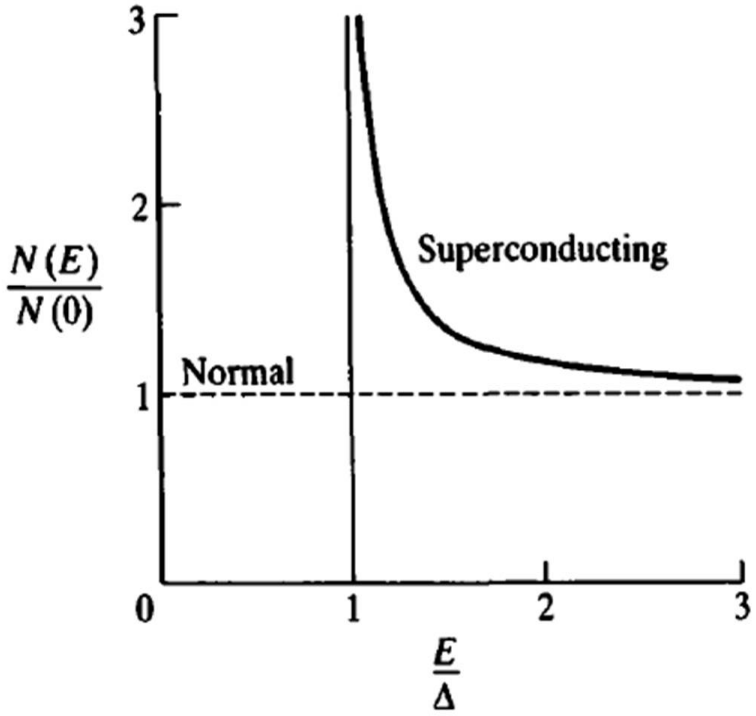

FIGURE 2.3: Taken from reference [17] the dotted line shows the density of states of a normal metal ($T > T_c$) and the solid line shows the density of states of the quasiparticles in a superconductor ($T < T_c$) in the limit of $T \rightarrow 0$.

which will which will adjust itself to minimize the total free energy given by the volume integral of

$$f = f_{n0} + \alpha |\psi|^2 + \frac{\beta}{2} |\psi|^4 + \frac{1}{2m^*} \left| \left(\frac{\hbar}{i} \nabla - \frac{e^*}{c} \mathbf{A} \right) \psi \right|^2 + \frac{h^2}{8\pi} \tag{2.2}$$

where f_{n0} is the free energy of the normal state, α and β are coefficients of expansion, m^* is twice the electron mass, e^* is twice the electron charge, $\mathbf{A}$ is the magnetic vector potential, and h is the magnetic field. This integral leads to the GL differential equations

$$\alpha\psi + \beta |\psi|^2 \psi + \frac{1}{2m^*} \left(\frac{\hbar}{i} \nabla - \frac{e^*}{c} \mathbf{A} \right)^2 \psi = 0 \tag{2.3}$$

and

$$\mathbf{J} = \frac{e^*}{m^*} |\psi| \left(\hbar \nabla \psi - \frac{e^*}{c} \mathbf{A} \right) \tag{2.4}$$

where here it has been assumed that no current passes through the surface of the superconductor. By taking the kinetic energy term of the supercurrents from equation 2.2 together with the kinetic energy density in the London model ($A^2/8\pi\lambda^2$) the penetration depth λ can be derived. Similarly, the solution to equations 2.3 and 2.3 when $\mathbf{A}$=0 gives the coherence length ξ. One of the fundamental conclusions that falls out of the GL equations is that superconductors can be separated into two classifications (type-I or type-II) depending on the surface energy between the normal and superconducting regions in applied magnetic fields, which as it turns out can be expressed in terms of the ratio of λ to ξ. Unfortunately, due mainly to low transition temperatures and low thermodynamic critical magnetic fields (H_c), there is limited potential for applications using type-I superconductors for which $\lambda/\xi < 1/\sqrt{2}$. As a result, further discussions will be constrained to the properties of type-II superconductors having $\lambda/\xi > 1/\sqrt{2}$, which hold a high potential for applications.

As was mentioned earlier in this section, superconductors subjected to external magnetic fields can display peculiar behaviors, the most notable being the flux expulsion due to the Meissner effect. Early research placed a huge emphasis towards understanding these phenomena, and as a result it was understood early on that it is possible for the superconductor exposed to magnetic fields to break up into normal and superconducting regions below H_c. From GL theory it can be calculated that in type-II superconductors there will be a negative energy contribution at the interface between these normal and superconducting states, making the superconductor unstable against the formation of such interfaces. The first implications of this were not experimentally observed until the measurements of Shubnikov showing two critical magnetic fields [23], which would later be explained in the groundbreaking work by

Abrikosov [24].

In that work, Abrikosov showed that below some lower critical field (H_{c1}) the type-II superconductor indeed acts as a perfect diamagnet through the Meissner effect. However, in the *mixed state*, for applied fields above H_{c1} a small tube of quantized magnetic flux ϕ_0=$hc/2e$ penetrates the superconductor turning the region inside the tube normal (*not* superconducting), and thereby creating the more energetically favorable interface. Figure 2.4 depicts schematically this normal tube, where the interior of the surrounding superconductor is isolated from this normal region by circulating supercurrents (j_s). Drawing from similarities in the field of fluid dynamics, the tube became known as an Abrikosov *vortex* because of the rotational supercurrents. As the cartoon shows, from the center of the vortex the magnetic field (H) penetrates the superconductor on a lengthscale of of λ, while the Cooper pair density (n_s) drops exponentially within the *normal* vortex core on a lengthscale of ξ. As the magnetic field is increased further an increasing number of vortices will penetrate the sample, and because of intervortex interaction from the circulating supercurrents these vortices will form an ordered lattice [25]. The first experimental visualization of this flux line lattice shown in figure 2.5 was provided by Essmann and Träuble using the bitter decoration technique [26]. At some value of magnetic field (H_{c2}) the vortex density will become too high and the superconductor will become completely normal.

It should be noted that the spatially dependent magnetic behavior of the vortex core is exploited by a number of low-temperature measurement techniques such as magnetic force microscopy, scanning squid microscopy, and scanning hall probe. These measurements, which will not be discussed in detail here, are directly sensitive to λ, making the resolution at large vortex densities limited due to a substantial overlap of the circulating supercurrents. Instead, for reasons to be discussed in detail in the following chapter, the scanning tunneling microscope (STM) is inherently

sensitive to the electronic properties of the vortex allowing for investigations much farther into the mixed state. This is possible because the electronic properties inside the normal vortex core are very different from the surrounding superconductor, which can best be understood by referring to the density of states shown in figure 2.3. Inside the superconductor there is a depletion of states in some range around the Fermi energy due to the presence of the energy gap (Δ), and for conservation these states pile up at the quasiparticle coherence peaks ($\pm\Delta$). Instead, within the normal vortex core the density of states (dashed line) is, in the simplest case, that of a normal metal (i.e. flat around the Fermi energy). By measuring spatially the local density of states at energies less than the superconducitng gap or at the coherence peak energies, STM resolution is due to the difference inside (normal) and outside (superconducting) the vortex core. The change in the local density of states seen by STM occurs over lengthscales of ξ. Imaging of the variations in the density of states has been heavily used during this dissertation work to visualize vortices and other mesoscopic superconducting phenomena, and will be described in more detail in later chapters.

With these concepts of superconductivity (GL and BCS) firmly in hand the community set out to increase the potential applicability of these materials by optimizing the superconducting properties. Until the discovery of the high-T_c materials this search lead to the development of many superconducting alloys and the A15 materials, which had a maximum T_c of around $\sim$23 K [27] and all followed the behavior expected from BCS theory. However, a dramatic breakthrough in the field of superconductivity came in 1986 with the discovery of the doped ceramic high-T_c material Ba-La-Cu-O having a T_c of around $\sim$35 K [28]. This discovery again reinvigorated research in superconductivity, which quickly led to the discovery of many more of the cuprates with T_c up to 133K [29, 30]. However, many questions started to emerge with respect to this new class of superconductors that didn't really follow

the behavior expected from the available theories. The BCS theory describes the pairing of electrons through some weak attractive potential due to electron-phonon interaction. However, an attraction between electron can also be mediated by other bosonic modes. One thing that remains true is that BCS theory assumes a non-zero density of states at the Fermi energy in the normal state just above T_c, but in this new class of materials there exists a "pseudogap" phase just above T_c which depletes the states around the Fermi energy. Thus, superconductivity in the cuprates emerges from a phase that is not the metallic state needed for the BCS mechanism of superconductivity. This, and other oddities in the behavior of the cuprates, created a race in the condensed matter community to identify the pairing mechanism in the high-T_c materials, and while the details are now better understood, this search is still going on. The ultimate goal is that the understanding of the mechanism of superconductivity in these classes of materials can pave the way to the discovery of materials with higher critical temperature and eventually room temperature superconductivity. Along the way it was also discovered that superconductivity can exists in a number of other materials including the organic compounds, borocarbides, pnictides, MgB_2, and most recently the iron-based materials such as iron selenides and pnictides. Some of these materials such as MgB_2 and the organic compounds can be well described by BCS theory using the idea of electron-phonon coupling, but in the case of the pnictides and iron-based materials there is still a debate going on in the community about how superconductivity emerges in these systems.

Due to the number of open questions regarding the superconducting properties in many of these *unconventional* materials, and to simplify the interpretation of the effects of a non-uniform magnetic field distribution on the superconducting properties, the work done in this dissertation on superconductor/hybrid structures uses the *conventional* superconductors which are well described by BCS theory and its extensions. In the following sections two of the primary mesoscopic phenomena, namely

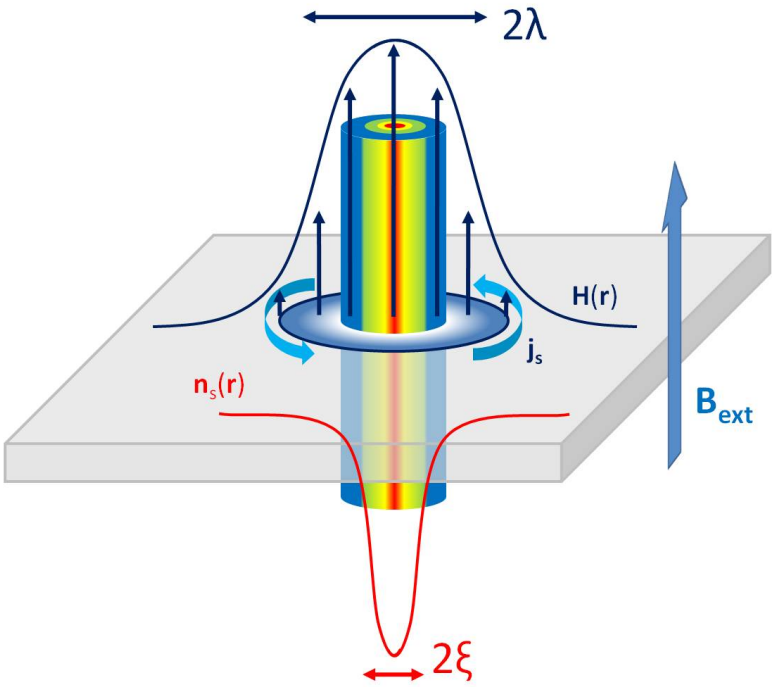

FIGURE 2.4: Abrikosov superconducting vortex that is formed when a type-II superconductor is subjected to fields larger than its lower critical field (H_{c1}). To remain superconducting above H_{c1} the superconductor will set-up circulating supercurrents (j_s) that generate exactly one quantum of flux (ϕ_0=$hc/2e$=2.07×10^{-7}G·cm^2). This fluxoid exists within a small region of the sample and its magnetic field decays on a length scale of the penetration depth λ into the superconductor. Instead, the Cooper pair density (n_s) evolves on a lengthscale of ξ with respect to the vortex core. Being that n_s is proportional to Δ, the measurement of the local density of states using the scanning tunneling microscope probes ξ of the vortex core.

spontaneous vortices and domain wall superconductivity, that can be observed in *magnetically* coupled superconductor/ferromagnet structures will be introduced.

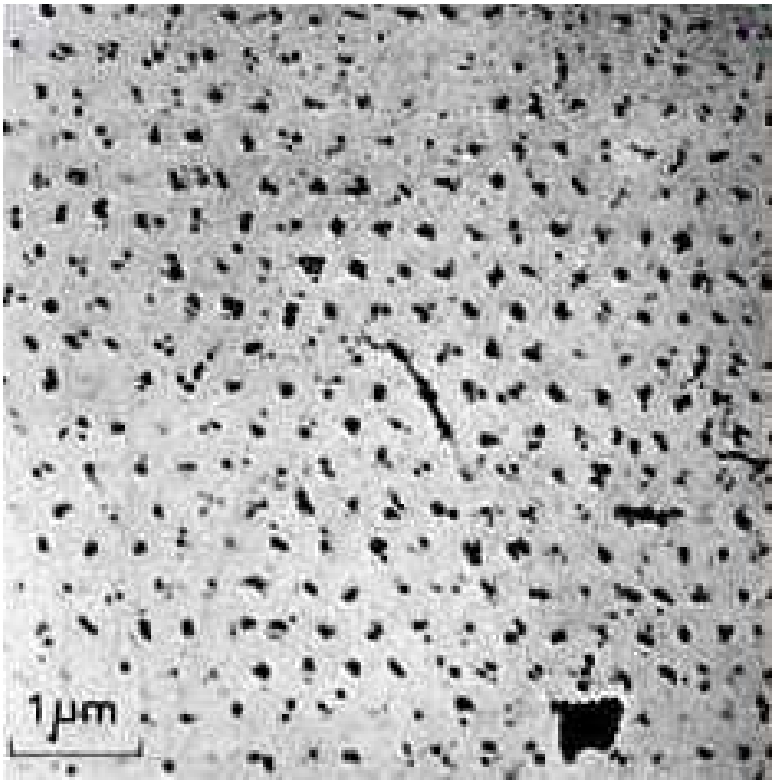

FIGURE 2.5: "Perfect" triangular lattice of flux lines on the surface of a lead-4at%indium rod at 1.1K. The black dots consist of small cobalt particles which have been stripped from the surface with a carbon replica [26].

2.2 Magnetically coupled systems

Historically , by their very nature, superconductors and ferromagnets don't play well together. In the case of ferromagnetism the ordered state is brought about by the alignment of the electron spins, whereas the Cooper pairs in singlet state superconductors should have opposite spin ($\uparrow\downarrow - \downarrow\uparrow$) in accordance with BCS theory. Simple considerations, and early experimental and theoretical works, indeed show that ferromagnetism can be very detrimental to the superconducting state. Nevertheless, it turns out systems comprised of ferromagnets and superconductors exhibit very interesting physical phenomena. Through the interaction between the ferromagnet

and superconductor the Cooper pairs can be broken up either by the strong effect of the exchange field acting on the electron spin (exchange interaction) or by the effect on the orbital motion of the electrons in a magnetic field due to the Lorentz force (orbital interaction). In the former case, same spin triplet ($\uparrow\uparrow$ and $\downarrow\downarrow$) Cooper pairs can also be formed under certain circustances, giving rise to a great potential use for applications involving superconductor/ferromagnet spin sensitive interfaces. A couple of excellent overviews on the subject have recently been compiled by Eschrig [31, 32].

All of the measurements on superconductor/ferromagnet hybrid structures presented in this dissertation have been performed in the magnetic coupling regime where only the orbital interaction plays a role in the system properties. These structures were fabricated having a thin insulating layer to separate the superconductor and ferromagnet. In this way, the non-uniform stray field of the ferromagnetic modulates the superconducting properties in a controlled manner. However, because this dissertation successfully addressed many of the phenomena expected to emerge in the magnetically coupled system, work is already well underway to investigate the new behavior that emerges in the proximity coupled regime. In the following sections, the novel behaviors expected to emerge in magnetically coupled S/F systems is discussed.

2.2.1 Nucleation thresholds for superconducting vortices

The treatment of vortex nucleation in superconductor/ferromagnet (S/F) hybrids revolves around the minimization of the total system energy. For planar S/F systems, shown schematically in figure 2.6, the total energy can be conveniently separated into individual energy contributions

$$E_{total} = E_{sv} + E_{vv} + E_{vm} + E_{mm} + E_{dw}, \tag{2.5}$$

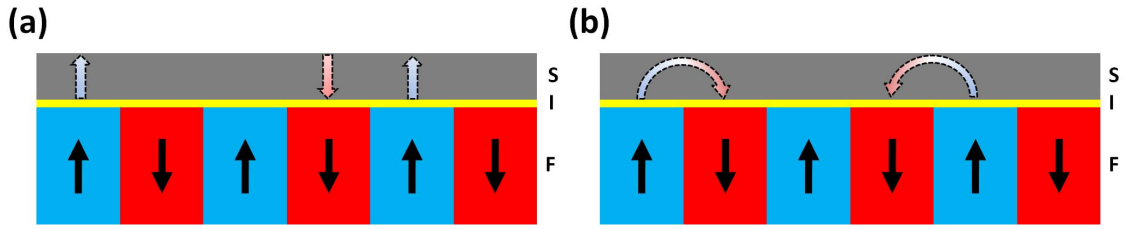

FIGURE 2.6: Illustrative cartoon of the nucleation of spontaneous vortices in an S/F bilayer in the case of (a) straight vortices and (b) vortex semi-loops, which are generated by the magnetic stray field of the underlying ferromagnet under the conditions outlined in the text.

where E_{sv} is the self-energy of a single vortex, E_{vv} is the energy due to vortex-vortex interactions, E_{vm} is related to the interaction of the vortex with the Meissner currents induced by the magnetic field of the ferromagnet, E_{mm} is the self-energy of the ferromagnet, and E_{dm} is the surface energy of domain walls [33, 34, 9]. As shown in figure 2.6, in planar S/F systems close to T_c, two unique vortex states emerge from the solution of the energy minimization, straight vortices and vortex semi-loops [9].

Straight vortices enter and exit at the two different superconductor interfaces, whereas vortex semi-loops turn inside the superconductor to enter and exit through the same interface. Due to different energy contributions and barriers, at decreased temperatures semi-loops tend to escape the system while straight vortices remain trapped [35]. Moreover, any signatures due to the sub-surface semi-loops are not accessible to scanning probe measurements [35] and as a result, further considerations will focus only on straight vortices. What is most fascinating is that, under the appropriate conditions, these vortices can be generated spontaneously in the superconductor by the underlying ferromagnet in the absence of applied field. It is not surprising that vortices are nucleated in the presence of the underlying magnetic field, but both theoretical [9] and experimental works [36, 35, 10] have conclusively

shown that this nucleation is extremely sensitive to the unique system properties, and spontaneous vortices are not a guaranteed consequence of the S/F composite geometry. In calculating the conditions for the appearance of spontaneous vortices, with respect to the total energy defined previously, many of the individual energy terms can be neglected in the majority of cases. Typically the contributions from E_{dm} and E_{mm}, which determine the equilibrium domain structure of the ferromagnet, can be disregarded on the assumption that the superconductor does not influence too much the domain structure of the ferromagnetic film [33]. Strictly speaking, as shown in magneto-optical measurements of Nb on iron-garnet films [37, 38], this assumption is not always valid and care must be taken to ensure that the chosen ferromagnetic film is not substantially modified by magnetic interactions with the superconducting film. In general, selecting a hard ferromagnet with a Curie temperature much higher than the superconducting transition temperature ($T_c > T_s$) can help to isolate the dynamics of the domain development in the ferromagnet from the superconductor. At low vortex densities, the vortex-vortex interactions will also be small, and the E_{vv} term can also easily be neglected in the total energy. The remaining terms are at least one order of magnitude larger than the neglected terms and give for the conditions for the nucleation of spontaneous vortices, and similarly anti-vortices, as $E_{total} \approx E_{sv} + E_{vm} < 0$. The limiting cases of thick and thin superconducting films (with respect to the penetration depth, λ) have been considered analytically [33, 9], where the self-energy of the single vortex is

$$E_{sv} = \frac{\Phi_0^2 d_s}{16\pi^2\lambda^2} ln\left(\frac{\lambda}{\xi}\right) \tag{2.6}$$

and the interaction of the vortex with the Meissner currents is

$$E_{vm}(x_0) = \int_{\infty}^{x_0} f_{mv}(x_0')dx_0' \tag{2.7}$$

where $f_{mv}(x_0)$ is the force acting on the vortex due to the Meissner currents [33]. As a result, in the case of a thin superconductor ($d_s < \lambda$), vortices will only be energetically favorable if

$$M_0 > \left(\frac{\Phi_0}{4\pi^2\lambda_{eff}}\right)\left(\frac{1}{w}\right)\ln\left(\frac{\lambda_{eff}}{\xi}\right) \quad ; \quad \lambda_{eff} << w \tag{2.8}$$

where M_0 is the magnetization in the magnetic domain, $\lambda_{eff}=\lambda^2/d_s$ is the effective penetration, Φ_0 is the quantum of flux, ξ is the coherence length, d_s is the superconductor thickness, and w is the magnetic domain width. Considering the complicated dependence of the critcal magnetization on the S/F system properties, it is not surprising that the nucleation of vortices is actually a non-trivial problem. It is important to note that the presence of an external magnetic field will introduce an additional energy contribution ($\pm H d_s \Phi_0/4$) with the sign depending on the relative orientation between the applied field and the polarity of the magnetic domain. Under these external magnetic fields vortices can be nucleated, and vortex densities increased/decreased, in systems otherwise not exhibiting spontaneous vortex characteristics due to effects of compensation of the applied field on the stray magnetic field of the ferromagnet.

2.2.2 Localized nucleation of filamentary superconductivity

Similarly to the case of vortices in superconductor/ferromagnet (S/F) hybrids discussed in the previous section, the filamentary nucleation of localized superconductivity in an ideal S/F system can best be understood by considering a ferromagnet with a uniform striped magnetic domain structure, as depicted schematically in figure 2.7. In this configuration the superconducting film experiences a non-uniform magnetic stray field, which alternates in polarity in-line with the magnetization of the underlying magnetic domains. Furthermore, for ferromagnetic films having a thickness much greater than the domain width ($D >> w$) this alternating magnetic

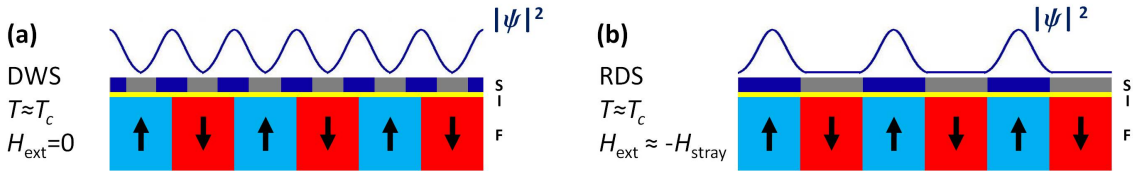

FIGURE 2.7: Illustrative schematic of filamentary superconductivity in the cases of (a) domain wall superconductivity (DWS) and (b) reverse domain superconductivity (RDS). In the absence of externally applied magnetic fields, the superconductor experiences a minimum in the perpendicular magnetic stray field from the ferromagnet in the regions localized between the domains (*e.g.* domain wall), and as a result when cooling below T_c localized filaments of superconductivity (dark blue) will first appear in these locations. However, when an perpendicular external field is applied the minimum of the magnetic stray field is shifted due to compensation effects, and the localized nucleation of superconductivity (dark blue) will instead be shifted above the magnetic domains with magnetizations anti-parallel to the applied field.

field as seen by the superconducting film is step-like and homogenous in the regions above the domains. As a result, in these regions the stray field is a maximum and the critical temperature for the nucleation of superconductivity is suppressed due to the orbital interactions. On the other hand, due to an energetically favorable rotation of the perpendicular magnetization towards the in-plane direction at the domain wall [39] the perpendicular stray field seen by the superconductor approaches zero locally. When the temperature of the S/F system is decreased through T_c, due to a partial decrease in the orbital effect above this in-plane region, the superconducting state will first emerge at the domain walls in a way that is reminiscent to surface superconductivity below H_{c3} [40, 41]. This localized superconductivity, so-called domain wall superconductivity (DWS), forms a very inhomogenous filamentary superconducting state which is only expected to occur close to the T_c where the orbital interactions above the domain centers still suppress development of a more global superconducting state.

While DWS in S/F bilayers occurs in the absence of externally applied magnetic fields, the situation changes drastically when an external field is instead turned on. Due to compensation effects, regions of the superconductor located above domains having the opposite polarity to the external field will see a decrease in the effective stray field, while regions having the same polarity will instead see an increase. Now when the temperature is decreased below T_c the localized superconducting state that develops will be shifted away from the domain wall region, and towards the space with the lowest compensated effective magnetic field. Increasing the applied field further will lead to continued shifting of the nucleation location until the value of the stray magnetic field is reached, at which point the localized superconducting state will be nucleated directly above the center of the magnetic domains with opposite polarity to the applied field. Because the external magnetic field partially alleviates the effects of the orbital interaction above domains with magnetization anti-parallel to the field, the system can actually exhibit an *increase* in T_c under applied fields. Collectively this shifting of the localized superconducting nucleus and increase in the transition temperature is called reverse domain superconductivity (RDS), and any further increase in magnetic field will lead to a global weakening in the superconducting strength and a lowering of T_c.

Formally, theoretical considerations of DWS begin with the linearized Ginzburg-Landau equation [42, 43, 17]:

$$-\left(\nabla + \frac{2\pi i}{\Phi_0}\right)\Psi = \frac{1}{\xi^2(T)}\Psi \tag{2.9}$$

where $\mathbf{A}(\mathbf{r})$ is the vector potential, Φ_0=2.07$\times 10^{-7}$ G$\cdot$cm^2 is the flux quantum, $\xi(T) = \xi_0/\sqrt{1-T/T_{c0}}$ is the coherence length, and T_{c0} is the critical temperature of the superconducting film in the absence of the ferromagnetic layer. By choosing the proper gauge and neglecting any dependence of the order parameter in the perpendicular

direction it is possible to calculate the critical temperature as a function of magnetic field thereby mapping out the H-T phase diagram for the S/F system [41]. An example H-T diagram exhibiting DWS and RDS, is shown in figure 2.8 where it is clear that the T_c of the system changes non-monotonously under applied fields.

Of course the actual behavior seen in real S/F bilayers depends intimately on the system properties, and especially important is the shift of critical temperature due to the orbital interaction $\Delta T_c^{orb} = T_{c0}\xi_0^2/L^2$ where T_{c0} is again the critical temperature of a reference superconducting film, ξ_0 is the coherence length, and L is related to the magnetic stray field through $L^2 = \Phi_0/(2\pi H_{stray})$. In the case that ΔT_c^{orb} is too small it will be impossible to detect DWS or any related effects because there is an inadequate variation of the order parameter ($|\psi|^2$ in figure 2.7) over the surface of the superconductor, and as a result there appears only a global reduction in T_c. On the other hand, also important theoretically is the relationship between the superconducting nucleation length (ξ) and the domain width (w). In the idealized case of an isolated domain wall, and sufficiently large ΔT_c^{orb}, DWS will always be favorable [41]. However, real S/F systems usually have a periodic magnetic structure, and this periodicity imposes the other, perhaps more stringent, constraint that the domain width be larger than roughly twice the nucleation length at T_c ($w >> \xi(T_c)$). It should emphasized that the coherence length at the transition temperature of the S/F hybrid $\xi(T_c)$ is not the same as the coherence length of an isolated superconducting film at the transition temperature $\xi(T_{c0})$, which in the latter case has a divergent behavior. Indeed, the behavior of the coherence length in the S/F hybrid is related to the coherence length of the isolated superconducting film through $\xi(T) = \xi_0/\sqrt{1 - T/T_{c0}}$, where ξ_0 is the zero temperature coherence length, T_{c0} is the critical temperature of the superconducting film without ferromagnet, and T is the temperature of the S/F bilayer.

If this condition is not met, the localized superconducting regions above the

domain walls overlap, again resulting in a global reduction in T_c and the absence of DWS. In S/F systems where both ΔT_c^{orb} and the domain widths are sufficiently large the nucleation of superconductivity will be located above the domain wall.

While the previously discussed field compensation effects leading to the emergence of superconductivity localized above domains will occur regardless of the realization of DWS, the same cannot be said of the re-entrant behavior shown in the H-T diagram of figure 2.8. If the conditions are not met for DWS there will be no increase in T_c with applied fields. Instead the H-T diagram will shown a flattening near low fields, which is still different than the linear behavior expected from BCS theory. Direct measurements on two similar S/F systems close to the critical threshold conditions for the nucleation of this localized superconducting state are discussed in Chapter 6. These results show with nanoscale resolution the evolution and severe dependence of this state on the microscopic system properties.

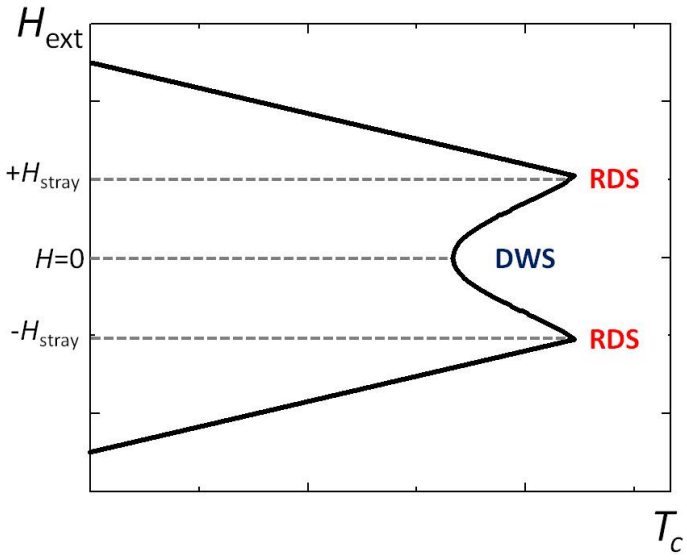

FIGURE 2.8: Example H-T phase diagram for and S/F bilayer exhibiting domain wall (DWS) and reverse domain superconductivity (RDS). In zero externally applied fields the superconductor will have a T_c that is reduced by the amount ΔT_c^{orb} with respect to a reference superconductor in the absence of the ferromagnetic film. Here, in the case DWS, the nucleation of superconductivity is localized in filamentary regions above the domain walls of the underlying ferromagnet. Application of an external magnetic field leads to an increase in T_c due to compensation effects. Locally the superconductivity is shifted away from the domain walls and towards the center of the domains with magnetization anti-parallel to the applied field. The maximum increase in T_c occurs when the applied field is equal to the stray magnetic field, and any further increase in applied field leads to a monotonic decrease in T_c.

CHAPTER 3

SCANNING TUNNELING MICROSCOPY AND SPECTROSCOPY

3.1 Basics of Scanning Tunneling Microscopy

The scanning tunneling microscope (STM) is one of the most powerful tools available in surface science for the study of electronic properties of materials with atomic resolution. The concept of STM was first developed by Gerd Binning and Heinrich Rohrer in 1982 while at IBM Zurich, and the importance of this discovery is reflected in the researchers very quickly being awarded the Nobel Prize in Physics in 1986. Scanning tunneling microscopy relies on the quantum mechanical tunneling effect whereby electrons can *tunnel* between a tip and sample through a barrier region resulting in an experimentally measurable current. The most important feature of STM lies in the fact that this tunneling current is exponentially dependent on the distance between the tip and sample which allows for sub-Å resolution in the z-direction. Although the underlying concepts were known for a long time, the ability to acquire the location dependent electronic properties with atomic resolution came only after the necessary experimental breakthroughs needed to scan at such close distances, and while the lateral resolution ultimately depends on the exact nature of

the tip, sub-Å resolution of is routinely acheived.

While measurements using STM always contain information of the local electronic properties of the sample, in discussion they are often separated into two classifications: scanning tunneling microcroscopy (STM) and scanning tunneling spectroscopy (STS). For the former, the focus is generally on acquiring the topographic information by scanning the tip over the surface of the sample, and in the latter case the measurement is more focused on spectroscopic electronic information of the sample.

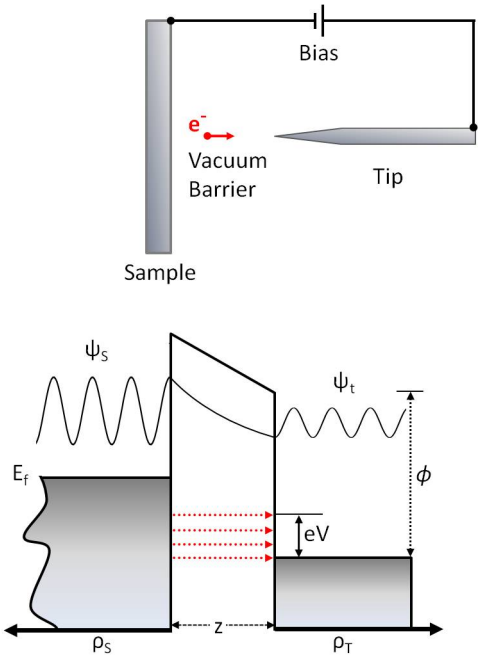

FIGURE 3.1: Schematic demonstrating the basic principle of STM. Electrons tunnel from the sample to the tip through the vacuum region with the help of a bias voltage. In this case, because the density of states of the tip (ρ_t) is flat the tunneling current reflects the density of states of the sample (ρ_s).

The arrangement between the tip and sample of an STM experiment in vacuum is shown schematically in figure 3.1, where a metallic tip is brought close to a conductive sample and according to quantum mechanics there is a non-zero probability

for electrons to traverse the vacuum barrier region in between. When a bias voltage is applied between the tip and the sample there will be a net flow of electrons in one direction, which results in a measurable tunneling current.

Inside the barrier region the electron wavefunction is expected to take the form of a decaying exponential

$$\Psi(z) = \Psi(0)e^{-\kappa z} \text{ and } \kappa = \frac{\sqrt{2m(\Phi - eV)}}{\hbar} \tag{3.1}$$

where z is the distance between the tip and the sample, Φ describes the height of the barrier and is related to the workfunctions of the sample and tip, and eV is the electron energy supplied by the bias. The probability of a single electron to tunnel across the barrier is

$$|\Psi(z)|^2 = |\Psi(0)|^2 e^{-2\kappa z} \tag{3.2}$$

and the resulting current is proportional to the probability of electrons making it through the barrier region

$$I(z) \propto \sum_{E_n = E_f - eV}^{E_f} |\Psi_n(0)|^2 e^{-2\kappa z} \propto I(0)e^{-2\kappa z}. \tag{3.3}$$

For a typical workfunction value of around 5eV, a 1Å change in tip-sample separation can result in almost an order of magnitude change in tunneling current.

In STM topographic mode, it is this exponential behavior of the tunneling current that allows for a measurement of the topography of the surface of a sample. Figure 3.2 shows the arrangement of a typical STM experiment, where a tip is *scanned* across the surface of a sample by applying high voltages to a piezoelectric material. There are different designs and geometries for the piezos used to scan, but in this case a "tube" scanner is used, which is depicted in figure 3.2. Here four electrodes are placed on the outside of a hollow cylinder made of a piezoelectric material such

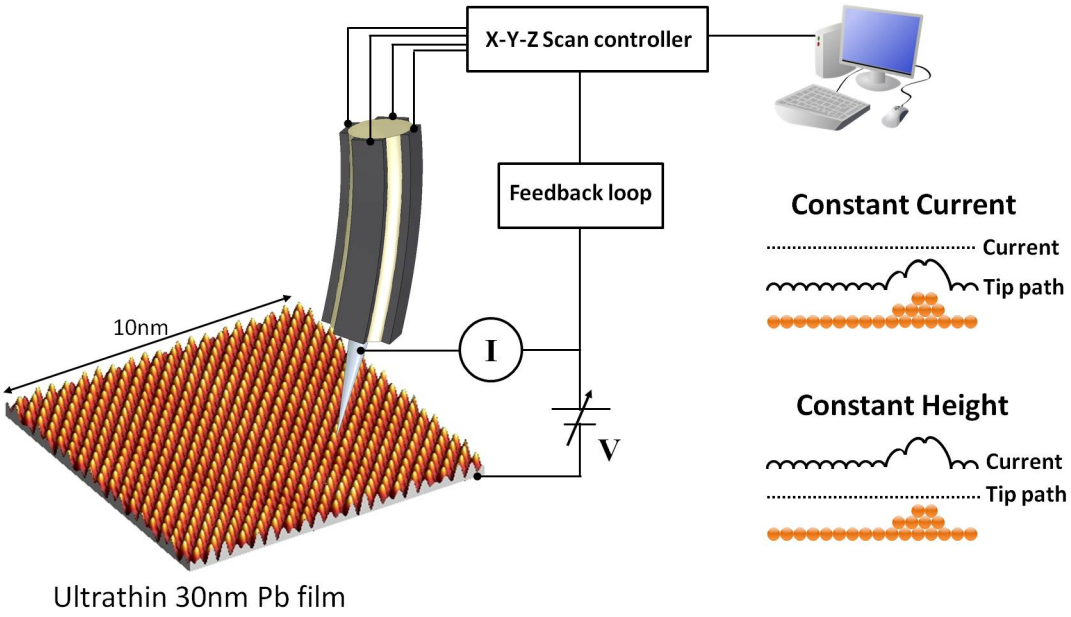

FIGURE 3.2: Typical STM arrangement where a metallic tip is scanned over the surface of a conductive sample and application of a bias voltage (V) results in a measurable current (I). Topographic scanning can be acheived using two different modes: constant current and constant height. In constant current the value of the current is kept constant by varying the voltage on the z-piezo during scanning. The voltage applied to the z-piezo is mapped, which can be processed into a topographic image of height. Instead, in constant height mode, the feedback loop is disabled and the tunneling current is mapped during scanning resulting in a topographic image of current. The topographic image in the schematic is a real 10 nm $\times$ 10 nm atomic resolution image of an ultrathin 30nm Pb film acquired in constant current mode.

as lead-zirconate-titanate (PZT) for x-y motion, as well as an electrode inside the hollow tube surface for z motion. The voltages applied to the piezo, as well as the resulting tunneling currents, are monitored and controlled using dedicated low-noise electronics and computers. In "constant current" mode a desired value of the tunneling current is defined to be the setpoint of a feedback loop. During scanning the feedback is used to adjust the voltage on the scanning piezo in the z-direction to keep this current, where the distance versus voltage response of the piezo material

has been pre-calibrated. In this way, by monitoring the voltage applied to the z-piezo by the feedback loop, a precise topographic map of the height can be created.

There is another useful mode of scanning that exploits the exponential dependence of the tunneling current, which is commonly referred to as "constant height" mode. Unlike "constant current" mode, in "constant height" mode the feedback is inactive during scanning. The tip is stabilized above the surface using a given bias voltage and current value. The feedback is then removed and scanning performed while acquiring directly the resulting tunneling current. A schematic visually showing the difference between these modes is shown in figure 3.2. It should be noted that if κ, which reflects Φ, is known the information from these two scan modes can be directly compared through equation 3.3 relating current to distance.

In STM topographic mode the goal is to acquire some kind knowledge regarding the morphology of the sample surface by exploiting the exponential dependence of the current on the tip-sample separation. Instead, in STS spectroscopic mode the goal is to directly acquire information about the local density of states of the sample surface. To understand STS and how the output of the experimental tunneling current corresponds to the actual density of states requires a more careful treatment, which will be covered in the following section.

3.2 Theory of tunneling and spectroscopy

In the previous section an overview of scanning tunneling microscopy and spectroscopy was provided in a way that makes this technique seem deceptively simple. On the contrary, it took many great scientists a number of years to develop the theory and experimental knowledge to make these measurements a reality. In fact, well before the scanning tunneling microscope was invented tunneling phenomenon in planar metal-insulator-metal junctions was being adressed both theoretically and experimentally [44, 45]. Because the tunneling effect is quantum in nature, the tun-

neling rate of electrons between the tip and sample is governed by Fermi's Golden Rule

$$w = \frac{2\pi}{\hbar} |M|^2 \delta(E_\psi - E_\chi) \tag{3.4}$$

where ψ and χ describe the individual electronic wavefunctions respectively inside the tip and sample and $\delta(E_\psi - E_\chi)$ ensures only electron states of the same energy contribute to the tunneling rate. To describe the recent tunneling results of Giaever [44], and following Oppenheimer's treatment of transition rates in atomic hydroden subjected to a strong electric field [46], Bardeen developed an approach to tunneling theory in junctions using time-dependent perturbation theory.

Treating the wavefunctions of the tip and sample separately, and assuming that they are roughly orthogonal, the tunneling matrix is given by

$$M = -\frac{\hbar^2}{2m} \int_{z=z_0} \left(\chi^* \frac{\partial \psi}{\partial z} - \psi \frac{\partial \chi^*}{\partial z} \right) dS \tag{3.5}$$

which describes the overlap of the tip and sample wavefunctions in the barrier region. Following the treatment of Bardeen, the net tunneling current that results from an arrangement as shown in figure 3.1 is the sum of the current flowing from the tip to the sample and vice versa

$$I = I_{tip \rightarrow sample} - I_{sample \rightarrow tip} \tag{3.6}$$

$$I = \frac{4\pi e}{\hbar} \int_{-\infty}^{\infty} |M|^2 \rho_t(E_t) \rho_s(E_s) \left\{ f(E_t)[1 - f(E_s)] - f(E_s)[1 - f(E_t)] \right\} dE \tag{3.7}$$

where e is the electron charge, $\hbar$ is the reduced Planck's constant, M is the tunneling matrix element, $\rho_{s,t}$ are respectively the density of states of the sample and tip, and $f(E) = \left[1 + e^{-(E - E_f)/k_B T}\right]^{-1}$ is the Fermi distribution function with k_B the Boltzmann constant and T the temperature. Here the relationship is exploited that the local

density of states near the Fermi energy is $\rho_s(z,E) = \frac{1}{\epsilon}\sum_{E}^{E-\epsilon}|\Psi_n(z)|^2$, which gives that $I \propto V\rho_s(z,E_f)$. By writing the energies of the sample and tip with respect to their Fermi energies in the presence of an applied bias voltage equation 3.7 can be simplified to:

$$I(V) = \frac{4\pi e}{\hbar}\int_{-\infty}^{\infty}|M|^2\,\rho_t(E)\rho_s(E+eV)\,\{f(E)-f(E+eV)\}\,dE \tag{3.8}$$

after $E_t = E$ and $E_s = E + eV$ have been substituted. While taking a fairly simple form, in practice the tunneling current actually has complicated dependence on the exact nature of the tip and sample through the tunneling matrix element, as well as the local density of states of both the tip and sample. In practice, the tunneling matrix element is often taken out of the integral because it is considered to be constant at low voltages and for a constant tip-sample separation. Although this can often be a safe assumption, there has been a lot of work done to analyze the validity of this simplification [47, 48, 49, 50, 51]. Because $|M|$ describes the overlap of the wavefunctions from the tip and sample in the barrier region, it will change for different tip and sample combinations, different tip materials, and even for different tips of the same material. However, in addition to assuming a constant matrix element at low voltages and constant separation it is customary to assume a constant matrix element throughout an isolated experiment with the same tip. However, there are many things that can happen experimentally where this assumption fails, with the most catastrophic being a collision with the sample surface. The tip, and therefore also $|M|$, is one of the most difficult elements to control experimentally, so these are definitely things that should be kept in one's mind when performing STM and STS measurements.

3.3 Differential conductance spectroscopy

While the ability to measure topographic details on the sample surface with atomic resolution is a great acheivement, the real power of scanning tunneling microscopy is found in the ability to extract the local density of states from the material surface with that same resolution. From equation 3.8 it is understood that the tunneling current is strongly dependent on the local density of states of the sample and tip, where the assumption has already been made that the tunneling matrix element is constant. Moreover, if the energy range of interest is small around the Fermi energy, then for most metallic tip materials the density of states can be considered constant and also taken out of the integral. This further simplifies the current given in equation 3.8 to be

$$I(V) \propto \frac{4\pi e}{\hbar} |M|^2 \rho_t(0) \int_{-\infty}^{\infty} \rho_s(E+eV) \{f(E) - f(E+eV)\} dE \tag{3.9}$$

and, if the sample is superconducting, taking the derivative with respect to the voltage gives the differential tunneling conductance (dI/dV)

$$\frac{dI}{dV} \propto G_{nn} \int_{-\infty}^{\infty} \frac{\rho_s(E)}{\rho_t(0)} \left[-\frac{\partial f(E+eV)}{(eV)} \right] dE \tag{3.10}$$

with substituting $G_{nn}=\frac{4\pi e}{\hbar} |M|^2 \rho_t(0)\rho_s(0)$, which is the tunneling conductance when both the tip and sample are normal metals ($T > T_c$). At low temperatures ($T \to 0$) the function $\partial f(E+eV)/\partial(eV)$ behaves as a Gaussian weighting function centered at $E = -eV$ and having width $\sim 4k_BT$, and therefore in this limit

$$\left.\frac{dI}{dV}\right|_{T=0} \propto G_{nn} \frac{\rho_s(e|V|)}{\rho_t(0)} \tag{3.11}$$

showing that for small energies and at low temperatures the differential tunneling conductance is directly proportional to the local density of states of the sample.

3.4 Experimental measurement of the differential conductance

Measurements of the current-voltage (I-V) characterstics described by equation 3.8 are fairly straight forward. At a fixed tip to sample distance, just ramp the voltage and measure the resulting tunneling current. In figure 3.3 a typical I-V curve on an ultrathin 30nm Pb film is shown (red line), where the behavior is ohmic far from the Fermi energy. However, near the Fermi energy there is a large deviation from ohmic behavior due to the presence of the superconducting energy gap at this temperature. This I-V curve can be explained quite well by equation 3.8 together with the superconducting density of states given by Bardeen-Cooper-Schreiffer (BCS) theory, and in principle taking the numerical derivative can provide directly the differential tunneling conductance.

However, the most common method to measure the dI/dV versus V curves is to use the lock-in method. By modulating the bias voltage (V in equation 3.8) with a small AC voltage of known frequency ($V_m \sin\omega t$) and expanding in a power series

$$I(V + V_m sin\omega t) = I(V) + \left.\frac{dI}{dV}\right|_V V_m \sin\omega t + \frac{1}{4}\left.\frac{d^2I}{dV^2}\right|_V V_m^2(1 - \cos 2\omega t) + ... \qquad (3.12)$$

it is possible to measure directly the differential conductance by acquiring the DC signal of the first harmonic of the output, which is phase locked to the known frequency.

An example spectra acquired simultaneously to the I-V on the same ultrathin Pb film using the lock-in technique is shown by the black curve in figure 3.3. Here the noise level is very low, and the superconducting coherence peaks and phonon contributions to the density of states are easily distinguishable. It should be mentioned that among many things, special care still needs to be taken when choosing the magnitude of the AC voltage, as well as the sampling rate of the measurement with respect to the time constant (over which an averaging takes place) of the lock-in

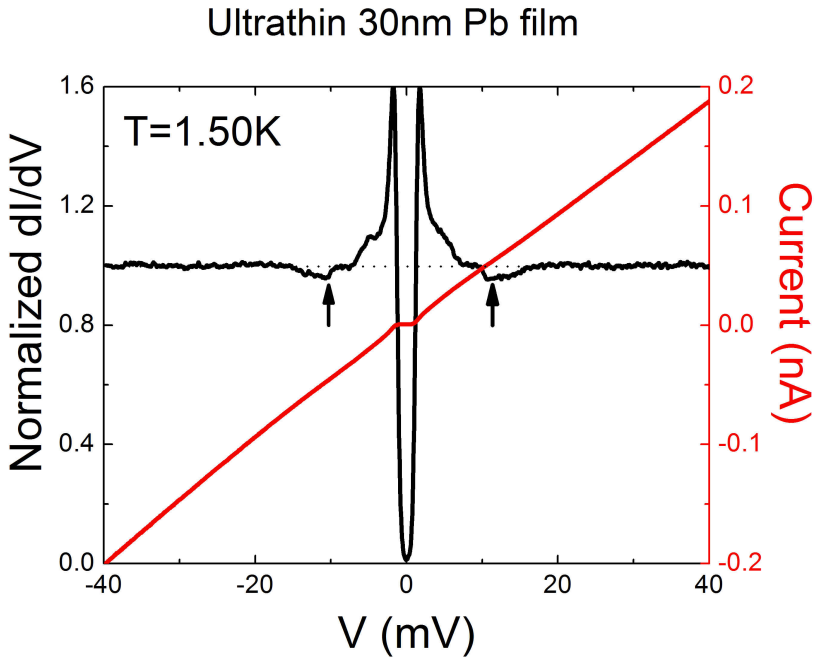

FIGURE 3.3: Experimental current-voltage (red) and differential conductance (black) simultaneously acquired on an ultrathin 30 nm Pb film both showing the presence of the superconducting gap. The differential conductance data has been acquired using the typical lock-in modulation technique for scanning tunneling spectroscopy measurements. Arrows have been added to indicate the symmetric contributions to the density of states due to the strong electron-phonon coupling at $\pm\Delta \pm \Omega$, where in the case of Pb there are two contributions due to the longitudinal and transverse phonons at $\approx$4.4 and 8.5meV [52].

amplifier. A general rule of thumb for selecting the magnitude of the modulation voltage to give the best signal to noise is to understand that the thermal broadening of the measurement will set a minimum of $\sim 3k_BT$, which gives for 400 mK that $V_m \geqslant 100$ μV. Additional noises on the signal (instrumental, electronic, ground loops, etc.) can cause this value to be higher, but this should be the lower limit. However, if the value of V_m is too high or the sampling rate too fast with respect to the lock-in time constant there can be an unintentional smoothing of the data. To avoid this

possibility, and as a continuous check of the quality of the data, all measurements in this dissertation were made by acquiring simultaneously the *I(V)* (without lock-in) and *dI/dV* (with lock-in) and optimizing the parameters. The conductance curve in figure 3.3 over a high energy range shows not only the superconducting coherence peaks at $\sim\Delta\approx\pm 1.40$ meV, but also the strong electron-phonon coupling induced dip. Here, the gap values have been extracted by fits of the experimental data to equation 3.10 using the Dynes modified DOS for the superconductor, which will be discussed in more detail in later chapters.

3.5 Ultra-high vacuum low-temperature scanning tunneling microscope

In the previous sections the exponential dependence of the tunneling current on distance between the tip and sample was stressed to be the principle behind scanning tunneling microscopy (STM), but as the adage goes you can't get something for nothing. This also means that one has to be able to control the tip-sample distance with a very strict tolerance. The first obstacle in designing a successful STM is to limit physical vibrations coming from the surrounding environment, which is actually a complicated and interesting problem in engineering design in its own right. In the following few sections these topics will be discussed briefly to give an idea of some of the challenges involved in low-temperature STM experiments.

3.5.1 Lab design and vibration isolation

In the summer of 2015 the STM used for this dissertation work was moved on the Temple University campus from the basement of Barton Hall (now destroyed) to the new Science Education and Research Center (SERC). Although similar in many respects to its predecessor, this new lab was specifically designed to attenuate vibrational noise to a level not possible in Barton Hall. A cross-sectional schematic of the new lab design is shown in figure 3.4, where the only real difference between the lab in Barton Hall and the lab in SERC is a 40 ton inertial mass and the corresponding large vibration isolation legs. This new lab space is an engineering feat on its own accord, and an extensive description of the design is outside of the scope of this dissertation. The main point here is to decouple the STM (indicated in figure 3.4) from the surrounding environment using as many vibration dampening stages as possible, where each stage has a different resonance frequency. However, the design of these stages is a very non-trivial matter. Detailed discussions of the mechanics of the design considerations needed to reduce vibrational noise, discussed in terms

of transfer functions and system response, have been the subject of a number of papers [53, 54, 55, 56] which can also be found summarized in the introductory text on STM by Chen [51]. To give an idea of the order of magnitude in noise reduction needed, some of the authors in these works suggest having vibrational levels less than a pico-meter to see the atomic corrugation of metal surfaces [53, 56]. In modern labs like the one in SERC noise levels lower than this are acheived regularly. Photographs of the shielding room design, including the inertial mass, raised floor, and isolators, are provided in figure 3.5 to give a feeling for what actually goes into making a well designed STM lab.

Assuming that the level of vibrational noise from the surrounding environment has been reduced to the necessary levels through proper design, the real challenge of STM is to limit the amount of electronic noise. With respect to the sheilding room depicted in figure 3.4 this is accomplished by creating a Faraday cage surrounding the entire space, which strongly attenuates (-100 dB) any RF noise up to 10 GHz. It is tricky to make a room like this that is completely sealed to RF leakage especially at the higher frequencies, but the real difficulty in the design of this room is actually how to pass the signals coming from the control electronics, through the RF shielded acousitc walls, and to the microscope without degrading the performace of the room. To that end, all electronic cables entering/exiting the room pass through specially designed low-pass filters. This is not an easy task since the electronics used such as temperature controllers and the scanning electronics all have different requirements for how the signals are passed. Additionally, any other feedthroughs such as pumping or gas lines, have been specifically designed not to act as waveguides over the specified range of frequencies. The previous lab in Barton Hall and the new lab in SERC both went through strenuous noise performance testing to ensure the optimum performance with respect to both acoustic and RF shielding, but the final and most sensitive test is always the STM measurement itself.

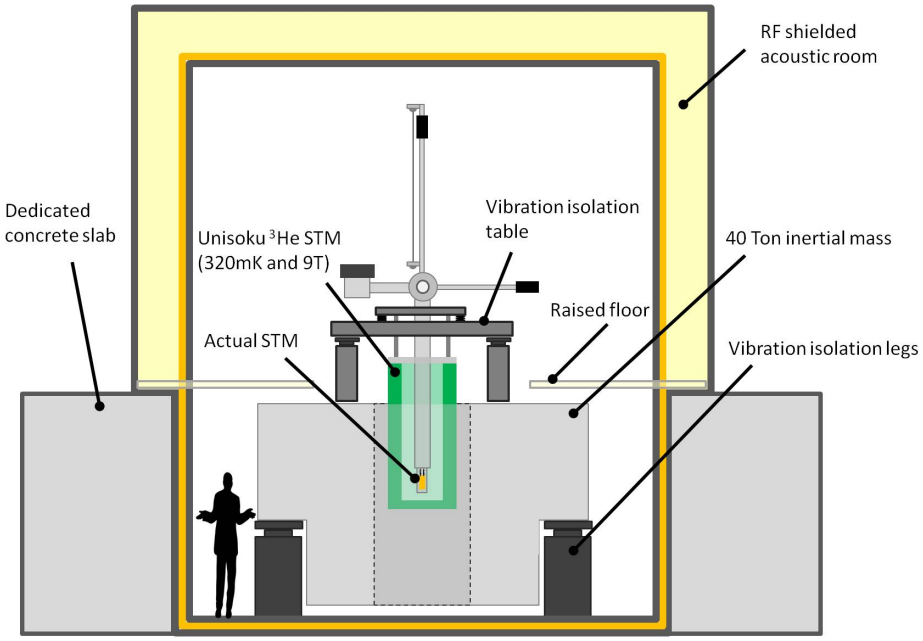

FIGURE 3.4: Layout of one of the new scanning tunneling microscopy labs in the Science Education and Research Center (SERC) at Temple University. This state of the art lab is located in the basement of the building and has been built on a section of concrete slab physically separated from the rest of the building. The slab features a large pit which houses the entire RF shielded acoustic room as shown in the illustration. Inside the shielded room the scanning tunneling microscope rests on a 40 ton inertial mass that is supported by six large vibration isolation legs. To avoid introducing vibrations during routine operations within the shielded room there is a raised floor that is completely decoupled from the inertial mass. All pumping lines and cables are mass damped before entering the shielding room. The previous arrangement of the lab in the basement of Barton Hall was similar, but without the inertial mass and large vibration isolation legs.

3.5.2 Ultra-high vacuum low-temperature scanning tunneling microscope and in situ fabrication capabilities

The STM used during this dissertation is a commercially available USM1300 ^{3}He system capable of reaching temperatures as low as 350 mK and axial magnetic fields up to 9T, which has been optimized with close interaction with the vendor. This system is housed in an ultra-high vacuum environment with a base pressure of better

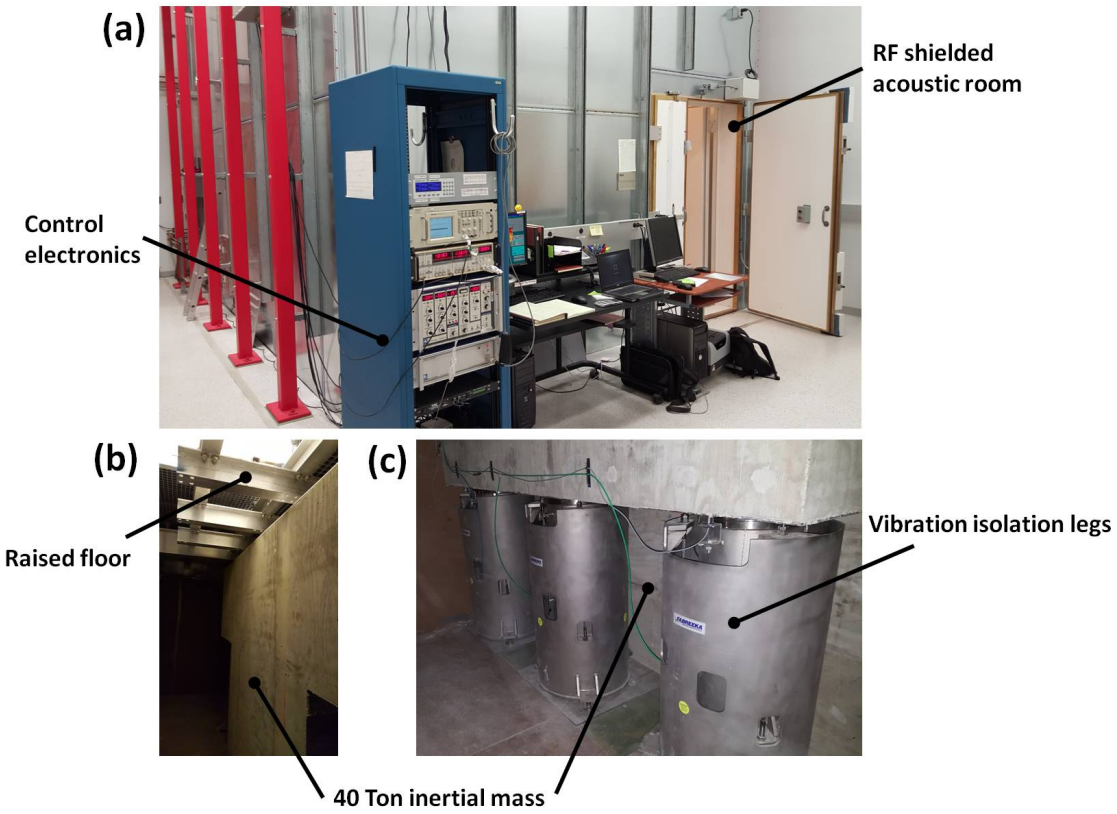

FIGURE 3.5: Photographs of one of the new scanning tunneling microscopy labs in SERC. (a) Outside view of RF shielded acoustic room, where the rack with the control electronics and the area where the computer is controlled is visible. (b) View from inside the pit showing the frame of the raised floor and the side of the 40 Ton inertial mass. (c) Three of the six massive vibration isolation legs used to raise the 40 ton inertial mass during measurements.

than 5×10^{-11} Torr with a number of additional *in situ* sample preparation and characterization capabilities that have been specially designed and added throughout the years. Figure 3.6 identifies many of the unique features of this system, which includes sample preparation by electron-beam deposition and cleavage of single crystals at low temperature.

In STM measurements it is necessary to ensure that the interfaces and surfaces un-

der investigation are clean and free of contaminants, and in most cases this is accomplished under ultra-high vacuum conditions. For some layered materials (graphite, $NbSe_2$, MoS_2, etc.), where the layers are weakly bonded by van der Waals interactions, it is possible to peel off a few layers of the top most surface (cleave) *in situ* thereby exposing an ideal flat clean surface. On the other hand, in the cases of single crystal materials which cannot be cleaved (Au, W, Ni, etc.) alternative methods of surface preparation such as ion milling or high temperature annealing can also be used for this task. During this dissertation, these cleavage and annealing processes have been optimized and routinely used for measurements of various materials. Part of this work involved developing a heating stage in the preparation chamber which allows for sample heating either by resistive heating of the sample or high voltage electron-beam heating. Additionally, a number of sample holders needed to accomodate constraints of different experiments (sample geometry, annealing temperature, type of material, etc.) have been designed to use on this heating stage. Since these sample holders offer a small cylindrical space with a maximum volume of $\sim$12 mm $\times$ 9 mm, and because it must be non-magnetic, UHV and low temperature compatible, and fit on the STM the design process is complicated, but possible.

However, the materials used in the fabrication of the S/F structures to be discussed in this dissertation cannot be cleaved. Furthermore, because the temperatures necessary to prepare surfaces by annealing are much higher than the Curie temperature of most ferromagnets this was also not an option. Instead, to provide a clean surface free of contaminants, the top-most superconducting layer of the S/F hybrid was deposited *in situ* at low temperatures using electron-beam evaporation. To accomplish these low temperature depositions a liquid nitrogen cooling stage was added to the sample preparation chamber, and the film growths optimized using different deposition parameters. For the results on the magnetically coupled S/F hybrids that will be presented, a thin insulating layer physically separates the superconductor

from the ferromagnet, which allows for the ferromagnet and insulator to be fabricated *ex situ*, where the insulator effectively serves as a capping layer. Finally, the superconductor is deposited in the UHV system connected to the microscope, preserving the cleanlinss of the surface under investigation.

While not specifically the topic of this dissertation, a large amount of work has already been done to prepare proximity coupled S/F hybrids where the superconductor and ferromagnet are in direct contact. Much of the interesting physics in these systems takes place at the interface between the superconductor and ferromagnet, and it is strongly affected by the quality and the transparency of the interface. This necessitates the need to prepare all components of the S/F structure *in situ*. However, even small concentrations of magnetic materials in a superconductor have a huge effect on the superconducting properties, and because the superconducting films fabricated in the sample preparation chamber are of extremely high quality (characteristic properties close to bulk) care must be taken when evaporating these two classes of materials in the same system. To safely accomplish this fabrication goal and eliminate the possibility of degrading the quality of the superconducting films, an auxiliary depsosition chamber with a single source electron-beam evaporator (see figure 3.6) was developed and added to the UHV system. This new chamber has already been tested, and measurements on proximity coupled S/F already underway are showing very promising results.

3.5.3 Scan head and course approach mechanism

Figure 3.7 shows the general design features of the Pan-style [57] STM scanner used during this dissertation, where the actual body of the scanner is only about the size of an adult fist. This type of scanner design is widely used due to its rigidity, which makes it less prone noise from external vibrations. The main body of the scanner is made of Titanium, which holds a sapphire prism firmly in place between six piezo

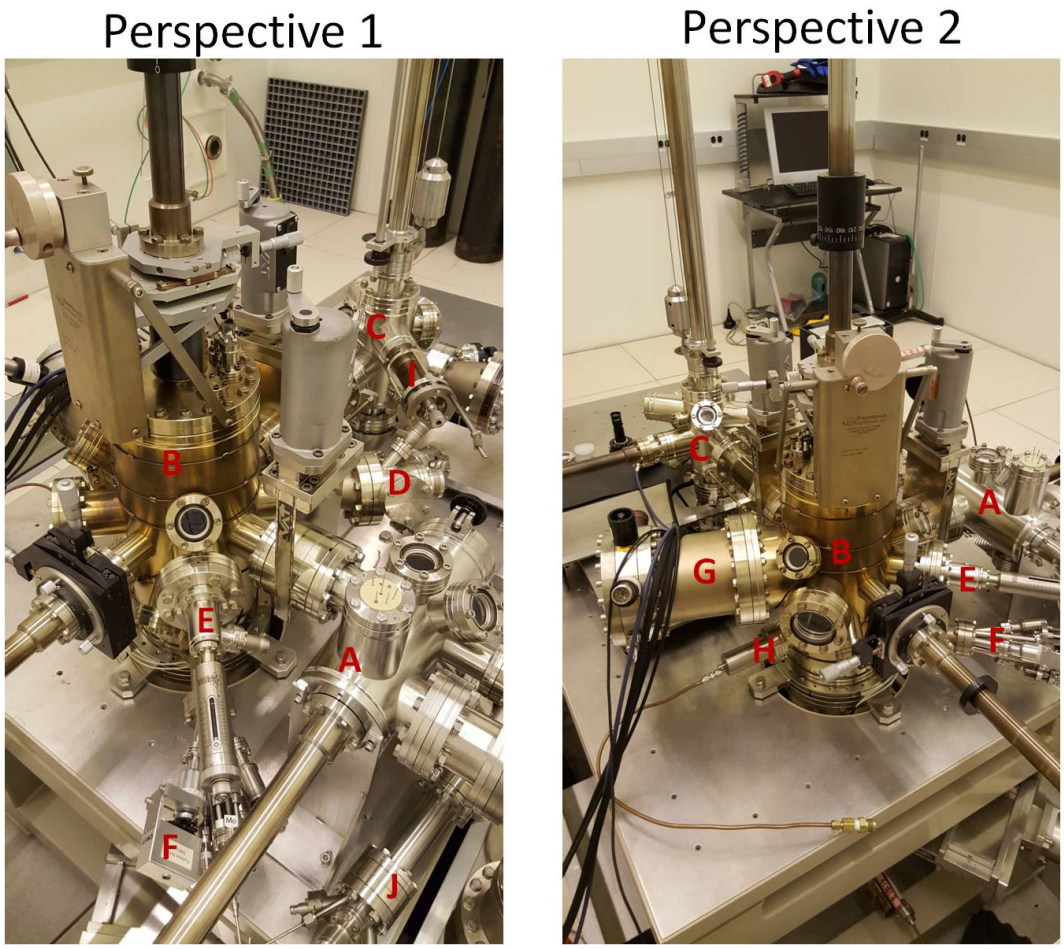

FIGURE 3.6: Images of ultra-high vacuum chambers and *in situ* capabilities for this system. (A) Load-lock chamber; (B) Preparation chamber; (C) STM chamber; (D) Ion gun for milling; (E) Electron-beam heating for tip preparation; (F) Triple source electron-beam evaporator for superconducting films; (G) Low-energy electron diffraction and Auger electron spectroscopy; (H) Liquid nitrogen feedthrough for low temperature deposition stage; (I) Low-temperature sample cleavage stage; and (J) Single source electron-beam evaporator for magnetic materials. Not shown are electrical feedthroughs for high-temperature heating for substrate preparation.

stacks. A ruby ball and plate are used to control the compression between the piezo stacks and prism, which is crucial in the kinetic behavior of the sapphire for approach. There is a hole in the center of the prism which houses the tube scanner piezo and tip. The overall mechanism of scanning using the tube scanner was briefly discussed in chapter 3, and here only the technique for coarse approach will be discussed. However, it should be noted the importance in the design of the scanner used that the tip can be changed *in situ* without breaking the vacuum. This is very important since the tip is always the least controlled component of an STM experiment, and this is actually not a feature of most ultra-high vacuum low-temperature STM systems.

It is impossible to put a tip and sample directly in place for STM experiments, being that they are separated only by a few atomic distances. A number of techniques have been developed that allow for the reproducible approach of the tip and sample depending on the design of the scanner. Slip-stick motion is the technique used for the Pan-style STM scanners described in figure 3.7, and figure 3.8 gives a step-by-step description of this operation. The party trick of pulling the table cloth out from under the plates is well known, and while the details are more complicated than dinnerware, the STM coarse approach uses the same general idea. As described by step A in figure 3.8, with zero voltage on the piezo stacks they are all in an equilibrium state, which firmly holds the sapphire prism in place. By quickly applying a voltage to one of the piezo stacks it deforms and slides against the prism, but because the other piezo stacks are stationary the prism does not move. This operation is performed sequentially for all the piezo stacks, where step B in figure 3.8 shows an intermediate stage and step C is where all piezos are deformed along the sapphire prism. It is important to note that there is no motion of the prism up to this point, and in the analogy so far it is acting like the dinner places. Now, once all of the stack piezos are deformed, the voltages are *slowly* ramped back to zero, where in this way slip-stick motion is avoided and the prism is moved forward. This operation,

which is controlled by the electronics and computer, is performed iteratively until the feedback loop senses the defined current setpoint indicating that the tip is in place above the sample surface.

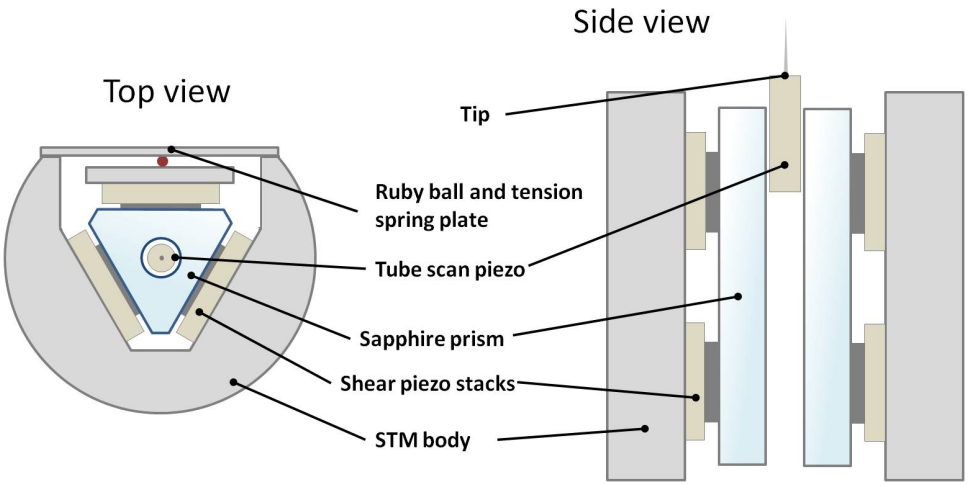

FIGURE 3.7: Schematic representation of the scanning tunneling microscope head (not to scale), which has been designed in the Pan-style [57]. Top view: At the center of a polished sapphire prism is the piezoelectric tube scanner which controls the x-y-z motion of the tip during scanning. The sapphire prism is held in place by compression between the shear piezoelectric stacks used for slip-stick motion during coarse approach (discussed later in figure 3.8). The force between the sapphire prism and the stack piezos is controlled by the tension on a leaf spring plate. Side view: Alternative perspective of the scan head.

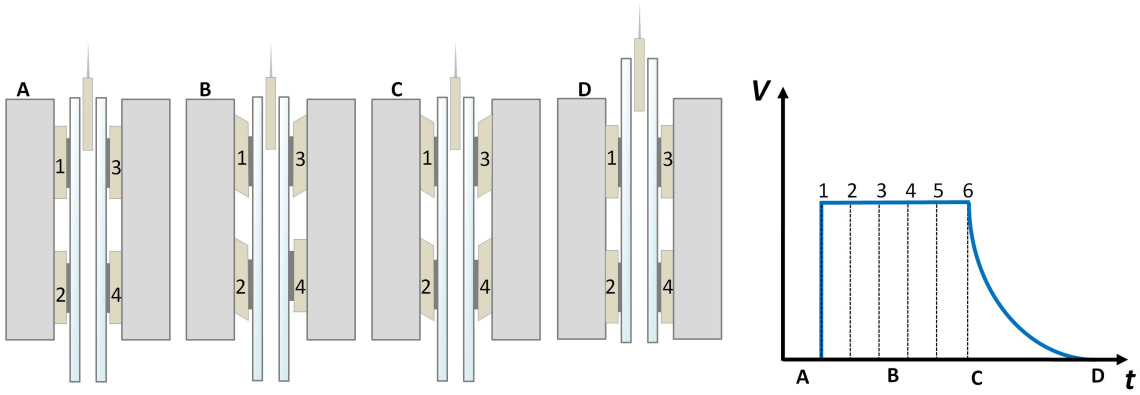

FIGURE 3.8: The sequential images show the method of course approach in scanning tunneling microscope measurements. Cartoons of the motion correspond with a plot of the applied voltages with time on the piezo stacks. In position (**A**) there is no voltage on the stack piezos and friction holds the sapphire prism rigidly in place against gravity. By quickly applying a high voltage to only one of the stack piezos, it deforms and is repositioned down the prism in a slip-stick motion. This is very similar to the trick of pulling a table cloth out from underneath the plates, where here the prism is a plate and the table cloth is the stack piezo. During this operation, the force from the other stack piezos holds the prism rigidly in place. This is done sequentially for all six piezos. (**B**) An intermediate step where only three of the stack piezos have deformed. (**C**) With all of the piezos uniformly deformed along the prism body, the voltage is slowly returned to zero. (**D**) By ramping the voltage down more slowly slip-stick motion is avoided and the friction between the piezos and the prism causes it to move forward.

CHAPTER 4

SUPERCONDUCTING LEAD FILMS

4.1 Ultrathin Pb films

This chapter is comprised the original manuscript of an article, S. A. Moore *et al.* "Low-temperature scanning tunneling microscopy and spectroscopy measurements of ultrathin Pb films," Supercond. Sci. Technol. **28**, 045003 (2015). The final version, available from the publisher, has undergone substantial modifications during the review process.

The number of studies on systems with reduced dimensionality has grown substantially in recent years. Due largely to refinements in materials processing as well as characterization techniques, it is now possible to fabricate and study systems and address fundamental questions from new perspectives. Spatially confined systems can be realized in the form of ultrathin films [58, 59], interfaces [60, 61], and other mesoscopic structures [62, 63, 64]. Part of the interest in 2D systems lies in the fact that as the dimension of a system is continuously reduced quantum effects begin to play a crucial role, which can result in properties that are very different than those found in the bulk. Systems which have attracted considerable attention are Pb(111) ultrathin films and islands grown on semiconducting and metallic substrates, due to

novel quantum size growth modes [65, 66, 67, 68]. Although a considerable effort has been put forward to understand the properties of nanoscale islands of this material, significantly less work has been done in continuous ultrathin films. Since the quantum size effects can modulate the electronic properties around the Fermi energy, it is important to understand the properties in all regimes of film growth [7, 69, 70, 71]. As the thickness of the film is varied, in addition to the quantum size effects which can strengthen or weaken superconductivity by modulating the density of states around the Fermi energy, there will be a modification to the electron-phonon coupling strength [72]. For thinner films the phonon frequencies are lowered, which results in a decreased electron-phonon coupling strength, and conversely on a weakening of the superconductivity. Quantum size effects and electron-phonon coupling can compete in an unusual way, therefore affecting the superconducting state. To investigate the nature of this competition, the dependence of the superconducting properties on the quantum size effects and electron-phonon coupling in the case of Pb films and islands has been widely studied both experimentally and theoretically [7, 73, 74, 75, 76, 77, 78]. Low temperature scanning tunneling microscopy and spectroscopy measurements on the superconducting properties of ultrathin Pb films are presented. Measurements have been performed on 30 nm Pb(111) films to characterize the superconducting as well as the normal state. The spectroscopy in the normal state at large energies shows clear evidence of quantum size effects, but the superconducting properties are still close to that of the bulk. These ultrathin films clearly remain in the strong-coupling regime, with a BCS ratio of 4.7. Measurements on a 3 nm Pb film, instead, show a weak-coupling behavior. The thinner films also show superconducting properties much different from the bulk, with a reduced transition temperature, energy gap, and coherence length.

Low temperature scanning tunneling microscopy and spectroscopy (LT-STM/STS) experiments have been performed on ultra-thin films of Pb(111) using a Unisoku

UHV ^{3}He system. The system can reach temperatures as low as 350mK and magnetic fields as high as 9T, with a base pressure in the 10^{-11} Torr range. The STM is connected to a preparation chamber equipped with an e-beam evaporator and LN cooling stage for the *in situ* preparation of samples at low temperature. The films were made by depositing high-purity (5N) Pb from a Mo crucible onto various substrates. The deposition rates were calibrated *ex situ* by measuring the thickness using room temperature atomic force microscopy. Rates of approximately 0.6 ML/min and 0.2 ML/min were used for the 30 nm and 3nm Pb films, respectively. Substrates of SiO_2 were used for the growth of 30 nm films, and cleaved HOPG was used for the growth of 3 nm films. All substrates were held at 150 K during deposition, and then gradually allowed to warm to room temperature before being transferred to the STM held at 1.5 K. Electro-polished Pt-Ir tips were used for all measurements.

4.1.1 Continuous 30 nm Pb films

For many fcc metals grown on amorphous substrates there is a strong predisposition for growth to proceed in the (111) direction [79, 80]. In the particular case of Pb films, this preferred orientation is also preserved when the substrate is held at reduced temperatures during deposition, and allowed to gradually warm to room temperature [5]. In this case growth should proceed first with the nucleation of large individual (111) oriented crystallites, which eventually become well connected to form a continuous film [81]. Annealing at room temperature allows the boundaries in between these crystallites to soften, and eventually leads to a very clean and flat film. Figure 4.1(a) shows the typical morphology of a continuous film over a large area, with terraces that are approximately one to two monolayers in height (1ML=0.286nm). A differential conductance spectrum (dI/dV), using the standard ac lock-in technique with a typical modulation voltage of 0.2mV, has been acquired in the normal state on one of these flat terraces and is shown in figure 4.1(b). The

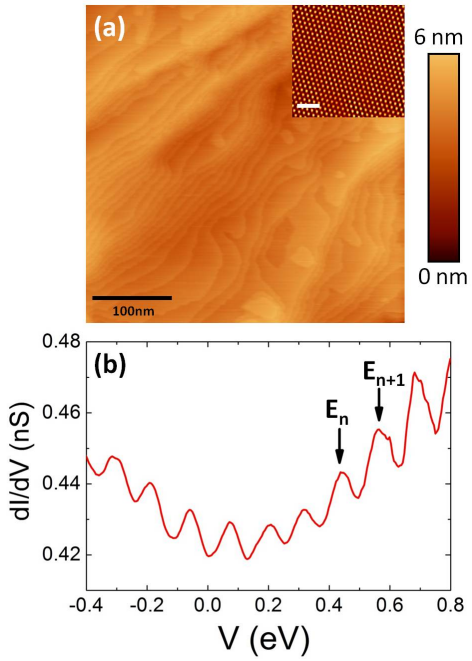

FIGURE 4.1: (a) 400 nm×400 nm constant current STM topography image of the Pb (111) surface for a 30 nm film, revealing continuous flat regions over large areas. Color scale indicates approximate height, and tunneling conditions were V=-100 mV and I=10 pA. Inset shows 10 nm×10 nm atomic resolution image taken on a terrace with tunneling conditions V=-25 mV and I=50 pA. (b) Differential conductance spectrum showing periodic energy dependent resonance peaks due to the presence of quantum well states. The spectrum has been acquired in the normal state at T=1.6 K and H=1500 Oe, with initial tunneling conditions of V=-0.8V and I=200 pA.

spectrum reveals defined resonance peaks at discrete energy levels, which are due to quantum effects that stem from the confinement of the electrons between the film interfaces. These resonance peaks are often referred to in literature as quantum well states (QWS) because of the behavior that is reminiscent of the quantum well problem. For Pb(111), these quantum effects are easily realized because the interlayer spacing is a close multiple of the Fermi wavelength, $d \approx 0.66\lambda_F$ [79], and it is well known that Pb films with this orientation support the existence of QWS well beyond the thicknesses found for other materials [5, 82, 83].

The positions of the QWS can be understood in terms of the Bohr-Sommerfeld

quantization rule:

$$2k(E)Nd + \phi_i(E) + \phi_s(E) = 2n\pi \tag{4.1}$$

where k is the electron wavevector perpendicular to the surface, N is the number of monolayers, n is the quantum number, $\phi_{i,s}$ are the energy dependent phase shifts at the vacuum and substrate interfaces, and d is the lattice constant of Pb in the (111) direction. In the simplest case, the system can be treated as an infinite quantum well where the quantized energy states will follow the familiar $E_n \approx n^2$ dependence. As a result, given the locations of the QWS peaks, it should be possible to directly calculate the film thickness because it is related to the width of the well. However, it is generally not known *a priori* which quantum number applies to which peak since the ground state is not well defined in such a system. This problem can be overcome by noting that a resonance peak located at 0.56 eV corresponds to the wave vector $k{=}3\pi/2d$, allowing for the unique identification of $n{=}(3/2)N$ for this particular peak [6]. Taking the difference of energy levels between E_n and E_{n+1} in the infinite quantum well model, the energy separation between adjacent peaks is:

$$\Delta E = \frac{\pi^2(2n+1)\hbar^2}{2m^* d^2 N^2}, \tag{4.2}$$

where m^* is the electron effective mass. By using the peaks at $E_n{=}0.44$ eV and $E_{n+1}{=}0.56$ eV, a thickness of 30 nm ($N{=}100$ MLs) is calculated, using for the effective mass $m^*{=}1.14$ m_0 [79]. This is in excellent agreement with the value of thickness expected from the calibration of deposition parameters. Once the thickness of the film is identified, a good estimate of the Fermi velocity can be obtained using the relationship between the energy separation and the width around the Fermi level given by $\Delta E{=}\hbar\pi v_F/dN$. This gives that $v_F \approx 1.74{\times}10^8$ cms^{-1}, which is in good agreement with other measurements on Pb films [78].

Representative dI/dV spectra taken as a function of temperature are shown in

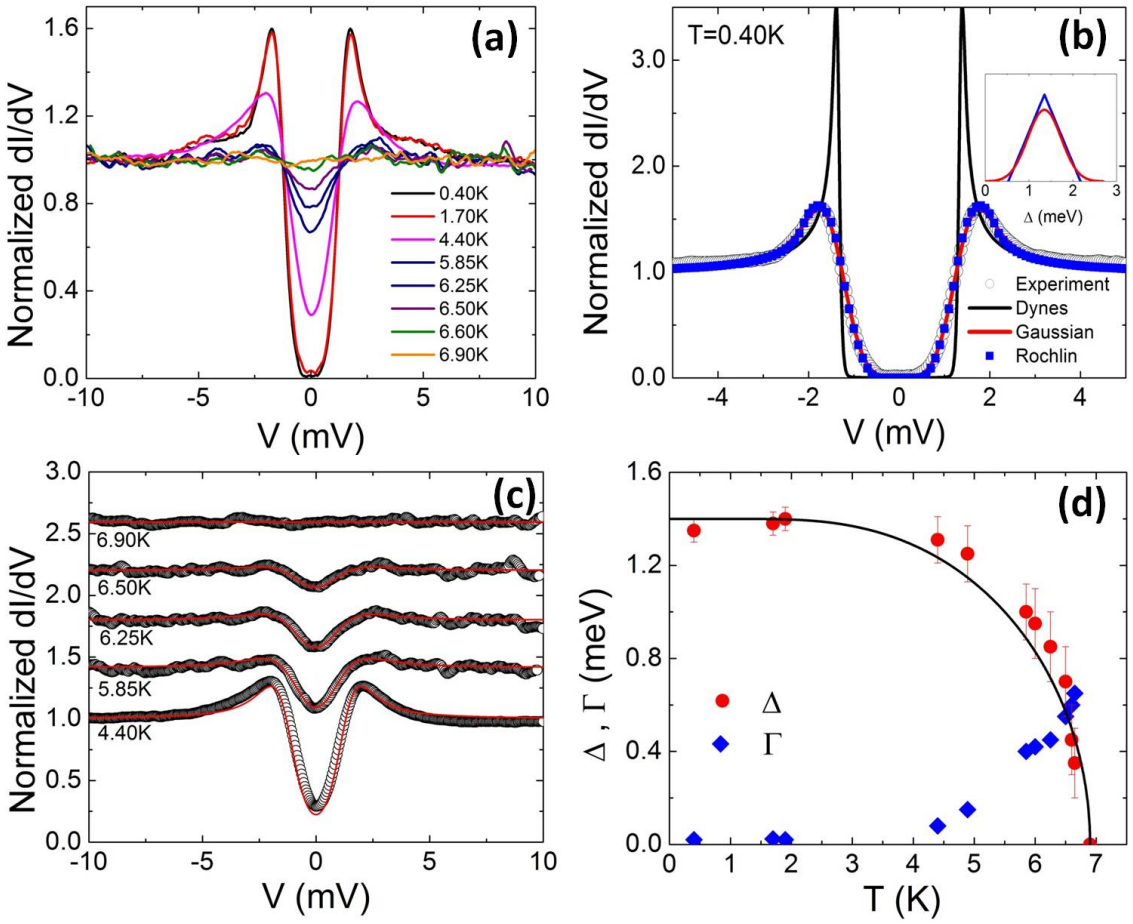

FIGURE 4.2: (a) Differential conductance (dI/dV) spectra taken in the same location as a function of temperature, which have been normalized using to spectra above the transition temperature in the normal state. (b) Comparison of fits of the normalized differential conductance spectra taken at 400 mK (open black circles) using the Dynes formula (black line), Gaussian gap distribution (red line), and Rochlin triangular gap distribution (blue squares). In all cases, the central gap value and broadening parameter Γ used were 1.35meV and 0.002meV, respectively. The red and blue lines of the inset show the forms of the Gaussian and triangular distributions, respectively. (c) dI/dV spectra (black circles) taken at higher temperatures and the corresponding fits using only the Dynes formula for the density of states (red lines), showing that at higher temperature the effect of the energy gap anisotropy is less critical due to thermal smearing. (d) Energy gap (red dots) and broadening parameter (blue diamonds) as a function of temperature extracted by from fits of the temperature dependent spectra. The black line is a BCS curve $\Delta(\mathrm{T})/\Delta_0=\tanh[T_c\Delta(T)/T\Delta_0]$, with T_c=6.9 K and Δ_0=1.39$\pm$0.05 meV.

figure 4.2(a). Normalization of the data has been performed using spectra taken above the transition temperature in the normal state. The spectra show qualitatively the broadening of the quasi-particle coherence peaks with increasing temperature, as well as an increase of the zero bias conductance (ZBC) value. To gain a quantitative understanding of the energy gap evolution, the normalized dI/dV spectra is fit using the function for the tunneling between a normal metal and a superconductor:

$$G(V) = G_{nn}\frac{d}{dV}\int_{-\infty}^{+\infty} N_S(E,\Gamma,\Delta)\left[-\frac{\partial f(E+eV)}{\partial(eV)}\right]dE \tag{4.3}$$

where G_{nn} is the conductance of the junction when both electrodes (tip and sample) are in the normal state, f is the temperature dependent Fermi distribution function, and N_S is the superconducting density of states [17]. For the density of states of the superconductor the Dynes modified formula is used,

$$N_S(E,T,\Gamma) = Re\left[\frac{|E+i\,\Gamma(T)|}{\sqrt{(E+i\,\Gamma(T))^2-\Delta(T)^2}}\right] \tag{4.4}$$

which is the BCS density of states with the addition of the phenomenological parameter Γ to account for broadening due to a finite quasi-particle lifetime [84]. As shown in figure 4.2(b) the fit using the Dynes formula with Δ=1.35 meV and Γ=0.002meV does not capture the features of the dI/dV spectra taken at the lowest temperature. In fact, it is impossible to adequately fit these spectra using the Dynes density of states, which can be understood by noting that Pb has a well known energy gap anisotropy over the Fermi surface [85, 86, 87]. Following the work of Rochlin, a triangular gap distribution of the form

$$g(x) = \begin{cases} A(x-\Delta_m), & \Delta_m \leqslant x \leqslant \Delta_{ave} \\ A(\Delta_M - x), & \Delta_{ave} \leqslant x \leqslant \Delta_M \\ 0 & \text{elsewhere} \end{cases} \tag{4.5}$$

is introduced, where A is a normalization constant, Δ_m is the minimum value of the energy gap, Δ_M is the maximum value, and Δ_{ave}=(Δ_m+Δ_M)/2 is the average value of the gap [86]. The convolution of this distribution and the Dynes density of states

$$N_S(E,T,\Gamma) = Re\left\{ \int_{\Delta_m}^{E} \frac{|E + i\,\Gamma|}{\sqrt{(E + i\,\Gamma)^2 - x^2}} g(x)dx \right\} \tag{4.6}$$

gives a density of states for the superconductor which incorporates the triangular distribution of gap values. The curve represented with blue squares in figure 4.2(b) shows the fit using this modified Dynes density of states with Δ_m=0.525 meV, Δ_M=2.175 meV and Γ=0.002 meV, and clearly captures the details of the experimental dI/dV spectra. As a comparison, the triangular distribution is substituted with a Gaussian distribution of gap values with the central value of Δ=1.35 meV, σ=0.38 meV and Γ=0.002 meV to fit the spectra (red line in figure 4.2(b)) [88]. The triangular and Gaussian distributions of gap values both fit the low temperature spectra very well for the same central gap and broadening values, despite having slightly different forms (inset of figure 4.2(b)). Figure 4.2(c) shows a series of dI/dV spectra taken at higher temperature (black circles), and fit using only the Dynes density of states (red lines). Because of the thermal smearing, the spectra at higher temperatures can be fit without taking into account the anisotropy. If the energy resolution required to see the anisotropy effects is considered as the difference between the maximum and minimum gap values from the model triangular distribution, Δ_M-Δ_m=1.65meV, is is seen that a temperature of around 4K is sufficient to provide enough thermal smearing to overshadow the anisotropy.

The resulting gap values and broadening parameters extracted from these fits as a function of temperature are shown in figure 4.2(d). The temperature dependence of the energy gap has been fit using the equation $\Delta(T)/\Delta_0$=tanh[$T_c\Delta(T)/T\Delta_0$] [89]. A good fit of the data is obtained with Δ_0=1.39$\pm$0.05 meV and T_c=6.9 K. From the

dimensionless ratio $2\Delta/kT_c$=4.7 it is found that the films are in the strong-coupling limit even at this reduced thickness, which is in agreement with other measurements [85, 86, 90].

In the case of type II superconductors in the presence of an applied magnetic field, vortex imaging can be performed by acquiring the zero bias conductance (ZBC) across the surface. The contrast in the conductance map is obtained by the change of the ZBC inside (normal state) and outside (superconducting state) the vortex core. The ZBC map in figure 4.3(b) shows the vortex configuration with figure 4.3(a) being a topography taken at the same time. The relationship between intervortex distance and the magnetic field is given by $d^2=2\phi_0/\sqrt{3}H$ [91], which yields, for H=600 Oe, a distance of 200 nm for a perfect triangular vortex lattice [91, 24]. Although the lattice is slightly distorted, the average inter-vortex spacing still falls around 200nm.

Analysis of the vortices can provide extremely valuable information about critical superconducting properties. Indeed, the radius of a superconducting vortex provides a convenient measure of the Ginzburg-Landau coherence length. It is possible to extract the spatial dependence of the ZBC across a vortex by directly taking a line cut from the ZBC map. An alternative way is to acquire spatially dependent dI/dV spectra across the vortex center. A series of characteristic spectra, acquired along the dashed line shown in figure 4.3(b), are reported in figure 4.3(c). The spectra show an increase in ZBC near the center of the vortex, but they also show a peculiar peak at the center. As shown in the pioneering work on $NbSe_2$ by Hess *et al.* [92], quasiparticle bound states can exist in the center which can lead to ZBC values greater than one. Such a bound state can only exist in the vortex core in the clean limit when the mean free path is much larger than the coherence length ($l >> \xi$). The presence of the bound state provides a convenient indicator for the vortex center, and plotting the normalized zero bias conductance as a function of position away from this point (figure 4.3(d)), gives that $\xi_{GL}(1.5\text{K})\approx$54 nm. This value of ξ_{GL} indicates

that the films are in the clean limit since the interface scattering limited mean free path for thin films, which is given approximately by two times the thickness [75, 93], is $l \approx$60 nm.

Using $H_{c2}=\phi_0/2\pi\xi^2_{\rm GL}$ ($\phi_0=2.07\times10^{-7}$ G cm^2), it is found that $H_{c2}\approx1130\pm50$ Oe for these films [17]. Although this information provides the upper limit for the magnetic field that can be applied before the superconducting film becomes normal, it does not provide any detailed information for the mixed state. In figure 4.4(a) characteristic dI/dV spectra taken at low temperature as a function of magnetic field are shown. The dI/dV show a clear reduction in the coherence peaks and increase in the ZBC as the magnetic field is increased, which is similar to that seen for the temperature dependence. To quantify this progression, the Dynes density of states is used to fit the spectra. The values of Δ and Γ found from these fits are plotted as a function of the applied field in figure 4.4(b), and in this case the value of Γ needed to fit the data increases very rapidly compared to the decrease in the gap value. The finite lifetime parameter incorporates many broadening terms such as instrumental, thermal, etc. The application of a magnetic field limits the quasiparticle lifetime by breaking the time-reversal symmetry, which acts to scatter the quasiparticles and smear the superconducting features. However, at high magnetic fields there is a tendency for $\Gamma>\Delta$, where the appropriateness of the use of the broadening parameter becomes questionable [94]. Nevertheless, the extracted values of the energy gap are plotted, and compared to the $\Delta = \Delta_0[1-(H/H_{c2})^2]^{1/2}$ dependence (solid line in figure 4.4(b)) expected from Ginzburg-Landau theory with $\Delta_0=1.42\pm0.05$ meV and $H_{c2}=1130\pm50$ Oe [95]. Knowledge of both the Δ(T) and Δ(H) behavior of the film forms a fairly complete understanding of the entire superconducting phase diagram.

4.1.2 Disordered 3nm Pb films

In contrast to the morphology of the 30 nm films, the STM topography in figure 4.5(a) shows that the thinner 3 nm Pb films grown on HOPG do not show such large flat surfaces. Instead, the system is comprised of well connected layers of small hexagonally shaped Pb crystallites, with an average diameter of around 10 nm. Figure 4.5(b) shows a characteristic dI/dV spectrum acquired directly on top of one of the Pb crystallites, which reveals a strong peak at 0.8 eV. The large energy spacing and low number of peaks is expected theoretically because the energy separation is inversely proportional to the square of the thickness. Without the stationary peak at 0.56 eV used in the case of the 30 nm film, it is not possible to calculate exactly using the quantum well model the thickness of the Pb film on HOPG for a single film. However, a comparison with the position of the peak with other values found in literature indicates a thickness no greater than 10 ML [96, 6]. This is in agreement with the expected thickness of 3 nm using the calibrated deposition parameters.

Electron-phonon coupling in ultrathin films often changes as a function of the thickness. This change can come about from a variety of reasons, such as modifications to the lattice due to increased strain. The dimensionless BCS ratio provides a simple way to distinguish strong and weak coupled systems, where it is given by BCS theory to be $2\Delta/k_BT_c \approx 3.52$ in the latter case. Temperature dependent dI/dV spectra have been acquired on the 3 nm film using the same technique described for the 30 nm film. As figure 4.6(a) shows, even at low temperatures the gap value for the thinner film is much reduced which is not an unexpected result. Again the spectra is fit using the Dynes formula (figure 4.6(b)), and in this case it provides a sufficient fit for all temperatures measured without the addition of the anisotropy term. The much reduced mean free path in this case ($l \approx 2d \approx 6$ nm) washes out any anisotropy even at the lowest temperature. Fitting the extracted Δ and Γ within the BCS model

gives Δ_0=0.64±0.05 meV and T_c=5.3 K, which makes $2\Delta/k_BT_c$≈2.81. This value is much lower than the value found for the 30 nm films and it is even lower than those found for comparable thickness films and islands on Si(111) [58, 59, 97]. However, this low value does agree with the overall trend of a decreasing BCS ratio expected for decreasing island size, which can be attributed to a decrease in electron-phonon coupling [97].

A topography image and its corresponding conductance map at the Fermi energy that have been taken in the mixed state, at 1.5 K and with a magnetic field applied along the c-axis of the film H=800 Oe (field cooled), are shown in figures 4.7(a) and (b), respectively. The vortex image shows a perfect triangular lattice with an average inter-vortex distance of about 180 nm at H=800 Oe. Detailed dI/dV spectra acquired across the vortex core (figure 4.7(c)) can be used to extract the ZBC value as a function of position. As in the case of the 30 nm film, the radius of the vortex is taken to be indicative of the coherence length, which as figure 4.7(d) shows, is ξ_{GL}≈25 nm in the case of the 3 nm film. Using this value of ξ_{GL} in the relationship linking the coherence length to the upper critical field gives H_{c2}≈5300±50 Oe, which is in the same range found for Pb films of a similar thickness grown on Si(111) [74].

Measurements on ultrathin films of Pb in the superconducting state using LT-STM/STS have been presented. The results show that for 30 nm films grown on SiO_2 the transition temperature and energy gap lie close to the bulk values, and are in the strong-coupling regime. Differential conductance measurements of the vortex state show that the films are in the clean limit as demonstrated by the presence of the bound state in the vortex core. Comparison with 3 nm films, grown on HOPG, shows that the thinner film is in the weak-coupling regime. Moreover, the absence of the bound state in the vortex core indicates a transition to the dirty limit.

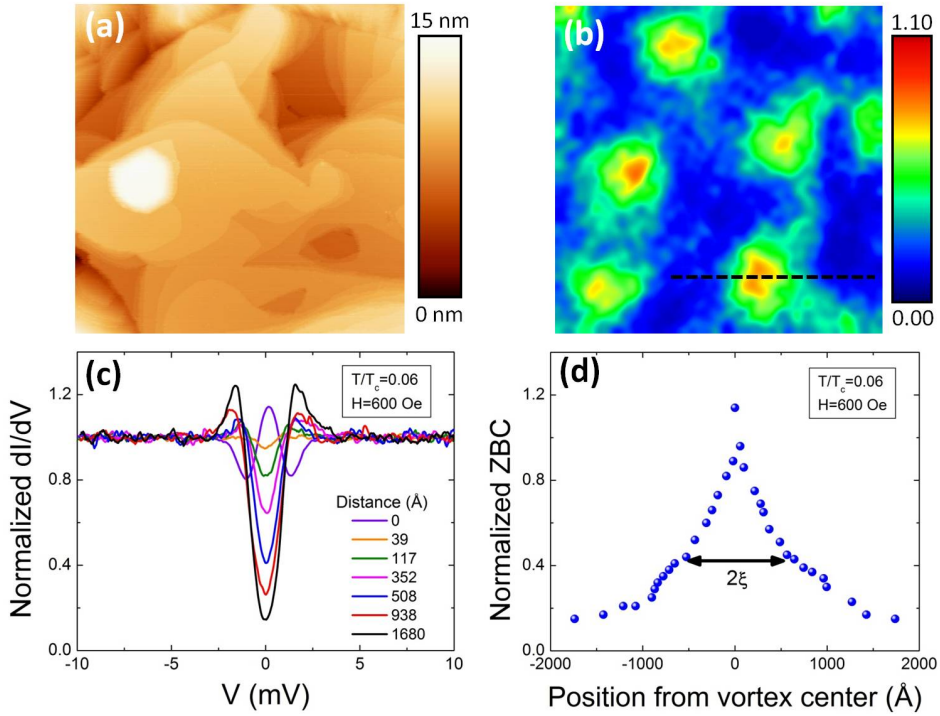

FIGURE 4.3: (a) 445 nm×445 nm STM topography image of a 30 nm Pb film showing that the film is smooth and continuous over large areas. Color scale indicates approximate height. (b) 445 nm×445 nm zero bias conductance map taken concurrently with the topography in (a), which shows the Abrikosov vortex lattice at T=400 mK and H=600 Oe. Blue regions are superconducting and red regions are the normal vortex core. Color scale represents ZBC values normalized to the map taken at the same location at -10mV. (c) Normalized differential conductance as a function of position across the vortex (black dashed line in (b)). (d) Evolution of the zero bias conductance as a function of position from the vortex core extracted from the normalized spectra, which shows that the coherence length is $\xi_{GL}(1.5\text{K})\approx 54$ nm. Tunneling conditions were V=-20 mV and I=100 pA for the images, and V=-10 mV and 100pA for the spectroscopy.

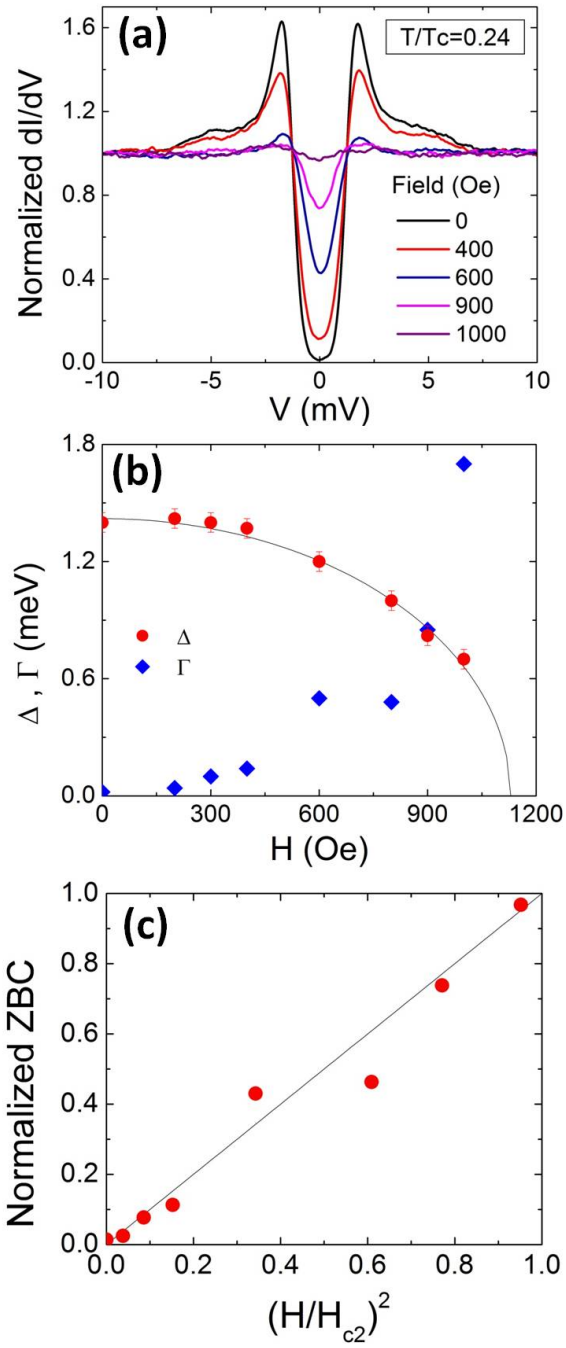

FIGURE 4.4: (a) Normalized differential conductance spectra showing the energy gap dependence on applied magnetic field. (b) Values of the energy gap (red circles) and Dynes broadening parameter (blue diamonds) found from fits of the spectra to equations 3 and 4. The black line is a fit to $\Delta=\Delta_0[1\text{-}(H/H_{c2})^2]^{1/2}$, where $\Delta_0=1.42\pm0.05$ meV and $H_{c2}=1130\pm50$ Oe have been used. (c) Normalized ZBC values versus $(H/H_{c2})^2$ with $H_{c2}=1030\pm50$ Oe showing a linear relationship.

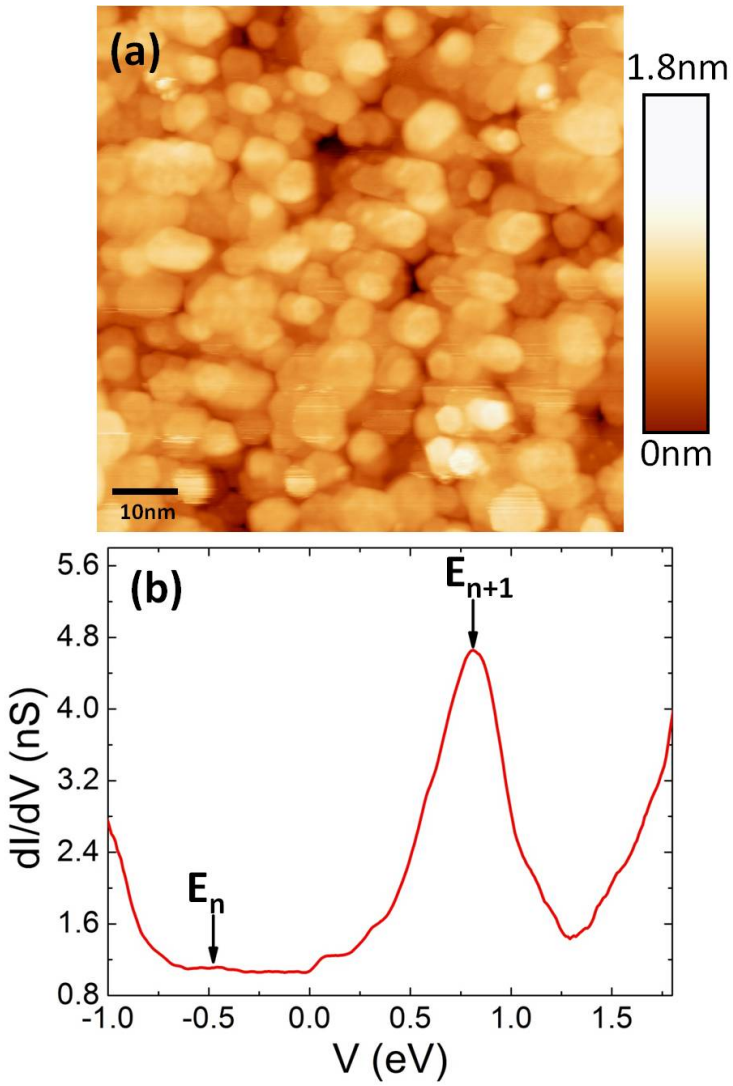

FIGURE 4.5: 80 nm×80 nm constant current STM topography image for a 3 nm Pb film. Color scale represents approximate height, and tunneling conditions were V=-100 mV and I=10 pA. (b) Differential tunneling conductance spectra showing two energy dependent peaks due to the presence of quantum well states. The spectra has been acquired at T=8 K and H=1000 Oe, with setpoint V=-0.7V and I=50 pA.

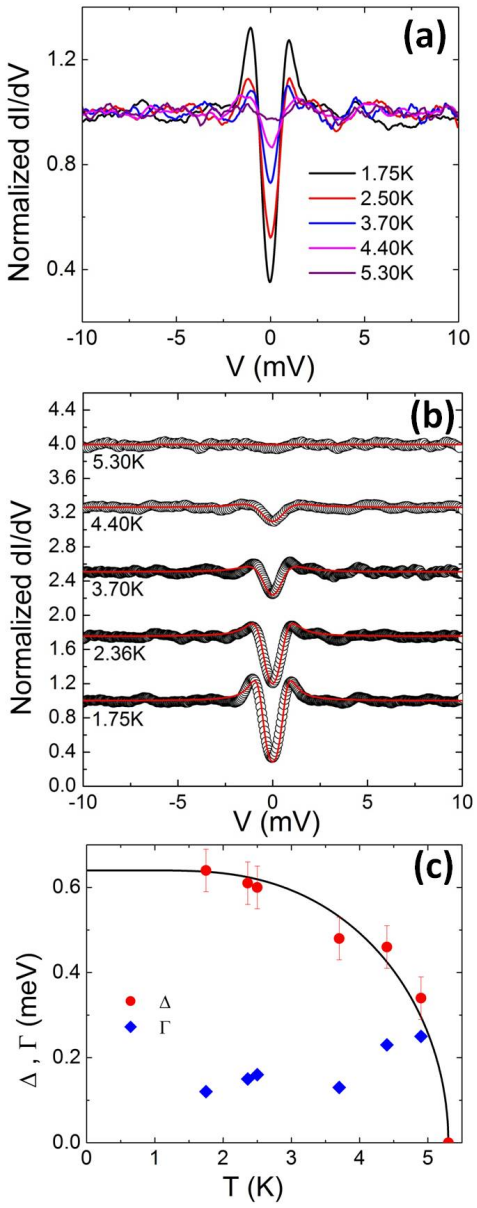

FIGURE 4.6: (a) Normalized differential conductance spectra taken as a function of temperature for the 3 nm Pb film. (b) Energy gap (red dots) and Dynes broadening parameter Γ (blue diamonds) as a function of temperature extracted by fitting the spectra with equations (3) and (4). The black line is the BCS function with T_c=5.3 K and Δ_0=0.64$\pm$0.05 meV.

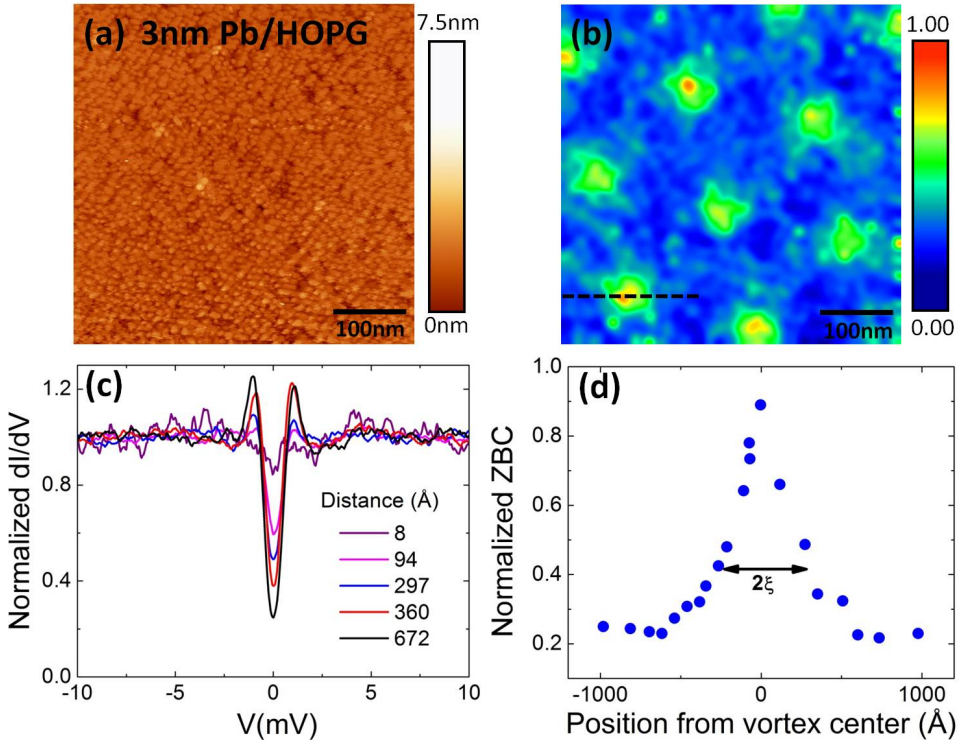

FIGURE 4.7: (a) 470 nm×470 nm STM topography showing a dense distribution of small interconnected Pb crystallites which form a continuous film. Color scale indicates approximate height. (b) 470 nm×470 nm zero bias conductance map taken concurrently with the topography in (a), which shows the Abrikosov vortex lattice at T=1.5 K with H=800 Oe. Blue regions are superconducting and red regions are the normal vortex core. Color scale represents normalized ZBC values. (c) Spectra across the vortex as a function of position from the core. (d) Evolution of the zero bias conductance as a function of position from the vortex core, which shows the coherence length ξ_{GL}=25 nm. Tunneling conditions were V=-10 mV and I=100 pA for all images and spectroscopy.

CHAPTER 5

NUCLEATION OF VORTICES IN SUPERCONDUCTOR/FERROMAGNET STRUCTURES

This chapter is comprised of an article, M. Iavarone, S. A. Moore *et al.* "Influence of Domain Width on Vortex Nucleation in Superconductor/Ferromagnet Hybrid Structures," J. Supercond. Nov. Magn. **28**, 1107 (2015).

Superconductor/ferromagnet (S/F) systems have been widely studied in recent years [98, 11]. If a thin layer of oxide is placed between the superconductor and the ferromagnet the stray field of the ferromagnet affects locally the superconductivity. In this case the interaction is orbital in nature, and can give rise to a variety of new phenomena such us domain wall superconductivity and reverse domain wall superconductivity [99]. Additionally, these types of S/F systems also hold the potential to increase the critical current density of the superconducting layer through the interaction of the vortices with the magnetic moment of the underlying magnetic domain [100, 101]. Furthermore, if the ratio of magnetic domain width to superconductor thickness is properly tuned vortex-antivortex pairs are formed in zero applied magnetic field [9, 33, 36]. If the magnetic domain width, instead, is below the

minimum threshold to allow the formation of spontaneous vortex-antivortex pairs vortices can still be induced in the superconducting layer when applying an external magnetic field [36, 102].

The effect of an unbalanced size distribution of positive and negative magnetic domains in the ferromagnetic layer on the vortex nucleation in the superconducting layer is studied. In recent publication, by changing the parameters of the multilayer ferromagnet in the S/F system, there has also found a strong dependence on domain width for the appearance of domain wall and reverse domain superconductivity [14]. This suggests a robust size dependence on these interesting states of S/F systems, many of which can easily be overlooked using more global measurement techniques.

The superconductor/ferromagnet system investigated consists of a 30 nm ultrathin film of Pb deposited on top of a multilayer Co-Pd ferromagnet. The multilayer Co-Pd system was made by successive deposition of 2 nm Co and 2 nm Pd onto a Si(100) substrate using dc magnetron sputtering with an in-plane magnetic field of a few hundred Oe applied to the substrate to help promote perpendicular magnetic anisotropy [103]. A 10 nm insulating layer of Al_2O_3 was immediately deposited onto the Co-Pd multilayer system prior to removal from vacuum by rf sputtering of aluminum in a partial pressure of oxygen. This insulating layer prohibits proximity effects between the superconducting and ferromagnetic films. Ultrathin films of Pb were deposited *in situ* in a vacuum in the range of 10^{-11} Torr onto the Co-Pd/Al_2O_3 system using e-beam evaporation from a Mo crucible at a rate of approximately 0.2 nm/min. The substrate was held at 150 K during deposition, and then gradually allowed to warm to room temperature over a few hours before being transferred to the already cold scanning tunneling microscope.

Magnetic characterization of the domain structure of the Co-Pd/Al_2O_3 multilayer system was carried out using room temperature magnetic force microscopy using silicon cantilevers coated with a layer of Co-Cr alloy (MESP MFM probes by Bruker

Corporation, Santa Barbara). These probes have a spring constant of 1-5 N m^{-1}, a resonant frequency of 60-90 kHz, and a coercive field of nearly 400 Oe. Images were taken using a Bruker Multimode 8 atomic force microscope in the lift-mode regime at a lift height of 30 nm.

Low temperature scanning tunneling microscopy and spectroscopy (LT-STM/STS) measurements were carried out, with the tunneling spectroscopy performed using the standard lock-in technique with an ac modulation of 0.2 mV at 373 Hz. The conductance maps were acquired while scanning the tip over the sample surface at high voltage (-20 mV), periodically pausing scanning to disable height feedback, and acquiring the lock-in signal at the Fermi energy. Topography was always acquired simultaneously to ensure the location where the spectroscopic information was recorded. All differential conductance spectra (dI/dV) were taken with the same tunneling parameters with the junction stabilized at V=-10 mV, I=100 pA.

Although STM is not sensitive to stray fields, the information of the underlying magnetic template is imprinted in the vortex configuration in the superconducting layer, which will be effected by the presence of an external magnetic field. Indeed, above each magnetic domain the stray field will either be compensated or strengthened by the external field and therefore the density of vortices will be reflect the underlying magnetic pattern. Figure 5.1(a) shows a $20\mu m \times 20\mu m$ room temperature magnetic force microscopy image, which exhibits the characteristic domain structure of the samples. Domains of opposite polarity have slightly different widths throughout the image, with an average width of about 200 nm. Ultrathin films of Pb grown in UHV on the oxide coated ferromagnet have surfaces with large areas of atomically flat terraces [8], as shown in figure 5.1(b). A zero bias conductance (ZBC) map acquired concurrently with the topography of figure 5.1(b) in zero applied external magnetic field is shown in figure 5.1(c). Regions of higher conductance (more normal) in this ZBC map represent Abrikosov vortices. The image shows the presence

of only a few vortices due solely to the ferromagnet stray field.

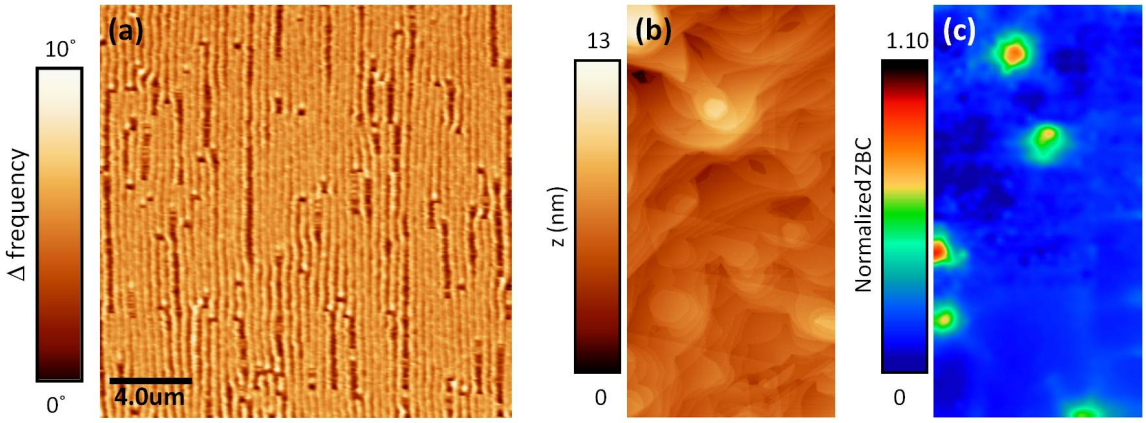

FIGURE 5.1: (a) 20 μm×20 μm room temperature magnetic force microscopy image taken in lift height mode showing the magnetic domain structure of our samples. (b) A 1.13 μm×0.57μm low temperature scanning tunneling microscopy topography showing the morphology of the ultrathin Pb film. Tunneling conditions during scanning were V=-10 mV and I=100 pA. (c) A 1.13 μm×0.57μm zero bias conductance map taken concurrently with the topography in zero applied field showing a low density of vortices (red) generated by the stray field of the underlying ferromagnet and surrounded by large superconducting regions (blue).

In order to understand the underlying magnetic domain structure magnetic field dependent ZBC maps were acquired. In figures 5.2(a-c), ZBC maps in the presence of magnetic fields H=0 and ±500 Oe are reported. The maps clearly show that vortices arrange preferentially along stripes, with an increasing density for higher applied magnetic fields. For the opposite polarity, vortices are located along previously unoccupied stripes. Evidently, the vortex configuration reflects the nature of the underlying stripe magnetic domains of the ferromagnet. When an external magnetic field is applied, the domains anti-parallel to the external field will be at least partially compensated, and as a result the effective region of magnetic stray field variation above each of these domains will decrease. On the other hand, domains parallel to

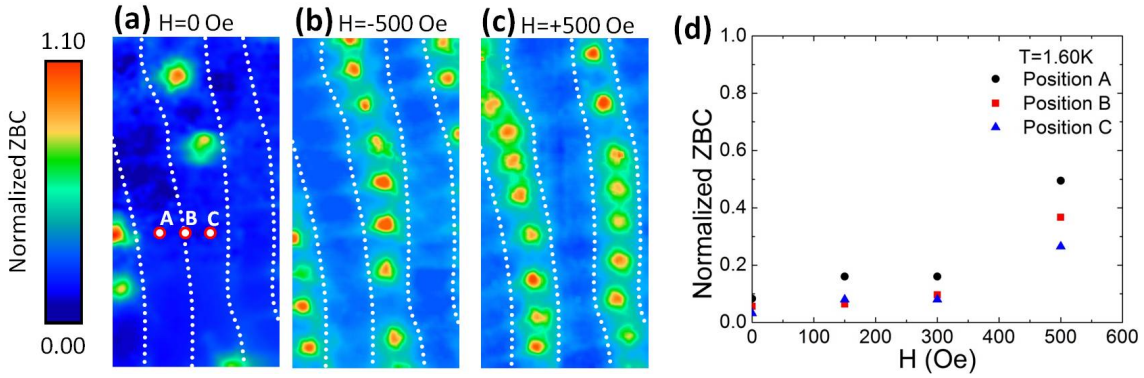

FIGURE 5.2: (a-c) 1.13 μm$\times$0.57 μm zero bias conductance maps taken in the same location as a function of applied fields showing the evolution of the vortex configuration, which reveals the nature of the underlying magnetic template. Points A, B, and C are points above the positive domain, the domain wall, and the negative domain, respectively. The white dotted lines indicate the approximate locations of the domain walls. (d) Spatial dependence of the normalized zero bias conductance values as a function of applied magnetic fields taken in positions near points A, B, and C.

the applied field will experience an increase in the effective region of magnetic stray field variation.

Tunneling spectroscopy acquired far from vortices above opposite polarity domains, as well as at the position corresponding to the domain wall (positions A, B, C in Figure 5.2(a)), show a slightly inhomogeneous superconducting state. This inhomogeneity is represented through the zero bias conductance values extracted from dI/dV spectra acquired at different values of magnetic field, which are reported in figure 5.2(d). As expected from the field dependent maps, this inhomogeneity grows with increasing field as the vortex density increases in stripes parallel to the applied field. This inhomogenous superconducting state also persists with increasing temperature. In figures 5.3(a-c) the temperature dependence of the tunneling spectra acquired above the two opposite magnetic domains (position A and C), as well as

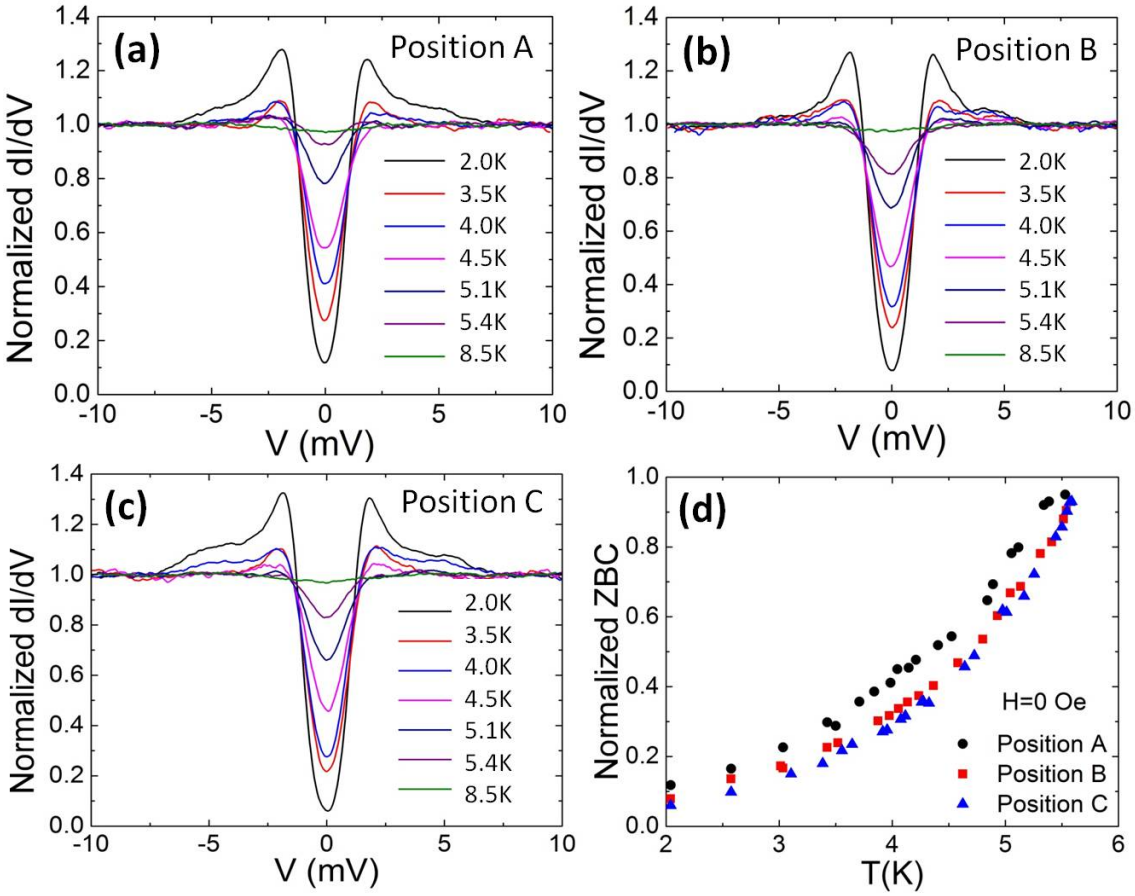

FIGURE 5.3: (a-c) Characteristic temperature dependent conductance spectra taken in zero applied magnetic field in positions A, B, and C indicated in figure 5.2(a). These spectra show that superconductivity is more pronounced (lower zero bias conductance) above the domain wall and negative domains. (d) Spatial dependence of the normalized zero bias conductance values (in positions A, B, and C) as a function of temperature. Although superconductivity decreases more quickly above the positive stripe (position A) with reduced width, the transition temperature is uniform in all regions

above the domain wall (position B), are reported. The behaviors of the temperature dependent evolution of the spectra are similar in the three locations. Again, the ZBC extracted from the dI/dV can be used to characterize the inhomogenous superconducting state. In this case, the inhomogeneity decreases with increasing temperature,

and eventually the curves all converge to the same value at the transition. Thus, the critical temperature extracted from these data is homogeneous with the location despite the different local stray field.

The effect of inhomogeneous magnetic domain size on the superconducting properties of Pb/(Co-Pd) systems has been investigated at the nanoscale, and such local variations of spectroscopic behavior in the superconducting state are less clear or inaccessible to many other techniques widely used in studies of S/F systems, such as magnetic force microscopy or transport measurements. These results show that in zero applied field only a few vortices are present due to the stray field of the ferromagnet, which are located in regions where the stripe width meets the criteria for vortex nucleation. Moreover, in applied external fields, vortices will prefer to nucleate above the domains with the same polarity as the external field. The ability to understand and control the formation of vortex-antivortex pairs in S/F structures can have far reaching impact going well beyond the fundamental understanding of vortex matter in superconductors. Many applications of superconductors in sensors are limited by noise believed to be due to dissipation from vortex-antivortex dynamics, yet no conclusive evidence of the mechanism causing this dissipation has been obtained thus far. These results show that it is possible to engineer these systems to avoid formation of vortex-antivortex pairs and that it is possible to locate vortices at different locations by changing the polarity of the applied magnetic field.

CHAPTER 6

DOMAIN WALL AND REVERSE DOMAIN SUPERCONDUCTIVITY

This chapter is comprised of an article, M. Iavarone, S. A. Moore *et al.* "Visualizing domain wall and reverse domain superconductivity," Nat. Comm. 5, 4766 (2014). The final version is available from the publisher.

Recent experimental advances in fabrication and in the measurement of mesoscopic superconductivity have renewed theoretical interest in ferromagnet-superconductor (S/F) hybrid structures. The interaction between superconductivity and magnetism, with Cooper pairs transferred from the superconductor into the ferromagnet, leads to new physical phenomena due to the proximity effect, with the mutual influence of extended electron states shared by fundamentally different materials [98]. However, if a thin insulating layer separates the superconducting and the ferromagnetic layers, the proximity effect will be suppressed and the electromagnetic interaction will dominate. In this case, the inhomogeneous distribution of the magnetic field produced by the ferromagnet substantially modifies the nucleation of the superconducting order parameter leading to a significant change in the superconducting properties [104].

Previous investigations of planar S/F hybrid structures focused on transport mea-

surements [105, 106, 107, 99, 11], vortex imaging [36, 102], S/F junctions [108] or the visualization of reverse domain wall superconductivity by scanning laser microscopy with a spatial resolution of micrometers [12, 13]. In the following sections, low temperature scanning tunneling microscopy (STM) and spectroscopy measurements focused on the direct visualization of the nucleation of superconductivity on the length scale of the superconducting coherence length will be presented. Moreover, it is experimentally demonstrated that S/F structures are efficient systems to spatially manipulate mesoscopic superconductivity and guide vortices by using an external magnetic field. Prior experimental work in the field of manipulation of superconductivity showed that the polarization of a ferroelectric, much like a ferromagnet domain polarization, could be used to control the modulation of the superconducting condensate at the nanoscale [109]. On the other hand, manipulation of a single vortex has been achieved by using a magnetic force microscopy tip, with results giving an insight into pinning strength and pinning mechanism in high-temperature superconducting materials [110].

Ferromaget/superconductor heterostructures composed of a superconducting layer placed on the top of a ferromagnetic layer, separated by a thin insulator (I) layer, have been fabricated. A multilayer Co/Pd film was chosen to be the magnetic material with a Pb thin film as the superconductor. These magnetic multilayers exhibit relatively large stray fields (compared with the critical field of the superconductor used in this study) and have striped magnetic domain patterns with the easy axis of magnetization perpendicular to the film plane [103]. The regions of the superconducting film above the domain walls experience a lower stray field, and therefore, the superconductivity is expected to nucleate at these regions when decreasing the temperature below the superconducting critical temperature T_c, giving rise to an inhomogeneous superconducting state. Scanning tunneling microscopy and spectroscopy have been used to study two S/F heterostructures (samples A and B), with

ferromagnetic films that have different magnetic domain sizes.

Upon decreasing the temperature below T_c, superconductivity emerges above the magnetic domain walls and is confined to length scales on the order of 100 nm in samples where the domain width of the ferromagnet is large enough compared with the characteristic nucleation length (that is, coherence length of the superconductor). The domain wall superconductivity leads to nanoscale confinement of the Cooper pairs by the inhomogeneous magnetic field. The emergence of superconductivity and the evolution of the inhomogeneous superconducting state with temperature strongly depend on the size of the magnetic domains in the ferromagnet. Moreover, upon decreasing the temperature below T_c, in the presence of an applied magnetic field perpendicular to the sample surface, the nucleation of superconductivity is observed in regions above magnetic domains that are aligned antiparallel to the applied field. Reversal of the polarity of the applied field leads to a shift of the superconducting regions to oppositely polarized magnetic domains, hence the appearance of reverse domain superconductivity. Furthermore, imaging of the local density of states deep in the superconducting state reveals the presence of spontaneous vortices induced by the stray field of the ferromagnet.

The S/F heterostructures were fabricated in two different systems. The (Co-Pd) multilayers were deposited on Si substrates by direct current sputtering in the presence of an applied magnetic field in a dedicated system. The presence of the in-plane field during deposition favours a stripe-like magnetic domain pattern for the films as grown. A seed layer of 4nm of Pd was used. The thickness of Co and Pd were fixed at 2nm for a total of 200 repeats for sample A, and for a total of 50 repeats for sample B. This deposition is followed by a deposition of a 10-nm Al_2O_3 layer without exposure to air. The Al_2O_3 films were grown by radio frequency sputtering from an Al target at a rate of 0.2nms1 in a partial pressure of oxygen. The gas ratios were 30sccm Ar/10sccm O_2 (3:1). The hybrid S/F system is completed with

the deposition of a 30nm Pb thin film deposited in the UHV deposition chamber linked to the STM chamber. It is quite important that the Pb surface be kept in UHV to avoid contamination. The deposition of Pb was via e-beam evaporation at low temperature (120K) followed by a room temperature annealing. This procedure enabled us to obtain flat films suitable for STM studies.

The choice of superconducting material was dictated by the value of the upper critical field of lead ($H_{c2}(T$=1.5 K)≈1,200 Oe) that is relatively low compared with the stray fields of the Co/Pd multilayers, thus providing a wide region of the H-T phase diagram where superconductivity can be spatially modulated by the stray fields of the underlying magnetic pattern. A reference Pb film was deposited on Al_2O_3, without ferromagnet for comparison and it was characterized by STM (see figure 6.1).

6.1 Inhomogeneous superconducting state in S/F hybrids

Two S/F heterostructures (samples A and B) with different magnetic domain sizes (schematics are shown in figures 6.2(a) and (b)). Sample A consists of 200 bilayers of Co (2 nm)/Pd (2 nm) as the ferromagnet and a 30-nm film of Pb as the superconductor. A 10 nm Al_2O_3 film was used as an insulator between the superconductor and the ferromagnet to suppress the proximity effect. The ferromagnet, in this sample, has an average domain size of w≈200 nm as seen in the magnetic force microscopy (MFM) image shown in figure 6.2(c). On the other hand, sample B consists of a ferromagnetic film with 50 bilayers of Co (2 nm)/Pd (2 nm) resulting in an average domain size w≈300 nm as shown in figure 6.2(d), and a 30-nm film of Pb as superconductor. It is important to note that the magnetic domains in both samples are independent of the applied magnetic field in the range of fields considered (as shown in figure 6.3). Therefore, no magnetic domain wall motion is taking place during STM measurements in applied magnetic field for the range of fields explored.

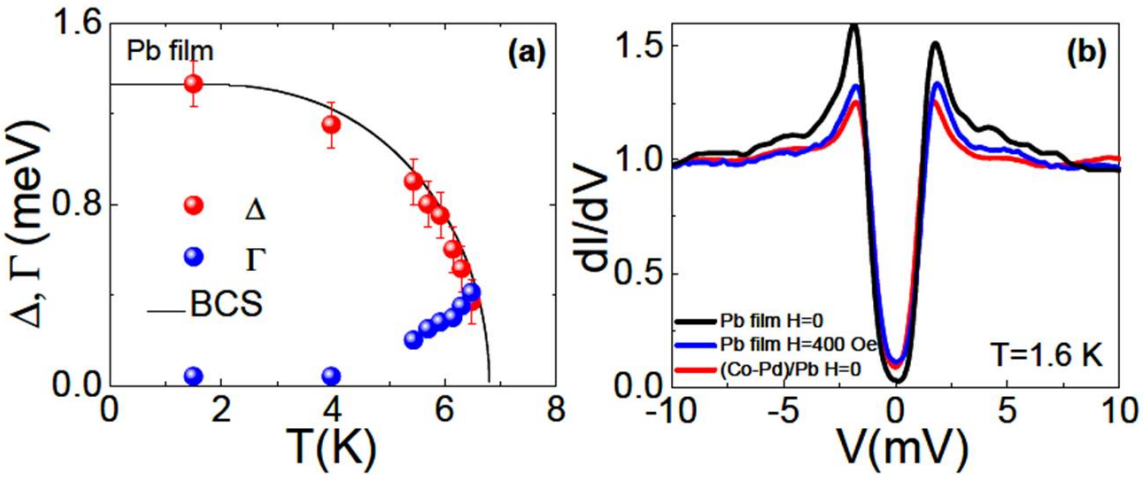

FIGURE 6.1: (a) Temperature dependence of the gap (red dots) and of the quasiparticle lifetime Γ (blue dots) for the reference 30 nm Pb film, derived by the BCS DOS fitting with the Dynes formula, as described in the main text. The error bars represent the standard deviation obtained from the fit. The continuous black line is the BCS gap equation corresponding to T_c=6.8 K. (b) Comparison between the tunneling dI/dV spectrum on the Pb reference film at T=1.6 K in zero applied magnetic field, a tunneling dI/dV spectrum acquired on the same film at the same temperature in a magnetic field H=400 Oe applied perpendicular to the film surface and a tunneling dI/dV spectrum acquired on a (Co-Pd)/Pb (Sample B) system in a zero applied external field. In all cases spectra have been acquired in locations far from vortices and with the same tunneling conditions: V=-10 mV, I=100 pA. The dI/dV curves have been normalized to the value of conductance at V=-10 mV.

The spatial distribution of the surface magnetic field induced by the ferromagnet in the S/F hybrid system depends upon the ratio of two length scales: the thickness of the ferromagnet D, and the domain width w [111]. In the case of both sample A ($D > w$) and sample B ($D \approx w$), there is a gradient of stray field above each domain with the field reaching the maximum value at the centre of the domain (see figure 6.4). The distribution of stray fields for a stripe domain structure in a ferromagnetic film can be calculated analytically. If the film is parallel to the xy plane the z component of the stray field in the direction perpendicular to the film

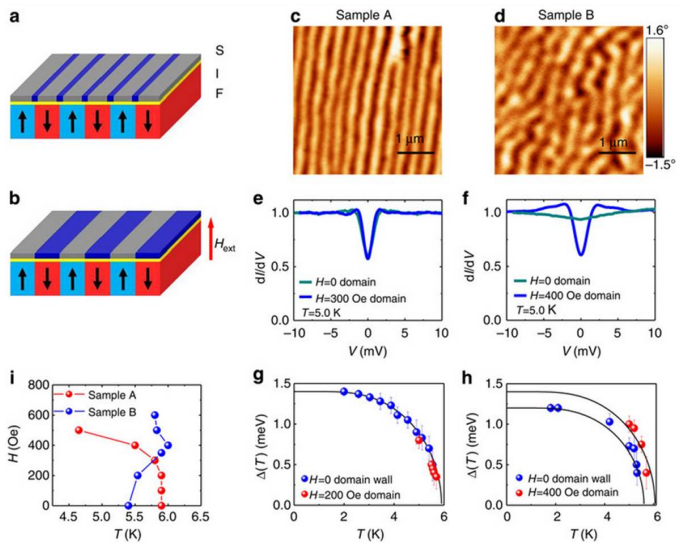

FIGURE 6.2: (a,b) Schematics of a hybrid system, consisting of a ferromagnet (F), insulator (I) and a superconducting film (S), close to the superconducting critical temperature. (a) In zero applied magnetic field, the superconductivity nucleates in the regions above the domain walls (shown in blue). (b) In the presence of an applied magnetic field that compensates one type of domain, the superconductivity nucleates above the antiparallel domains (blue regions). (c,d) Magnetic force microscopy phase images (scan area of 4×4 μm^2, scale bar, 1m) at room temperature of two ferromagnetic samples used in this experiment. MFM measurements have been performed after deposition of the Al_2O_3 layer. (c) Sample A (200 bilayers of Co (2nm)/Pd (2nm)) showing a stripe domain pattern with average domain size w≈200 nm. (d) Sample B (50 bilayers of Co (2nm)/Pd (2nm)) showing a stripe domain pattern with average domain size w≈300 nm. (e,f) STM conductance spectra acquired on (e) (Co-Pd)/Pb sample A and (f) (Co-Pd)/Pb sample B, at a position corresponding to the middle of a magnetic domain. The two spectra were acquired in the absence and in the presence of an external field H at T=5.0 K. The tunneling spectra have been normalized to the conductance value at V=-10 mV. (g,h) Temperature dependence of the gap values obtained from the conductance spectra acquired on the (g) (Co-Pd)/Pb sample A and (h) (Co-Pd)/Pb sample B. The blue dots represent the temperature dependent gap values at the location above a magnetic domain wall in the absence of an external field. The red dots represent the temperature dependent gap values at a location corresponding to the middle of the magnetic domain in the presence of a compensating applied magnetic field. The gap values have been derived by the Bardeen-Cooper-Schrieffer (BCS) DOS fitting. The error bars represent the standard deviation obtained from the fit. The experimental points are compared with the BCS gap equation $\Delta(T)$ (solid lines). (i) Phase diagram of the highest local T_c versus H derived from local tunneling spectroscopy measurements for both samples.

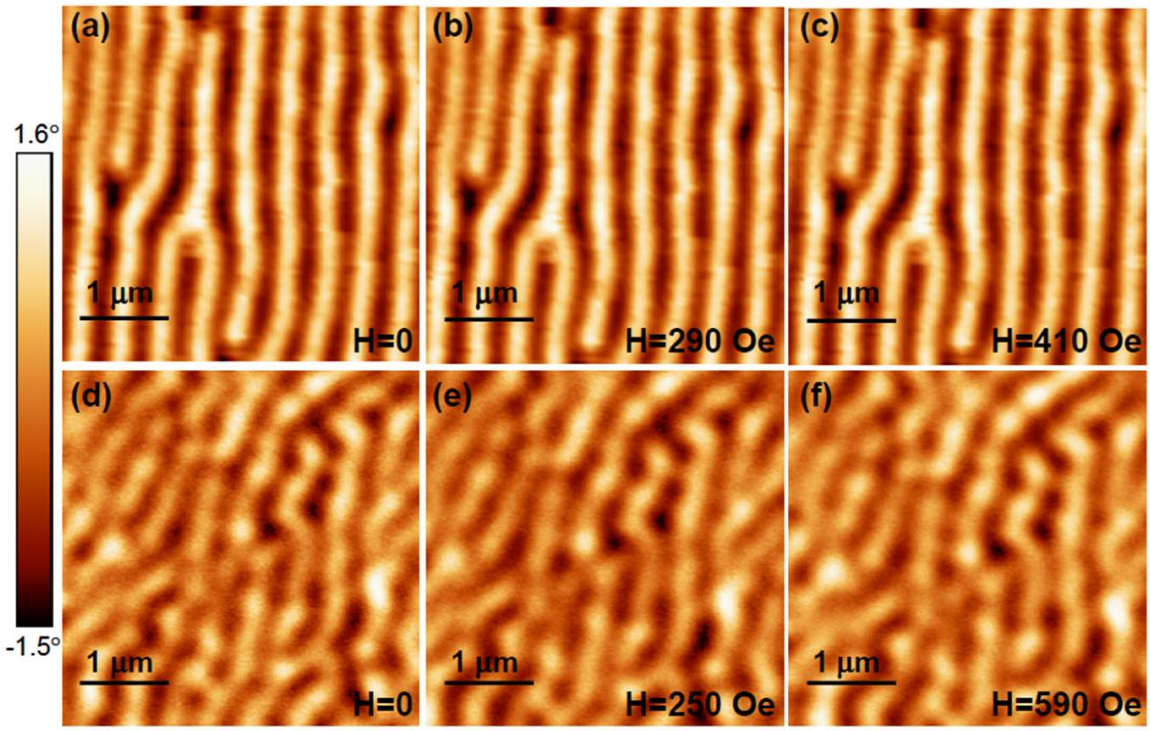

FIGURE 6.3: Room temperature 4×4 μm^2 MFM phase images, acquired in lift mode, of the (a), (b), (c) 200 bilayers of Co(2nm)/Pd(2nm) (SampleA) and (d), (e) , (f) 50 bilayers of Co(2 nm)/Pd(2nm) (Sample B) in external magnetic fields applied perpendicular to the surface. (a) H=0 Oe, (b) H=290 Oe, (c) H=410 Oe, (d) H=0 Oe, (e) H=250 Oe, (f) H=590 Oe. Scale bars are 1 μm. MFM images have been acquired after deposition of the Al_2O_3 layer.

surface is

$$b_z(x,z) = Im\left[4M_0\left[\ln\tan\frac{\pi t}{2w} - \ln\tan\frac{\pi(t-iD)}{2w}\right]\right] \tag{6.1}$$

where t=x+iz, D is the ferromagnet thickness, and w is the stripe domain width [111]. If the thickness of the superconductor is less than the superconducting penetration depth (in the case of bulk Pb λ=38 nm [112]), the magnetic field distribution will not be affected by the superconducting transition, as in these two S/F systems [111]. When the temperature is decreased below T_c, the superconductivity is expected to

first nucleate at the location where the stray field is minimum, that is, at the domain wall, which is a realization of domain wall superconductivity [104] (figure 6.2(a)). The theoretical condition for the nucleation of the superconductivity at a domain wall is that the characteristic length scale for the nucleation of superconductivity, that is, the coherence length at the superconducting critical temperature of the S/F system $\xi(T_c)$, should be smaller than the domain half-width to avoid overlap of the superconducting nuclei [11]. The local T_c value above the domains will be lower than the T_c above the domain wall. On the other hand, when an external magnetic field is applied perpendicular to the film, the regions with minimum magnetic field will shift to a different position due to magnetic field compensation effect (figure 6.2(b)). Therefore the applied magnetic field will spatially shift the superconducting nucleus to the centre of the compensated domain, as shown schematically in figure 6.2(b).

Systems with purely electromagnetic interactions can be described phenomenologically using the Ginzburg-Landau and London formalisms. Aladyshkin *et al.* [41, 113] solved the linearized Ginzburg-Landau equations for a superconducting film and a ferromagnetic film with a periodic one-dimensional domain structure with magnetization perpendicular to the film surface. The spatial inhomogeneity of the stray field leads to different regimes of the order parameter nucleation and an unusual phase boundary $T_c(H)$ depending upon parameters, such as the stray field values, characteristic length scale for nucleation of the superconductivity and magnetic domain size.

Local differential tunneling conductance data (dI/dV), obtained from the scanning tunneling spectroscopy measurements, provide information about the local density of states (LDOS) in the material. Mapping of the LDOS is an effective method of visualizing a temperature and magnetic field evolution of the inhomogeneous superconducting state on the nanometer scale. In sample B, containing wider magnetic domains, the superconducting inhomogeneities are more strongly pronounced at H=0

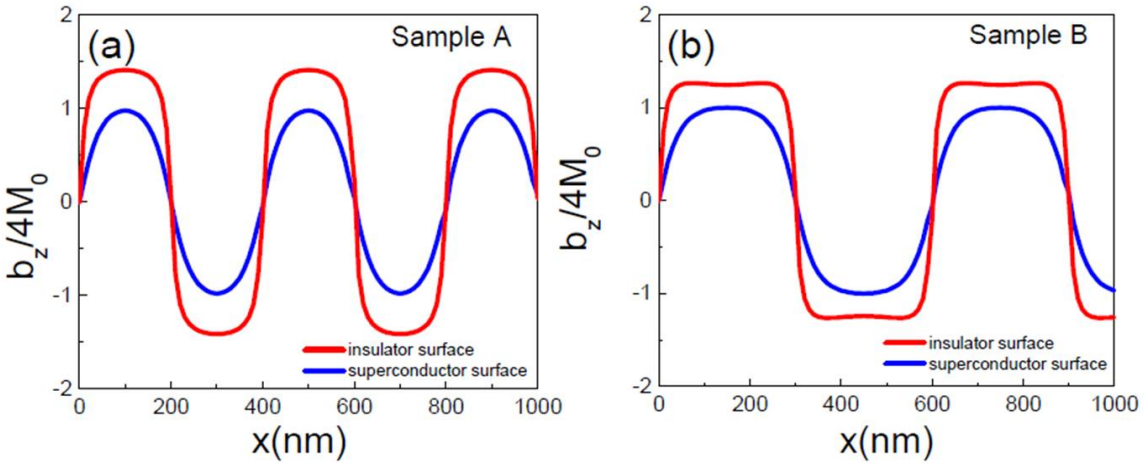

FIGURE 6.4: Calculated magnetic field distribution for the Ferromagnet-Insulator-Superconductor systems for (a) Sample A (ferromagnet thickness D=800 nm, magnetic domain width w=200 nm) and for (b) Sample B (ferromagnet thickness D=200 nm, magnetic domain width w=300 nm). In both graphs the red line represents the stray field at the top of the insulators surface (at a distance z=10 nm from the ferromagnets surface) and the blue line is the magnetic profile at the surface of the superconductor (at a distance z=40 nm from the surface of the ferromagnet). This calculation is based on the formula given by equation 6.1.

Oe, the tunneling spectra are spatially homogeneous and do not depend on the distance from the magnetic domain wall (figure 6.5). Moreover, spectra acquired at positions corresponding to the middle of a magnetic domain do not change in external fields up to H=300 Oe (figure 6.2(e)). On the other hand in sample B, under the same conditions, a superconducting gap like spectra with a pronounced dip in the LDOS at the Fermi energy E_F (zero bias conductance, ZBC) and symmetric coherence peaks at positive and negative energies from the Fermi energy is observed. In the other locations, the spectra look similar to the ones observed in the normal state (figure 6.6). Application of a field of H=+400 Oe leads to even more inhomogeneous superconducting state, with the strongest superconductivity now observed at the locations that were normal at H=0 Oe (figure 6.2(f)). These locations correspond to

the centers of magnetic domains that are antiparallel to the applied field. The local stray field is reduced here as a consequence of the compensation by the applied field. Such a strong spatial variation of superconductivity in sample B is in stark contrast to the state of sample A, in which no spatial variation of the local T_c is observed up to applied fields of H=200 Oe (figure 6.2(g)). In sample B there is a strong magnetic field enhancement of the superconductivity at the centers of domains that are antiparallel to the applied field, with local T_c values that exceed any observed at H=0 Oe (figure 6.2(h-i)). In figure 6.2(h) the superconducting gap values (obtained from the tunneling spectra) in sample B at H=0 Oe in locations above the magnetic domain wall and at H=+400 Oe in locations above the center of an antiparallel domain are compared. The data show that the T_c value is location dependent. A comparison of the superconducting phase diagrams $T_c(H)$ for both samples is summarized in figure 6.2(i). The phase diagram is obtained from the tunneling spectra acquired as a function of applied field and temperature with each point corresponding to the highest local T_c value obtained at each field. The magnetic field enhancement of the superconductivity in sample B is shown by a pronounced re-entrant behavior of the H-T phase line.

6.2 Visualization of reverse domain superconductivity

A map of the ZBC, that is, the LDOS at the Fermi level, reveals normal and superconducting regions with atomic resolution. Therefore, it is a direct experimental technique to visualize the emergence of domain wall superconductivity and reverse domain superconductivity with high spatial resolution. Although STM is not sensitive to the magnetic field, the presence of a superconducting film can be used as an indicator of the underlying magnetic pattern. Local changes in tunneling spectra performed in applied magnetic fields of opposite polarity will indeed reveal the location and polarity of the underlying magnetic domains. In figure 6.7 the magnetic field

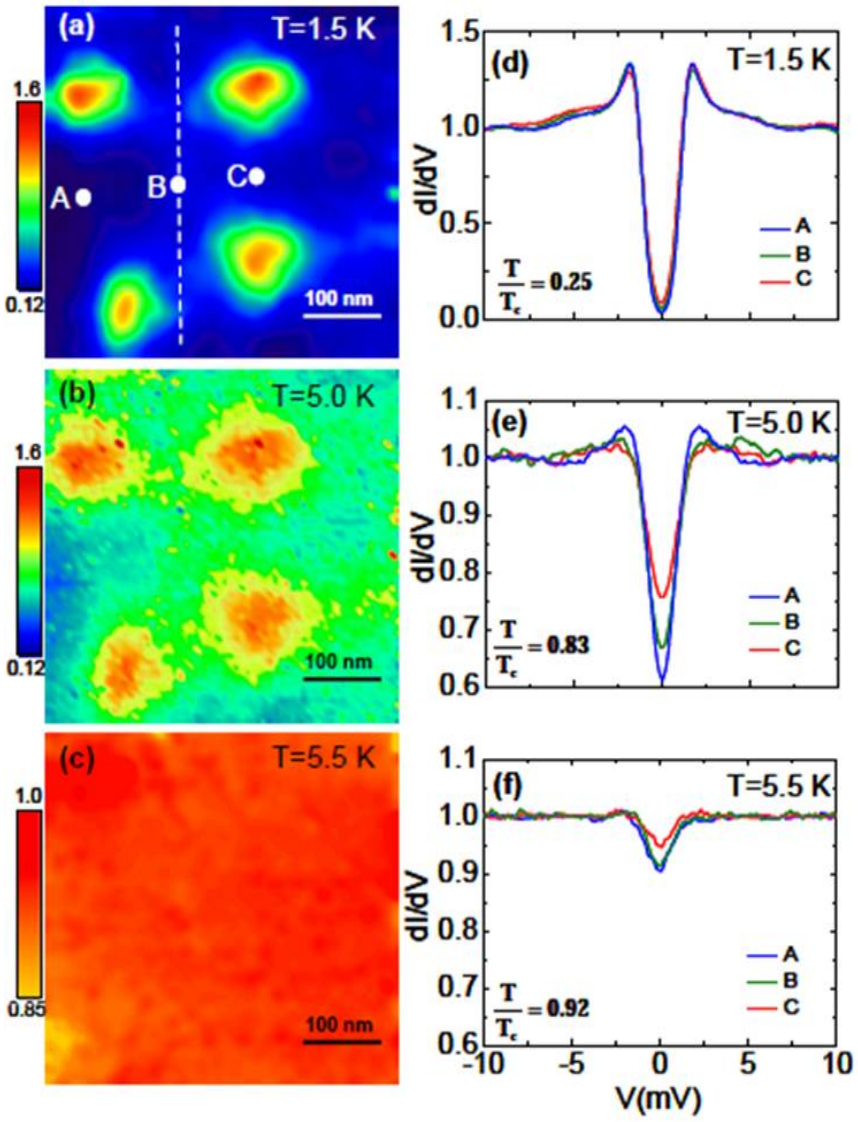

FIGURE 6.5: (a), (b), (c) LDOS maps at the Fermi energy acquired at H=0 Oe and at (a) T=1.5 K, (b) T=5.0 K, (c) T=5.5 K. All maps have been normalized to the maps acquired simultaneously at V=-10 mV. The scan areas in (a), (b) and (c) are 450×450 nm^2 and the scale bars are 100 nm. The white dashed line in (a) indicates the approximate positions of the domain walls as inferred from the vortex configurations at different fields (figure 6.7).The graphs in (d), (e) and (f) show the tunneling spectra acquired at different location across the domain wall (Positions A, B, C) of the corresponding LDOS map taken at the same temperature. All spectra have been acquired with the same tunneling conditions V=- 10 mV and I=100 pA and normalized at V=-10 mV.

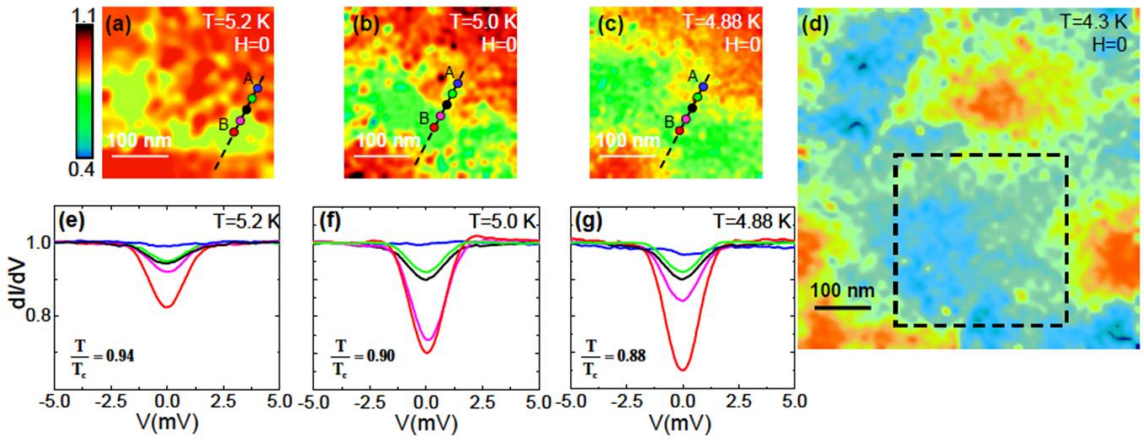

FIGURE 6.6: (a), (b), (c), (d) LDOS maps at the Fermi energy acquired at H=0 Oe and at (a) T=5.2 K, (b) T=5.0 K, (c) T=4.88 K and (d) T=4.3 K. All maps have been normalized to the maps acquired simultaneously at V=-10 mV. The colour scale (representing the normalized zero bias conductance) is the same for all images. The scan areas are 300×300 nm^2 for (a), (b), (c) and 600×600 nm^2 for (d). The maps in (a), (b) and (c) have been acquired at the location indicated with a dashed square in (d). The graphs in (e), (f) and (g) show the tunneling spectra acquired at different location across the domain wall (along the dashed line from A to B every 15 nm) of the corresponding LDOS map at the same temperature. The colors used for the tunneling spectra are the same used to indicate the locations where the spectra were acquired (coloured dots on the corresponding LDOS map). All spectra have been acquired with the same tunneling conditions V=-10 mV and I=100 pA and they have been normalized to the value of conductance at V=-5 mV.

dependence of the ZBC maps acquired from sample A is presented. Figure 6.7(a) is the topography image of the top Pb film, which shows atomically flat terraces. Figures 6.7(b-h) are LDOS maps at E=E_F acquired on the same area as a function of H and T. The ZBC conductance map at T=1.5K in zero externally applied field (figure 6.7(b)) reveals the presence of vortices spontaneously induced by the stray field of the ferromagnet, in agreement with theoretical predictions [33, 9]. Vortices appear as normal regions in the conductance map, which are regions with higher ZBC. Therefore, the polarity of the vortex is indistinguishable in the STM image. By applying

a magnetic field of H=+200 Oe and +300 Oe (figures 6.7(c) and (e)), the vortex density increases in some regions and decreases in other regions. In opposite fields of H=-200 Oe and -300 Oe (figures 6.7(d) and (f)), the regions where the vortex density increases and decreases are interchanged, with the vortices always following a stripe-like pattern. These images suggest that the regions with increasing vortex density in positive applied fields are above a positive magnetic domain. Instead, regions with decreasing vortex density in positive applied fields, due to compensation effects, are above a negative magnetic domain. It can be concluded that the observed vortices have opposite polarities and they are located above the corresponding domain with the same polarity [36, 100]. The formation of vortex chains is due to confinement by the stray magnetic field from the underlying magnetic domains [102].

Close to T_c in the presence of an applied magnetic field, superconducting regions will be located above the magnetic domains antiparallel to the external field, whereas normal regions will be located above the magnetic domains with the same polarity as the external field. In figures 6.7(g) and (h) the conductance maps at H=+300 Oe and H=-300 Oe, respectively, show the direct visualization of the reverse domain superconductivity. Here, the effect of reversing the applied field produces two complementary images with normal and superconducting regions that exchange their position upon reversal of the applied field.

6.3 Visualization of domain wall superconductivity

In sample B the magnetic domains are wider and the magnetic pattern is more irregular. The vortices in zero applied field form an irregular stripe pattern following the irregular magnetic pattern, as shown in figure 6.8(a). The location and the polarity of the underlying magnetic domains have been checked by local tunneling spectroscopy performed at different applied fields of both polarities.

Now attention is placed on the nucleation of the superconductivity close to T_c

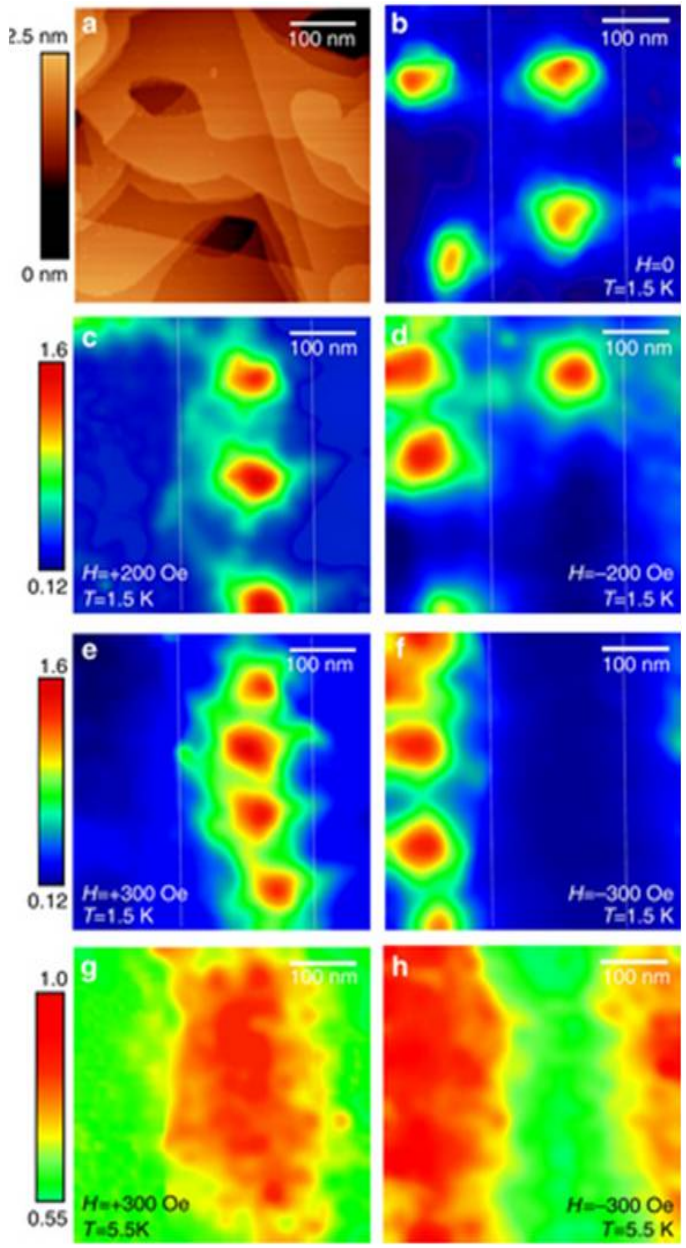

FIGURE 6.7: (a) STM topography image of the Pb film in sample A. Scan area is 450×450 nm^2. The tunneling conditions are: V=-20 mV and I=100 pA. (b-h) Zero bias conductance maps acquired on the same area at different applied fields and temperatures. The white dashed lines indicate the approximate positions of the domain walls as inferred from the vortex configurations at different fields. The conductance maps are normalized to the conductance maps at V=-10 mV. (b) H=0 Oe, T=1.5 K; (c) H=+200 Oe, T=1.5 K; (d) H=-200 Oe, T=1.5 K; (e) H=+300 Oe, T=1.5 K; (f) H=-300 Oe, T=1.5 K; (g) H=+300 Oe, T=5.5 K; (h) H=-300 Oe, T=5.5 K. Scale bar, 100 nm for all images.

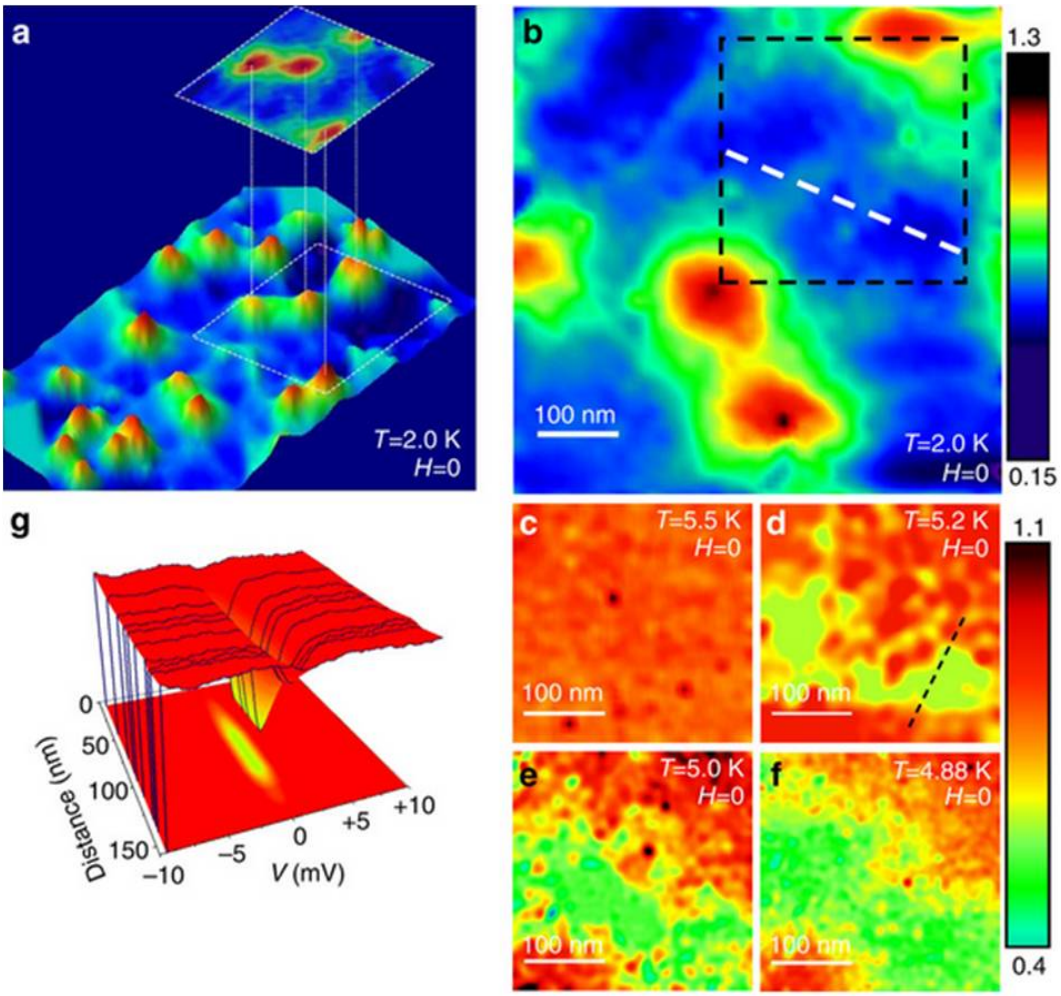

FIGURE 6.8: (a) Zero bias conductance map acquired at T=2.0 K in zero applied field for sample B. The image shows spontaneous vortices produced by the underlying magnetic pattern. Scan area is 900×1,625 nm^2. The image was obtained by acquiring several images of size 600×600 nm^2. The inset shows the same image reported in b. The image is rotated and superimposed to a to show the field of view of b on a larger map. The vertical dashed lines indicate the position of the individual vortices. The white dashed square is the scan area in (b). (b) Zero bias conductance map at T=2.0 K and applied field H=0 Oe in a smaller field of view. The scanning area is 600×600nm^2, scale bar, 100nm. The dashed square in the image shows the field of view (300×300nm^2) for the zero bias conductance images shown in (c) T=5.5 K, (d) T=5.2 K, (e) T=5.0 K and (f) T=4.88 K (scale bar, 100nm for c-f). The magnetic field is H=0 Oe for all images. The white dashed line shows the approximate position of the domain wall. (g) Series of local tunneling dI/dV spectra acquired across the dashed line in (d) at T=5.2 K (tunneling conditions V=-10 mV and I=100 pA). The conductance maps are normalized to the conductance maps at V=-10 mV.

in zero applied external field. The order parameter should nucleate first at the location with minimum local stray field. However, if the magnetic domain size is too small, the order parameter cannot follow the rapid variation of the local field. In this case overlapping of the superconducting nuclei is to be expected, which produces a practically uniform superconducting state. Different behavior for samples A and B is observed. In sample A, with stripe width w≈200 nm, a uniform nucleation of superconductivity when T is lowered below T_c is detected (as shown in figure 6.5). In sample B, with larger magnetic domains of w≈300 nm, the order parameter distribution is strongly modulated by the presence of the inhomogeneous field (figure 6.8 and figure 6.6). Figure 6.8(b) shows a rescanned ZBC image in a smaller area acquired at T=2.0K on sample B showing spontaneous vortices. The dashed square, 300nm×300nm, represents the field of view used to directly visualize the nucleation of superconductivity. The ZBC map at T=5.5K (figure 6.8(c)) shows the same conductance value everywhere, with local tunneling spectra corresponding to the normal state. By decreasing T to 5.2K, the ZBC map (figure 6.8(d)) shows areas of lower conductance localized along the white dashed line in figure 6.8(b). This area corresponds to a region above the domain wall in the ferromagnet. The lateral size of the superconducting nucleus is ∼120nm. The value of the ZBC above the domain wall is only 15% lower than the conductance above the domains, due to T being very close to T_c. The spatial evolution of the tunneling spectra shows that the most superconducting region (lower ZBC) extends for 50 nm, with the ZBC gradually increasing on each side for about 35 nm. As T is further decreased to T=5.0 K (figure 6.8(e)) and T=4.88 K (figure 6.8(f)), the superconducting state becomes more robust, characterized by tunneling spectra with a lower conductance at E_F, and therefore, by more depletion of states at E_F. A sequence of tunneling spectra recorded along the dashed line in figure 6.8(d) appears in figure 6.8(g).

To explain the different behavior of the nucleation of superconductivity in the two

samples the characteristic length scale of nucleation of the superconductivity needs to be estimated. The criterion for domain wall superconductivity is $w > 2\xi(T_c)$. The coherence length can be estimated from the upper critical field measured on a reference Pb film fabricated without ferromagnet. The measured value of H_{c2}(1.5 K)≈1,100 Oe gives $\xi(T$=1.5K)≈54 nm, which means that ξ_0=48nm. The value of 2ξ(T=1.5 K) is consistent with the average diameter of vortices in these images [114]. Furthermore, this value of coherence length, very different from the bulk value of 87nm [112], is in agreement with values of 40÷50nm reported for ultrathin Pb films [71]. Using $\xi(T_c) = \xi_0/\sqrt{1 - T_c/T_{c0}}$, where ξ_0=48nm is the zero temperature coherence length, T_{c0} is the critical temperature of the reference Pb film without ferromagnet, and T_c is the superconducting temperature of the S/F bilayer, gives for sample A ξ(6K)≈140nm and for sample B ξ(5.5K)≈110nm. Therefore, $w > 2\xi(T_c)$ in the case of sample B and $w < 2\xi(T_c)$ in the case of sample A, which confirms that the two samples are in different regimes. Sample A is in the regime of overlapping superconducting nuclei above different domains; whereas in sample B the superconducting wave function is localized above regions with minimum stray field.

Finally, attention is turned to the tunneling spectra acquired at the domain wall at 5.2K (figure 6.8(c)) and figure 6.6(e)). The tunneling spectra in the superconducting regions are much more smeared than the tunneling spectra in the Pb reference film (deposited on an Al_2O_3 substrate; figure 6.1). The increased broadening cannot be accounted for even considering the difference in T_c values. Lead is a strong-coupled superconductor. Therefore, the density of states should be obtained directly from the Eliashberg's mean-field formalism, which accounts for recombination processes and electron-phonon scattering. However, a simpler approach was proposed by Dynes *et al.* [84]

$$N_S(E, T, \Gamma) = Re\left[\frac{|E| + i\,\Gamma(T)}{\sqrt{(E + i\,\Gamma(T))^2 - \Delta(T)^2}}\right] \tag{6.2}$$

with $N_s(E, \Delta, \Gamma)$ being the density of states of the superconductor, Δ is the superconducting gap, and Γ is the quasiparticle lifetime that takes into account all sources of scattering, including the orbital depairing produced by the stray field [94]. The experimental dI/dV spectra were fitted with the equation:

$$G(V) = G_{nn} \frac{d}{dV} \int_{-\infty}^{+\infty} N_S(E, T, \Gamma) \left[f(E) - f(E - eV) \right] dE \tag{6.3}$$

where $f(E)$ is the Fermi-Dirac distribution function and G_{nn} is the conductance of the tunnel junction for high bias (normal state). This approach is widely used, since the values of Δ and Γ are in excellent agreement with theoretical predictions based on the Eliashberg formalism. In the case of Pb, Dynes' density of states does not reproduce the experimental tunneling conductance spectra acquired at low temperatures, due to the gap anisotropy [86]. Nevertheless, at higher temperatures, because of the thermal broadening, the anisotropy is usually smeared, and this approach provides reasonable fittings of the experimental data. For the spectra acquired above the domain wall region on sample B, at T=5.2K (figure 6.8(c) and figure 6.6(e)), the fitting yields values of Δ=0.7meV and Γ=0.7meV. For T in the range 5.2-5.35K, the spectra do not show the presence of coherence peaks, but still present a dip around E_F. These spectra cannot be fitted accurately with the above model; the fit yields a very high value of Γ, compared with the fits on the Pb reference film at the same reduced temperature. In the regime of domain wall superconductivity, the superconductivity is filamentary and the sample consists of superconductor-normal interfaces. Cooper pairs are squeezed into a very small volume, thus the quantum confinement in the transverse dimension becomes important and strongly modifies the wavefunctions. Thermal and quantum fluctuations [115] will have a dominant role, and, therefore, suppress the superconductivity due to phase slips [116]. The lateral confinement also promotes an increase in the Coulomb repulsion. A description of the spatial

evolution of tunneling spectra in mesoscopic proximity systems in the presence of a non-homogeneous magnetic field is beyond any existing theory. New theoretical work would also have to take into account nonlocal effects in the normal regions due to electronic interference [117]. These results provide direct evidence of the possibility of order parameter manipulation in S/F hybrid systems and should stimulate theoretical work to take into account nonlocal effects in mesoscopic proximity systems.

CHAPTER 7

S/F HYBRIDS WITH OFF-AXIS SUPERCONDUCTING FILM

A continuous need for ever increasing performance and decreasing size in modern electronic devices continues to fuel and reshape both experimental and theoretical condensed matter research. Along this path, heterostructures of two or more different systems have become one of the most promising avenues towards the discovery and functionalization of new materials and their properties. In particular, heterostructures comprised of superconductors and ferromagnets reveal exciting properties despite the antagonistic nature of the constituent materials. When directly in contact the electronic properties of superconductor/ferromagnet (S/F) systems will be strongly dominated by proximity effects, which can lead to a number of exciting physical phenomena such as so-called long range triplet superconductivity [118, 119]. This type of phenomenon can be highly applicable in the growing field of spintronics [120]. On the other hand, if the two materials are electrically isolated, the resulting system's properties are governed only by the magnetic interactions [11]. In particular, the properties of the superconductor can be strongly altered due to the orbital interaction with the ferromagnet stray field. This can lead to a variety of in-

teresting phenomena such as the ability to control vortex behavior and the presence of filamentary nuclei of superconductivity, which have been verified by a number of experimental works [101, 14, 121].

The majority of experiments on planar magnetically coupled S/F heterostructures have so far been primarily focused on global measurements [107, 113, 105, 99, 106] and the theoretical community has not had too much difficulty in predicting and/or explaining the results [9, 33]. However the increased use of local probes, such as the scanning tunneling microscope [122, 102] and magnetic force microscope [36], have begun to reveal a rich body of new physics that might bring more questions that need to be theoretically addressed. Nanoscale superconducting properties of an S/F system are reported where the (111) direction of an ultrathin Pb film is tilted at approximately 50° with respect to the plane of the underlying multilayer Co-Pd ferromagnet. In this case the parallel component of the magnetic stray field, which has a local maximum above the domain wall, plays a significant role in the underlying physics. Previous work by Tinkam and co-workers have shown both theoretically [123] and experiementally [124] that there is a strong relationship between the superconducting thermodynamic critical field and the angle of the applied magnetic field, which is given by

$$H_c \sin\theta / H_{c\perp} + (H_c \cos\theta / H_{c\parallel})^2 = 1 \tag{7.1}$$

in the case of a clean superconducting film subjected to a uniform magnetic field. Measurements have shown that when the magnetic field does not fall along the c-axis the local electronic properties which are only accessible by STM can be unique, such as the case of vortices in $NbSe_2$ using inclined and in-plane magnetic fields [125, 126, 127]. Our results on an S/F system, where there exists a *non-uniform* magnetic stray field, reveal a modulation of the superconducting properties at the nanoscale that are unreconcilable within conventional S/F theory which neglects the effect of

the in-plane component of the magnetic stray field. In the theoretical treatments of S/F systems found in literature so far the starting point is to consider the linearized Ginzburg-Landau equation for the order parameter Ψ [42, 43, 17]:

$$-\left(\nabla + \frac{2\pi i}{\Phi_0}\mathbf{A}\right)^2 \Psi = \frac{1}{\xi^2(T)}\Psi \tag{7.2}$$

where $\mathbf{A}(\mathbf{r})$ is the vector potential, Φ_0 is the flux quantum, and $\xi(T)$ is the coherence length. Customarily the next step is to neglect the parallel magnetic stray field on the premise that for ultrathin superconducting films ($\xi > d$) its role should be negligibly small. While experimental evidence for c-axis oriented films largely agrees with most of the theoretical predictions handled in this way, this is not the case for off-axis films. When the film axis is tilted more and more with respect to the plane of the ferromagnet a growing proportion of the parallel magnetic stray field penetrates the film along the c-axis, resulting in a behavior that is very reminiscent of Tinkham's work on the angular dependence in uniform films. At a certain tilt angle of the superconducting film, when the combined ferromagnet stray fields from both the parallel and perpendicular components are maximized, there will be a signficant suppression of superconductivity localized in some region. These spatially modulated superconducting properties have been investigated by means of temperature and magnetic field dependent spectroscopy and conductance maps.

The multilayer ferromagnet Co-Pd film was grown by successive dc magnetron sputtering of 2nm Co and 2nm Pd for a total of 200 bilayers onto a Si(100) substrate in a vacuum system with a base pressure of $2\text{x}10^{-8}$ Torr. A small magnetic field of a few hundred Oersted was applied in-plane during the multilayer deposition because this has been shown to promote a more uniform stripe domain structure [103]. To prohibit proximity effects between the ferromagnet and superconducting layers a thin 10nm film of Al_2O_3 was consequently deposited on top of the Co-Pd multilayer film

by rf magnetron sputtering of aluminum in a partial pressure of oxygen (30sccm Ar/10sccm O_2). The resulting [2nm Co-2nm Pd]$_{N=200}$ has been characterized by squid magnetization measurements and room temperature magnetic force microscopy (MFM), as shown in figure 7.1. The MFM measurements were performed prior to the deposition of the Pb film and after the STM measurements to confirm that the magnetic pattern remains unchanged after application of magnetic field up to at least 500 Oe. Ultrathin 30nm Pb films were deposited at low temperature onto the Co-Pd/Al_2O_3 using e-beam evaporation at a rate of approximately 0.2nm/min and allowed to gradually warm to room temperature; the deposition temperature and rate of annealing strongly influence the final morphology of the film. To avoid contamination of the Pb surface the deposition was performed *in situ* in an ultrahigh vacuum deposition chamber directly connected to the STM with a base pressure better than 4x10^{-11} Torr.

The low-temperature STM measurements were performed using an ultra-high vacuum Unisoku ^{3}He system capable of reaching temperatures as low as 320mK in the presence of magnetic fields perpendicular to the sample plane of up to 9T. Differential conductance spectra (dI/dV), which for small bias voltages represents the local density of states, have been acquired using the standard lock-in ac modulation technique with a frequency of 373Hz and a modulation amplitude of 0.2mV. The zero bias conductance maps were acquired simultaneously with topography by periodically stopping scanning, disabling the feedback, and acquiring the conductance value at zero bias using the lock-in technique. Normal Pt-Ir tips have been used for all measurements.

In figures 7.2(a) and (b) large scale topographic STM images are shown which reflect the difference in morphology of the c-axis and off-axis oriented Pb films. As seen from the topographies the c-axis film has large flat terraces with the (111) crystallographic direction oriented normal to the plane of the film, whereas in the case

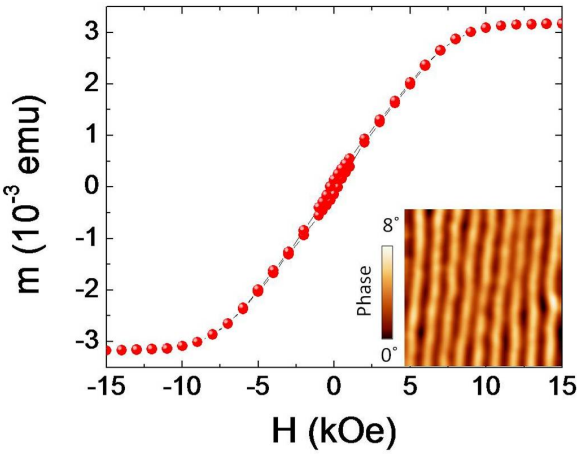

FIGURE 7.1: Perpendicular magnetization loop of a typical Co-Pd multilayer film acquired using squid magnetometry. The hysteresis loop shows coercive and saturation fields typical of ferromagnet multilayers with stripe domains. Inset shows 4x4μm^2 room temperature magnetic force microscopy image of the Co-Pd showing very uniform stripe domains.

of the off-axis film the (111) direction is instead tilted at approximately 50°. To provide a better understanding of the underlying ferromagnet layer the magnetic domain structure has been simulated using characteristic values from the magnetization loops and by solving the Landau-Lifshitz-Gilbert equations in the commercially available LLG Software package; using for the geometry a 0.2x2.0μm^2 cross section and a 5x5nm^2 cell size. The simulated domain structure shown in figures 7.2(c) and (d) has domain widths of approximately 200nm, and is in great agreement with previous measurements of the same multilayer system [10]. To emphasize the difference between c-axis and off-axis films cartoon depictions of the overlayers have been added to show the relative orientation of the magnetic features with respect to the film axes. The Co-Pd multilayer film breaks up into alternating up (red) and down (blue) perpendicular magnetic domains, between which the magnetization vector continuously rotates resulting in additional alternating in-plane magnetic domains. Simulations have also been performed of the perpendicular and parallel stray fields at

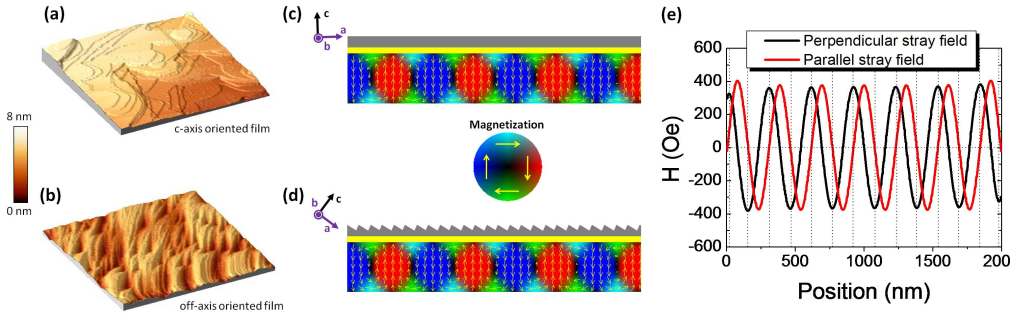

FIGURE 7.2: (a,b) Topographic images (438x438nm^2) representing the typical morphologies of Pb films grown with the (111) direction oriented perpendicular (c-axis) and at a slight angle (off-axis) to the surface of the ferromagnet, respectively. Tunnel conditions were -10mV and 100pA for both images. (c,d) Simulation of the internal magnetization vectors of the multilayer ferromagnet film found by solving the Landa-Lifshitz-Gilbert equations using values extracted from hysteresis loops ($H_{sat}^{\parallel}$=1860Oe and $H_{sat}^{\perp}$=7900Oe). The color wheel indicates the orientation of the net magnetization. Cartoons of the film morphology in the cases of (c) c-axis and (d) off-axis have been added to show the relative orientation of the film with respect to the magnetic features. (e) Simulated magnitude of the perpendicular and parallel componenets of the magnetic stray field at a distance of 60nm from the surface of the ferromagnet. The perpendicular stray field is a maximum above the center of the domain, and the parallel stray field is a maximum above the domain walls.

a distance of 60nm above the ferromagnet film surface, which are plotted as a function of position in figure 7.2(e). Both the perpendicular and parallel stray fields take a sinusoidal form, with the maximum stray fields in the perpendicular and parallel directions centered above the domains and domain walls, respectively. Because the exact nature of the magnetic stray field will vary with the internal domain structure not all ferromagnet systems may exhibit such a large parallel component. Moreover, it should also be emphasized that the values for the perpendicular stray field found from this simulation agree well with the estimated values from STM measurements on similar systems [14].

Figures 7.3(a) and (b) show concurrently acquired topographic and zero bias conductance (ZBC) images of the off-axis superconducting Pb film. The low-temperature ZBC map acquired in the absence of any externally applied magnetic field reveals

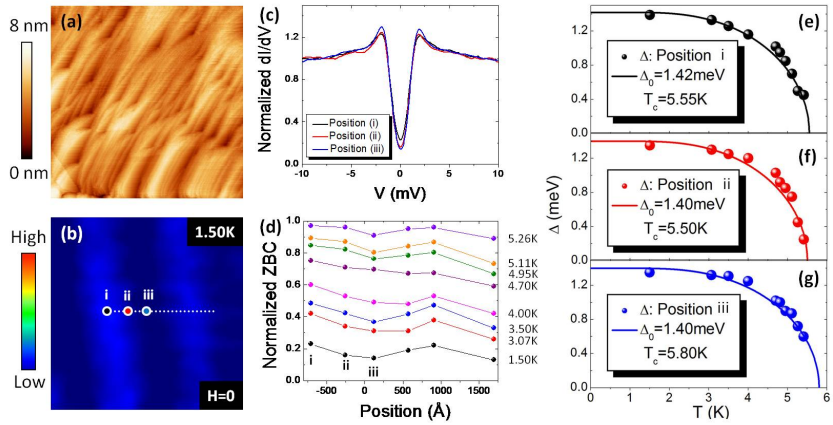

FIGURE 7.3: (a,b) Simultaneously acquired 438x438nm^2 (a) topographic image and (b) zero bias conductance (ZBC) map of the off-axis Pb film. The ZBC map shows the presence of a periodic modulation in conductance far from the transition temperature ($T/T_c \approx 0.25$) and in zero externally applied magnetic field, which reflects local variations of the superconductivity. (c) Characteristic differntial conductance spectra taken in positions: (i) on a bright region (least superconducting), (ii) in between bright and dark regions, and (iii) on a dark region (most superconducting). (d) Temperature dependence of the spatially varying normalized ZBC acquired across the white dashed line of (b) showing that the modulations persist up to temperatures very close to the transition. Positions i, ii, and iii indicated on the ZBC plot are the same as in the map. (e-g) Temperature evolution of the superconducting gap in the three characteristic locations (i, ii, iii) where the gap value was extracted by fitting the dI/dV to the Dynes modified BCS density of states. The solid lines are fits using the BCS formula with the values given in the legends. In all cases the stabilizing tunnel conditions were -10mV and 100pA.

a clear spatial modulation of zero bias conductance values on the lengthscale congruent with that of the underlying ferromagnet domain structure ($w \approx$150-200nm). Representative differential conductance spectra (dI/dV) taken in three characteristic locations with respect to the bright and dark stripes in the ZBC map are shown in figure 7.3(c). To account for slight variations in background the dI/dV curves have been normalized to the conductance values far from the energy gap. The variation $\sim$ 43% of the normalized ZBC values across the stripes is small, with values ranging between approximately 0.2 and 0.14 in the bright and dark regions, respec-

tively. Spectra acquired on a 30nm thick Pb c-axis oriented reference film in magnetic field [8] shows similar values of normalized ZBC in an applied magnetic field of approximately 500 Oe, which is close to the simulated maximum stray field value of the Co-Pd multilayer in figure 7.2(e). A series of temperature dependent dI/dV were subsequently acquired along the white dashed line of figure 7.3(b), and a plot of the resulting normalized ZBC values in figure 7.3(d) shows that this spatial electronic modulation persists with the same periodicity up to the transition to the normal state. The temperature dependence of the superconducting gap $\Delta(T)$ in the three characteristic locations (i, ii, and iii) shown in figures 7.3 (e-g) was determined by fitting the spectra using the equation for tunneling

$$G(V) = G_{nn}\frac{d}{dV}\int_{-\infty}^{+\infty} N_S(E,T,\Gamma)[f(E) - f(E-eV)]dE \tag{7.3}$$

where $f(E)$ is the Fermi-Dirac distribution and G_{nn} is the conductance value at high bias. Here the Dynes modified BCS formula for the superconducting density of states

$$N_S(E,T,\Gamma) = Re\left[\frac{|E| + i\,\Gamma(T)}{\sqrt{(E + i\,\Gamma(T))^2 - \Delta(T)^2}}\right] \tag{7.4}$$

has been used, where T is the temperature, $\Delta(T)$ is the temperature dependent energy gap, and $\Gamma(T)$ is a temperature dependent phenomenonological broadening parameter used to account for the finite lifetime of the quasi-particles[84]. The variation of superconducting transition temperatures found from the fittings is consistent with the expected behavior based on the map, with the highest transition temperature occuring in the most superconducting region (lowest ZBC).

One possible explanation for this behavior invokes arguments based on the theory of domain wall superconductivity [41]. It has previously been shown in similar systems that due to the fact that the magnitude of the out-of-plane magnetic stray field experiences a local minimum above the domain wall the H-T phase diagram

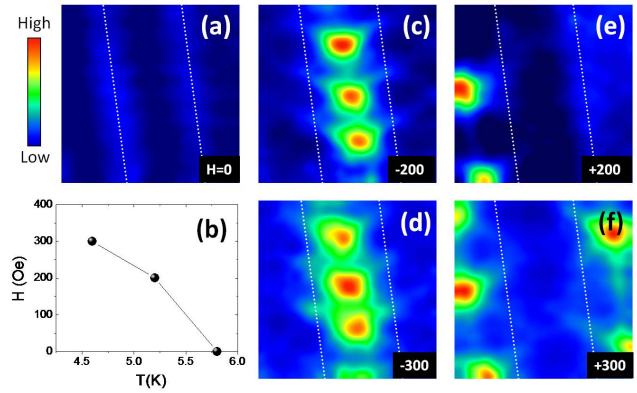

FIGURE 7.4: (a) Same 438×438nm^2 zero-bias conductance map shown in figure 7.3(b) showing the presence of a periodic modulation in ZBC far from T_c and in zero externally applied magnetic field. (b) Highest local found T_c in applied magnetic fields corresponding to the conductance maps shown in (c-f) taken in the same area as (a).

of the entire system can be modified in novel ways depending on the exact domain structure of the underlying magnetic template [14]. Particularly, in the scenario of zero externally applied magnetic fields the transition temperature in the localized region above the domain wall will be higher than that above the domains. However, both the experimental and theoretical investigations of this phenomenon show that this behavior should be confined to temperatures close to the superconducting transition [14, 41]. Our measurements have been performed signficantly far from T_c ($T/T_c \approx 0.25$). If the observed modulations were a consequence of domain wall superconductivity the regions with the strongest superconducting state (dark stripes in figure 2(b)) would be localized above the domain walls.

To obtain an understanding of the locations of the domain walls in the ferromagnet requires some type of magnetic sensitivity. Because STM measurements probe the electronic, rather than magnetic, properties there is no instrinsic sensitivity to the underlying ferromagnet domain structure. Recent measurements, however, have shown that it is instead possible to use the locations of superconducting vortices

as indicators of the underlying magnetic template [10]. In figure 7.4(a) the same conductance map of 7.3(b) is shown, where the white dashed lines have been added to indicate the region with the weakened superconductivity (higher ZBC). Similar conductance maps in small magnetic fields ($\pm$200 and $\pm$300 Oe) in the same area as figure 7.4(a) are shown in figures 7.4(c-f). For S/F systems which meet specific materials dependent and geometry dependent properties it is possible to have vortices *spontaneously* generated in the superconducting film due to the underlying magnetic template even for zero externally applied field [9, 35]. In our system the conditions for spontaneous vortices are not fulfilled, so they are induced only when an external magnetic field is applied. The conductance maps show the vortex cores as regions of higher zero bias conductance due to the systematic increase of states inside the gap when entering the normal vortex core. This increase in states reflects the divergent drop in the pair wavefunction within the vortex core, and as a result the lateral size of the vortex gives an accurate measurement of the coherence length, which for this system falls around $\xi_{\mathrm{GL}}(1.5\mathrm{K})\approx$50nm; in agreement with other ultrathin Pb films[71, 14]. The fact that the vortex size found in the off-axis film agrees with that of the c-axis film is not suprising. In the case of STM measurements of $NbSe_2$ in inclined magnetic fields the shapes and sizes of the vortices mapped at the zero bias conductance remain largely unchanged, which is especially true for small tilt angles [126]. Furthermore, using the relationship $H_{c2}^{\perp}=\phi_0/2\pi\xi_{\mathrm{GL}}^2$ ($\phi_0=2.07\times10^{-7}$ G$\cdot$cm^2) between the coherence length and the upper critical field in the perpendicular direction [17] it is found that $H_{c2}^{\perp}(1.5\mathrm{K})\approx$1320 Oe. Within the framework of Ginzburg-Landau theory [19, 128] the relationship for $H_{c2}^{\perp}$ can also be written as

$$H_{c2}^{\perp}(T) = \frac{4\pi\lambda^2(T)H_c^2(T)}{\phi_0} \tag{7.5}$$

where λ is the penetration depth and H_c is the thermodynamic critical field. Simi-

larly, the upper critical field in the parallel direction can be written as

$$H_{c2}^{\parallel}(T)/H_c(T) = 2\sqrt{6}\lambda(T)/d \tag{7.6}$$

where d is the superconducting film thickness. In the parallel direction this relationship is valid in the limit $d<\sqrt{2}\lambda(T)$. Relating equations (7.5) and (7.6) through the thermodyamic critical field, and using the value of $H_{c2}^{\perp} \approx$1320 Oe found from the coherence length, the parallel upper critical field ca be calculated to be $H_{c2}^{\parallel} \approx$6000 Oe, which agrees well with previous measurements on thin Pb films [129]. Moreover, since $H_{c2}^{\parallel} \gg H_{c2}^{\perp}$ and $H_{stray}^{\parallel} \approx H_{stray}^{\perp}$, it is not possible that the modulation is due to the parallel stray field alone.

The white dashed lines in the conductance maps in figure 4 are always in the same positions, and fall between rows of vortices. In the regime where the domain width is much less than the ferromagnet thickness ($d_F>w$) the vortices nucleate in the regions centered directly above the underlying magnetic domains with the same polarity. This definitively indicates that the regions above domain walls (white dashed lines) have weakened superconductivity in the absence of applied magnetic fields compared with the regions above the domains. This is opposite to that found in the case of domain wall superconductivity. Local temperature dependent dI/dV in positions i,ii, and iii of figure 7.3(b) were acquired for each field in the maps and similarly fit using the Dynes modified BCS formula. The highest T_c found for each magnetic field is plotted in 7.4(b).

In a domain wall superconductivity scenario the H-T phase diagram shows a re-entrant behavior [14, 113]. Our results instead, obtained on off-axis films, exibit a more conventional linear H-T behavior despite the similar presence of the non-uniform superconducting properties. Moreover, the theoretical condition for the nucleation of superconductivity at a domain wall is that the characteristic length scale for nucleation, i.e. the coherence length at the superconducting T_c of the S/F

system, should be smaller than the domain half-width to avoid overlap of the superconducting nuclei [11, 14]. Using $\xi(T_c) \approx \xi_0/\sqrt{1-T_c/T_{c0}}$ where ξ_0 ≈46 nm is the zero temperature coherence length, $T_{c0} \sim 6.8$K is the critical temperature of a Pb film without ferromagnet, and Tc is the critical temperature of the S/F system, gives that $\xi(5.5K)$≈105nm. Taking the magnetic domain width to be approximately 150-200nm from the conductance maps gives that w< $2\xi(T_c)$. Therefore this condition is not fullfilled. The entire body of experimental data obtained indicate that the modulation of the superconducting properties is not due to the domain wall superconductivity and that this modulation follows instead the profile of the in-plane component of the stray field. When the film axis is rotated with respect to the magnetic field there occurs a redistribution of the screening currents, which in the case of an S/F system is non-trivial due to the non-uniformity of the underlying magnetic template. The interplay between the projections of the parallel and perpendicular magnetic stray fields onto the c-axis direction, where the critical field value is the lowest, and this redistribution of screening currents likely leads to the effects seen in this off-axis system.

Furthermore, the ability to visualize these effects most likely stems from energy shifts in the quasi-particle excitation spectrum due to the addition of a Doppler energy term. When this Doppler shift contribution becomes comparable to the superconducting energy gap changes in the quasiparticle density of states at the Fermi energy can occur in the superconductor. By mapping this effect on the density of states in the S/F hybrid with off-axis superconducting film it is possible to directly visualize the unique pattern of supercurrents that exists due the Meissner screening currents and Abrikosov vortex currents.

In summary, low-temperature STM measurements have been performed on a 30nm Pb/[Co-Pd] superconductor/ferromagnet system. A periodic modulation in the superconducting properties is found over length scales similar to the periodicity

of the underlying ferromagnet system. Conductance maps and nanoscale topography as a function of temperature and field identify regions of weaker superconductivity to be found localized above the domain walls. This behavior persists over much of the H-T phase diagram even far from T_c and follows the in-plane component of the stray field. To the best of our knowledge so far there has been no formal treatment of the effects of the parallel component of the magnetic stray field in an S/F hybrid system. Hopefully further theoretical investigations into the open questions on these systems will be motivated by our results.

CHAPTER 8

CONCLUSIONS

In this dissertation low-temperature ultra-high vacuum scanning tunneling microscopy and spectroscopy results on magnetically coupled superconductor/ferromagnet (S/F) hybrid structures have been presented. The goal of these measurements was to successfully visualize the mesoscopic inhomogeneities of the superconducting properties brought about by the presence of a non-uniform magnetic template on length scales that are inaccessible to any other measurement techniques.

It has been shown that the generation of spontaneous vortices/anti-vortices by the underlying ferromagnet layer is non-trivial, and instead depends sensitively on very specific material dependent properties. This information is vital to future improvements in superconductor technologies because at the moment the energy dissipation by vortex motion under applied magnetic fields and currents is one of the major limiting factors preventing the use of superconductors in more applications. Moreover, through this work it has been shown that it is possible to extract information about the underlying magnetic variations in a S/F system by using the superconducting film as an indicator. As computing technologies become smaller and smaller, the ability to manipulate and control the behavior of superconducting vortices at the

nanoscale may be an avenue towards unforseen computational devices.

Among the results presented in this dissertation was the first visualization of the emergence of the localized superconducting nucleus in the case of domain wall superconductivity. The nanoscale variations in the superconducting properties involved in this phenomenon are only accessible using scanning tunneling microscopy. Through the use of external magnetic fields reverse domain superconductivity has also been successfully realized in the systems presented. Similarly to vortices in S/F hybrids, the nanoscale behavior of the domain wall and reverse domain superconducting states show a lot of promise to be utilized in future technologies. The switching behavior of the localized superconductivity under applied magnetic fields, and sensitivity to temperature, make it an ideal candidate towards techological breakthroughs without the need for time consuming lithographic patterning.

While the presented results in this dissertation were completely focused on magnetically coupled S/F hybrid structures the novel physics involved in their proximity coupled counterparts hold even more promise. The experimental capabilities to realize these S/F systems have already been developed during this dissertation and at the time of writing the results are already very intriguing. Hopefully the work performed during this dissertation has some positive impact in the scientific community at large.

Bibliography

[1] B. T. Matthias, H. Suhl, and E. Corenzwit, Phys. Rev. Lett. **1**, 449 (1958).

[2] B. T. Matthias and H. Suhl, Phys. Rev. Lett. **4**, 51 (1960).

[3] V. Jaccarino and M. Peter, Phys. Rev. Lett. **9**, 290 (1962).

[4] L. N. Bulaevskii, A. I. Buzdin, M. L. Kuli, and S. V. Panjukov, Adv. Phys. **34**, 175 (1985).

[5] R. C. Jaklevic and J. Lambe, Phys. Rev. B **12**, 4146 (1975).

[6] W. B. Su, C. S. Chang, and T. T. Tien, Journal of Physics D: Applied Physics **43**, 013001 (2010).

[7] Y. Guo, *et al.*, Science **306**, 1915 (2004).

[8] S. A. Moore, J. Fedor, and M. Iavarone, Supercond. Sci. Technol. **28**, 045003 (2015).

[9] R. Laiho, E. Lähderanta, E. B. Sonin, and K. B. Traito, Phys. Rev. B **67**, 144522 (2003).

[10] M. Iavarone, *et al.*, J. Supercond. Nov. Magn. **28**, 1107 (2015).

[11] A. Y. Aladyshkin, A. V. Silhanek, W. Gillijns, and V. V. Moshchalkov, Supercond. Sci. Technol. **22**, 053001 (2009).

[12] J. Fritzsche, *et al.*, Phys. Rev. Lett. **96**, 247003 (2006).

[13] R. Werner, *et al.*, Phys. Rev. B **84**, 020505(R) (2011).

[14] M. Iavarone, *et al.*, Nat Commun **5** (2014).

[15] K. Onnes, Commun. Phys. Lab. **12**, 120 (1911).

[16] W. Meissner and R. Ochsenfeld, Naturwissenschaften **21**, 787 (1933).

[17] M. Tinkham, *Introduction to Superconductivity*. Dover second edition 2004.

[18] L. Landau, Zh. Eksp. Teor. Fiz. **7**, 19) (1937).

[19] V. Ginzburg and L. Landau, Zh. Eksp. Teor. Fiz. **20**, 1064 (1950).

[20] J. Bardeen, L. N. Cooper, and J. R. Schrieffer, Phys. Rev. **106**, 162 (1957).

[21] L. N. Cooper, Phys. Rev. **104**, 1189 (1956).

[22] L. P. Gor'kov, Sov. Phys. JETP-USSR **36**, 1364 (1959).

[23] L. W. Shubnikow and J. N. Rjabinin, Nature **135**, 581 (1935).

[24] A. A. Abrikosov, Journal of Physics and Chemistry of Solids **2**, 199 (1957).

[25] A. A. Abrikosov, Rev. Mod. Phys. **76**, 975 (2004).

[26] U. Essmann and H. Träuble, Phys. Lett. A **24**, 526 (1967).

[27] W. E. Pickett, Physica B **296**, 112 (2001).

[28] J. G. Bednorz and K. A. Mller, Z. Physik B - Condensed Matter **64**, 189 (1986).

[29] M. R. Norman and C. Ppin, Rep. Prog. Phys. **66**, 1547 (2003).

[30] A. Schilling, M. Cantoni, J. D. Guo, and H. R. Ott, Nature **363**, 56 (1993).

[31] M. Eschrig, Phys. Today **64**, 43 (2011).

[32] E. Matthias, Rep. Prog. Phys. **78**, 104501 (2015).

[33] G. M. Genkin, V. V. Skuzovatkin, and I. D. Tokman, J. Magn. Magn. Mater. **130**, 51 (1994).

[34] S. Erdin, I. F. Lyuksyutov, V. L. Pokrovsky, and V. M. Vinokur, Phys. Rev. Lett. **88**, 017001 (2001).

[35] F. Bobba, *et al.*, Phys. Rev. B **89**, 214502 (2014).

[36] M. Iavarone, *et al.*, Phys. Rev. B **84**, 024506 (2011).

[37] V. Vlasko-Vlasov, *et al.*, Phys. Rev. B **82**, 100502 (2010).

[38] V. Vlasko-Vlasov, *et al.*, Phys. Rev. B **85**, 064505 (2012).

[39] S. Chikazumi and C. D. Graham, *Physics of ferromagnetism* volume 94.; no. 94. Oxford University Press Oxford; New York 2009.

[40] D. Saint-James, G. Sarma, and E. J. Thomas, *Type II superconductivity.* Pergamon Press New York 1969.

[41] A. Y. Aladyshkin, *et al.*, Phys. Rev. B **68**, 184508 (2003).

[42] A. A. Abrikosov, *Fundamentals of the theory of metals.* North-Holland ; Sole distributors for the USA and Canada, Elsevier Science Pub. Co. Amsterdam; New York; New York, NY, USA 1988.

[43] V. V. Shmidt, P. Müller, and A. V. Ustinov, *The physics of superconductors: introduction to fundamentals and applications.* Springer New York; Berlin 1997.

[44] I. Giaever, Phys. Rev. Lett. **5**, 464 (1960).

[45] J. Bardeen, Phys. Rev. Lett. **6**, 57 (1961).

[46] J. R. Oppenheimer, Phys. Rev. **31**, 66 (1928).

[47] J. Tersoff and D. R. Hamann, Phys. Rev. Lett. **50**, 1998 (1983).

[48] J. Tersoff and D. R. Hamann, Phys. Rev. B **31**, 805 (1985).

[49] A. Baratoff, Physica B+C **127**, 143 (1984).

[50] M. S. Chung, T. E. Feuchtwang, and P. H. Cutler, Surf. Sci. **187**, 559 (1987).

[51] C. J. Chen, *Introduction to Scanning Tunneling Microscopy: Second Edition.* Oxford University Press Oxford 2007.

[52] J. M. Rowell, W. L. McMillan, and W. L. Feldmann, Phys. Rev. **178**, 897 (1969).

[53] M. Okano, *et al.*, J. Vac. Sci. Technol. A **5**, 3313 (1987).

[54] A. Hammiche, Y. Wei, I. H. Wilson, and R. P. Webb, Rev. Sci. Instrum. **62**, 3010 (1991).

[55] A. I. Oliva, *et al.*, Rev. Sci. Instrum. **63**, 3326 (1992).

[56] D. W. Pohl, IBM J. Res. Dev. **30**, 417 (1986).

[57] S. H. Pan, E. W. Hudson, and J. C. Davis, Rev. Sci. Instrum. **70**, 1459 (1999).

[58] S. Qin, J. Kim, Q. Niu, and C.-K. Shih, Science **324**, 1314 (2009).

[59] D. Eom, S. Qin, M. Y. Chou, and C. K. Shih, Phys. Rev. Lett. **96**, 027005 (2006).

[60] N. Reyren, *et al.*, Science **317**, 1196 (2007).

[61] A. Gozar, *et al.*, Nature **455**, 782 (2008).

[62] Z. L. Guan, *et al.*, Appl. Phys. Lett. **93** (2008).

[63] T. Cren, L. Serrier-Garcia, F. Debontridder, and D. Roditchev, Phys. Rev. Lett. **107**, 097202 (2011).

[64] T. Nishio, *et al.*, Phys. Rev. Lett. **101**, 167001 (2008).

[65] T. L. Chan, C. Z. Wang, M. Hupalo, M. C. Tringides, and K. M. Ho, Phys. Rev. Lett. **96**, 226102 (2006).

[66] S.-C. Li, *et al.*, Phys. Rev. B **74**, 075410 (2006).

[67] L. Floreano, *et al.*, Progress in Surface Science **72**, 135 (2003).

[68] M. M. zer, Y. Jia, B. Wu, Z. Zhang, and H. H. Weitering, Phys. Rev. B **72**, 113409 (2005).

[69] I. Vilfan and H. Pfnr, Eur. Phys. J. B **36**, 281 (2003).

[70] J. Kim, *et al.*, Proc. Natl. Acad. Sci. **107**, 12761 (2010).

[71] T. Zhang, *et al.*, Nat. Phys. **6**, 104 (2010).

[72] J. M. Dickey and A. Paskin, Phys. Rev. Lett. **21**, 1441 (1968).

[73] S. Bose, *et al.*, J. Phys. Cond. Matt. **21**, 205702 (2009).

[74] M. M. Ozer, J. R. Thompson, and H. H. Weitering, Nat. Phys. **2**, 173 (2006).

[75] M. M. zer, J. R. Thompson, and H. H. Weitering, Phys. Rev. B **74**, 235427 (2006).

[76] Y.-F. Zhang, *et al.*, Phys. Rev. Lett. **95**, 096802 (2005).

[77] J. Noffsinger and M. L. Cohen, Solid State Commun. **151**, 421 (2011).

[78] H. Shaolong, *et al.*, New J. Phys. **12**, 113034 (2010).

[79] M. Jalochowski and E. Bauer, Phys. Rev. B **38**, 5272 (1988).

[80] I. B. Altfeder, K. A. Matveev, and D. M. Chen, Phys. Rev. Lett. **78**, 2815 (1997).

[81] I. Petrov, P. B. Barna, L. Hultman, and J. E. Greene, J. Vac. Sci. Technol. A **21**, S117 (2003).

[82] Y. Jia, *et al.*, Phys. Rev. Lett. **105**, 066101 (2010).

[83] Y. Sun, *et al.*, Nano Res. **3**, 800 (2010).

[84] R. C. Dynes, V. Narayanamurti, and J. P. Garno, Phys. Rev. Lett. **41**, 1509 (1978).

[85] A. J. Bennett, Phys. Rev. **140**, A1902 (1965).

[86] G. I. Rochlin, Phys. Rev. **153**, 513 (1967).

[87] G. I. Lykken, A. L. Geiger, K. S. Dy, and E. N. Mitchell, Phys. Rev. B **4**, 1523 (1971).

[88] J. G. Rodrigo and S. Vieira, Physica C **404**, 306 (2004).

[89] J. C. Swihart, IBM J. Res. Dev. **6**, 14 (1962).

[90] P. Townsend and J. Sutton, Phys. Rev. **128**, 591 (1962).

[91] W. H. Kleiner, L. M. Roth, and S. H. Autler, Phys. Rev. **133**, A1226 (1964).

[92] H. F. Hess, R. B. Robinson, R. C. Dynes, J. M. Valles Jr., and J. V. Waszczak, Phys. Rev. Lett. **62**, 214 (1989).

[93] Y. X. Ning, *et al.*, J. Phys. Cond. Matt. **22**, 065701 (2010).

[94] Y. G. Naidyuk, R. Hussler, and H. v. Lhneysen, Physica B **218**, 122 (1996).

[95] M. Tinkham, IBM J. Res. Dev. **6**, 49 (1962).

[96] Y. Wang, *et al.*, Appl. Phys. Lett. **103**, 242603 (2013).

[97] L. Jiepeng, *et al.*, J. Phys. Cond. Matt. **23**, 265007 (2011).

[98] A. I. Buzdin, Rev. Mod. Phys. **77**, 935 (2005).

[99] Z. Yang, M. Lange, A. Volodin, R. Szymczak, and V. V. Moshchalkov, Nat Mater **3**, 793 (2004).

[100] L. N. Bulaevskii, E. M. Chudnovsky, and M. P. Maley, Appl. Phys. Lett. **76**, 2594 (2000).

[101] M. Iavarone, *et al.*, Magnetics, IEEE Transactions on **48**, 3275 (2012).

[102] G. Karapetrov, *et al.*, Phys. Rev. B **80**, 180506 (2009).

[103] J. R. Barnes, *et al.*, J. Appl. Phys. **76**, 2974 (1994).

[104] A. I. Buzdin and A. S. Melnikov, Phys. Rev. B **67**, 020503(R) (2003).

[105] W. Gillijns, A. Y. Aladyshkin, M. Lange, M. J. Van Bael, and V. V. Moshchalkov, Phys. Rev. Lett. **95**, 227003 (2005).

[106] L. Y. Zhu, T. Y. Chen, and C. L. Chien, Phys. Rev. Lett. **101**, 017004 (2008).

[107] A. Y. Aladyshkin, D. Y. Vodolazov, J. Fritzsche, R. B. G. Kramer, and V. V. Moshchalkov, Appl. Phys. Lett. **97**, 052501 (2010).

[108] J. Fritzsche, R. B. G. Kramer, and V. V. Moshchalkov, Phys. Rev. B **80**, 094514 (2009).

[109] A. Crassous, *et al.*, Phys. Rev. Lett. **107**, 247002 (2011).

[110] O. M. Auslaender, *et al.*, Nat. Phys. **5**, 35 (2009).

[111] E. B. Sonin, Phys. Rev. B **66**, 136501 (2002).

[112] O. Klein, E. J. Nicol, K. Holczer, and G. Grner, Phys. Rev. B **50**, 6307 (1994).

[113] A. Y. Aladyshkin and V. V. Moshchalkov, Phys. Rev. B **74**, 064503 (2006).

[114] A. A. Golubov and U. Hartmann, Phys. Rev. Lett. **72**, 3602 (1994).

[115] M. Tian, *et al.*, Phys. Rev. B **71**, 104521 (2005).

[116] K. Y. Arutyunov, D. S. Golubev, and A. D. Zaikin, Phys. Rep. **464**, 1 (2008).

[117] F. W. J. Hekking and Y. V. Nazarov, Phys. Rev. Lett. **71**, 1625 (1993).

[118] F. S. Bergeret, A. F. Volkov, and K. B. Efetov, Phys. Rev. Lett. **86**, 4096 (2001).

[119] A. I. Buzdin, Rev. Mod. Phys. **77**, 935 (2005).

[120] J. Linder and J. W. A. Robinson, Nat. Phys. **11**, 307 (2015).

[121] D. Mancusi, *et al.*, Supercond. Sci. Technol. **27**, 125002 (2014).

[122] G. Karapetrov, J. Fedor, M. Iavarone, D. Rosenmann, and W. K. Kwok, Phys. Rev. Lett. **95**, 167002 (2005).

[123] M. Tinkham, Phys. Rev. **129**, 2413 (1963).

[124] R. H. White and M. Tinkham, Phys. Rev. **136**, A203 (1964).

[125] H. F. Hess, C. A. Murray, and J. V. Waszczak, Phys. Rev. Lett. **69**, 2138 (1992).

[126] H. F. Hess, C. A. Murray, and J. V. Waszczak, Phys. Rev. B **50**, 16528 (1994).

[127] I. Fridman, C. Kloc, C. Petrovic, and J. Y. T. Wei, Appl. Phys. Lett. **99**, 192505 (2011).

[128] D. H. Douglass, Phys. Rev. Lett. **6**, 346 (1961).

[129] G. D. Cody and R. E. Miller, Phys. Rev. **173**, 481 (1968).